Faculteit Wetenschappen
Departement Fysica

Academiejaar 2013 - 2014

First-principles studie van positronium gebonden toestanden nabij het oppervlak van topologische isolatoren

First-principles study of positronium bound states near the surface of topological insulators

Proefschrift ter verkrijging van de graad van Master in de Fysica

Vincent Callewaert

Promoters: Bart Partoens & Rolando Saniz

Abstract

In this thesis, we study the possibility of positronium, an atom formed by a positron and an electron, bound states near the surface of the topological insulator Bi_2Te_2Se and graphene. The overlap of the bound state's wavefunction with the material can be used to calculate properties which are relevant in positron spectroscopy techniques. The description to determine such bound states is entirely based on quantities that can be obtained from first-principles. We calculate these quantities with the linearized augmented plane wave method approach to density-functional theory. In this first-principles study, we investigate if the edge states that exist near the surface of topological insulators have an important effect on the positronium bound state. For both materials, we present the bound state's energy and wavefunction. At the end of this thesis, we propose an improved model for the positronium bound state near the surface of a material.

Acknowledgements

This thesis forms the endpoint of my career as a student at the University of Antwerp. I am glad to mention that after five years, I absolutely do not regret my choice for physics. Regular confrontation with topics from actual research, showing that up to today there is a lot to be discovered in the field, forms a important factor. In that line, writing this master thesis formed the icing on the cake. I take the opportunity here to express my appreciation for the professors of the department that made studying physics at the University of Antwerp a nice experience. In particular their enthusiasm during the courses and their willingness to help students deserves credit. This master thesis should also be seen a product of their combined efforts over the years to train students from the level of a layman to someone that (hopefully) deserves the title of Master of Physics.
Specifically for this thesis, I would like to express my gratitude towards Prof. Bart Partoens for suggesting this topic, his willingness to help with questions, useful remarks and discussions. For continuous support during the year, discussions of results, comments and suggestions, I would like to thank Dr. Rolando Saniz.
Last but not least, I would like to thank my friends, for some occasional very welcome distractions from this work during the year, and my girlfriend Anne for dealing with my grumbling at times or overenthusiasm at others and in general for keeping me motivated.

Vincent Callewaert May, 2014

Contents

Chapter 1

Introduction

In this general introduction to this thesis, we state the problem we deal with and we motivate why it is relevant. At the end of the chapter, we give an overview of how the rest of the thesis is built up.

1.1 Positron spectroscopy

After the theoretical prediction of the existence of the positron in 1928 by Dirac and the first experimental observation of the particle by Anderson in 1933, positron-electron annihilation processes were extensively studied in the following two decades. During this period, experimental techniques employing positrons were beginning to be developed. In the late 1960's a couple of important papers appeared that showed the sensitivity of positrons to lattice defects in materials. The progress in the 1980's, from the experimental side as well as the development of the theory of positrons in semiconductors and defects, lead to a significant increase in the usage of positron spectroscopy in material research since the early 1990's.
Compared to other experimental techniques for defect identification, positron-spectroscopy excels at characterizing vacancy-type defects. This is easy to understand because the ions will strongly repel the positively charged positron and the latter will thus experience vacancies as attracting centers. The two most frequently used techniques are the positron lifetime spectroscopy and Doppler broadening (of the positron-electron annihilation radiation) spectroscopy. The first technique measures how long the positron survives before annihilating with an electron of the material and relies on the fact that the annihilation rate decreases if the electron density is lower. The information included in these measurements is mainly the size of the vacancies, which can reveal what atoms are missing and if clusters of vacancies are present. The second technique measures the momentum distribution of the annihilating electron-positron pair. If a positron gets trapped in a vacancy defect, it can annihilate with the electrons of the surrounding atoms. Due to the distinct core electron structure of each element, the Doppler broadening technique reveals information about the chemical environment of the vacancy defects. Because of its sensitivity to vacancy-type defects, positron spectroscopy is also often used in the study of polymers and their surfaces [22]. The application of positron-spectroscopy is, however, not

limited to the study of vacancies alone and the application of these techniques is being used to study a variety of systems. As an example, a paper recently appeared that shows that positron spectroscopy is a sensitive technique to probe the surface properties of quantum dots because positrons get trapped at the surface of these nanoparticles [15].
It is not our intension here to go into the details of these experimental techniques but rather motivate the rest of this thesis. Therefore we briefly describe the different scenarios of what can happen with a positron in a sample. After a positron has been fired towards a sample, it quickly loses its momentum and then lives in the order of $\sim 100\,\mathrm{ps}$ in thermal equilibrium with its environment. In the annihilation process, in which momentum and energy are conserved, two energetic photons of around $\sim 511\,\mathrm{keV}$ are sent out in opposite directions. During its lifetime in the material, the positron can just interact with the electron density of the bulk but this process usually does not contain the information experimentalists are interested in. The more interesting case is where a positron encounters a vacancy defect and gets trapped into a localized state, which then reveals information about the defect as described before. The trapping of positrons is not limited to vacancy defects, however, and can also happen at interfaces between materials and at surfaces. There is also a third possible scenario and that is when the positron forms a bound state with an electron, which leads to a significant increase in the lifetime. The annihilation properties of the positron depend on wether it forms a singlet or a triplet state with the electron. Because of the strong repulsion between the bulk electrons and the electron of this positronium (Ps), the interaction between the material and Ps is mainly repulsive. This makes it possible that Ps gets repelled out of the bulk and forms a bound state near the surface of the material or that it gets trapped in a vacancy defect. A recent paper shows that the Ps can be used a sensitive probe for studying the surface properties of pores in porous catalysts [27]. More generally, a Ps bound state near the surface of a material can be used to very selectively probe the surface properties of the material. This because the positron wavefunction has a small overlap with the material that quickly decays to zero. Apart from the annihilation of the positron with its bound electron of the Ps, the overlap with the edge of the material causes the positron to annihilate only with those electrons of the material that are located near the surface. The detected annihilation radiation then contains information about the electronic structure of the surface. One example where measurements that very selectively only probe the surface electronic structure are interesting is in the case of topological insulators, which exhibit conducting states located at the edge of the material while they are insulating in the bulk.
Unlike angle-resolved photoemission spectrscopy (ARPES), which directly reveals (the occupied part of) the electronic structure of a material, the interpretation of positron spectroscopy measurements is not straightforward. As mentioned repeatedly in Tuomisto's paper [52], theoretical modeling can significantly help in the interpretation of experimental data.
The topic of this thesis is to investigate if it is possible to have Ps bound states near the topological insulator Bi_2Te_2Se. From experiments, this seems to be the case [4, 45] but a theoretical investigation can model what to expect from the Ps bound state and can help with the interpretation of experimental data.
A second system we investigate is graphene, also because it is of great interest as of present. Apart from determining wether or not it is possible to have Ps

bound states near these materials, we look for the effect of the edge states on the Ps bound state.

1.2 Topological insulators

A short introduction to topological insulators seems in order here to convince the reader why they are of interest and to understand some of the properties of these materials.

In one sentence, a topological insulator is a material that behaves as an insulator in the bulk while at the surface there exists a conducting state that is robust in the sense that it is unaffected by (non magnetic) defects it might encounter. To understand how such a state can emerge, we begin, in analogy with the review paper of Hasan and Kane [18], by considering the integer quantum hall effect, then explain the spin quantum hall effect after which we can introduce the three dimensional topological insulators.
The quantum hall effect occurs when a strong magnetic field is applied perpendicular to a two dimensional electron gas (2DEG). The cyclic motion of an electron, with a cyclotron frequency of ω_c, is quantized and gives rise to Landau levels. If we define a unit cell with an area that encloses a quantum of magnetic flux, then we can label states with a crystal momentum $\mathbf{k}$ in the plane of the 2DEG. A bandstructure of this system shows no dispersion as function of $\mathbf{k}$ and the different bands are separated by an energy gap $\hbar\omega_c$. This means that an electrical field cannot induce a current since there are no states available directly above the highest occupied electron state. Let us now adopt a classical point of view for a moment, where electrons perform a cyclic motion around flux lines, and imagine that the 2DEG lives inside a rectangle. At the edges, electrons will perform a skipping orbit motion, since they will bump into the edge and cannot move outside the rectangle. At the opposite edge, electrons will move in the opposite direction so that in the absence of an electrical field the net charge displacement is zero. So, in the integer quantum hall effect we have a bulk (the inner part of the rectangle) that is insulating and an edge that shows a conducting state. Moreover, from the classical picture we can understand that an electron propagating in one direction cannot be backscattered, unless it ends up at the opposite edge in the scattering process, so it will just skip around any impurities it encounters at the edge. We seem to have all ingredients we need to fulfill the requirements to classify the integer quantum hall state as a topological insulator, would it not be that the external magnetic field forms an essential ingredient.
Before we discuss how we can get rid of the magnetic field but retain the other properties, let us adopt a band structure description that will prove to be more useful in the rest of the story. Figure 1.1 shows schematically what the bandstructure of the integer quantum hall state looks like. The two bands that cross the Fermi energy are the skipping orbit edge states. If one of the bands denotes a left moving electron at one edge, the other one is the right moving electron that lives at the opposite edge.
Now, it turns out that bandstructures, in the case where there exists a bandgap, can be classified with the total Chern number. A Chern number n_m tells you the net amount of times a Bloch state $|u_m(\mathbf{k})\rangle$ picks up a phase of 2π when it

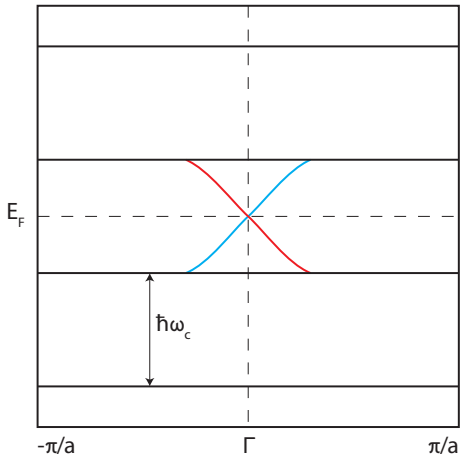

Figure 1.1: Schematic bandstructure plot of the quantum Hall state, where the two colored bands denote the edge states.

makes a walk around the edge of the Brillouin zone. It is easy to understand that it has to be an integer since, when one transports a wavefunction around a closed loop, its value must remain unchanged. This is only possible if the phase changes by an integer amount of 2π. Furthermore, since any smooth changes in the parameters of the Hamiltonian cannot induce a discontinuous change in the wavefunction, the Chern number is in that sense a topological invariant. The total Chern number N is defined as the sum over all Chern numbers n_m of the occupied bands in a system. So also this number cannot change, given that the occupied states do not change, i.e. no bands pass through the bandgap. It has been shown that the Hall conductivity:

$$\sigma_{xy} = N\frac{e^2}{h} \tag{1.1}$$

is determined by this number [51]. Thus, for an ordinary insulator the total Chern number has to be zero. To show how the Chern number can be used to identify conducting edge states, imagine that you have a certain system which has a nonzero Chern number. Because the vacuum can be regarded as an ordinary insulator since it has a bandgap (the pair creation energy), conduction states (electrons) and valence states (the filled negative energy solutions), it has $N = 0$. Now if you consider the Chern number as a function of the position, it will have changed when you start inside the system and end up in the vacuum. We argued above that this cannot happen when no bands pass through the Fermi energy thus, consequently, we must have a conducting state where the number changes, which is at the edge.
The conducting edge state in the quantum hall phase exists only because we explicitly broke the time reversal symmetry of the system by applying a magnetic field to it. We wonder now if it is possible to have conducting edge states without breaking this symmetry. Let us first take a look at what time-reversal

symmetry implies. The time-reversal operator is given by [40]:

$$\hat{T} = e^{i\frac{\pi}{2}\sigma_y}\hat{K}, \tag{1.2}$$

where σ_y is the Pauli matrix and $\hat{K}$ performs the complex conjugation. If we write the exponential as a Taylor series for an arbitrary angle α and if we use that $\sigma_y^2 = 1$, then we can recognize the Taylor series for the sine and cosine. The result is that:

$$e^{i\frac{\alpha}{2}\sigma_y} = \cos\left(\frac{\alpha}{2}\right) + i\sigma_y \sin\left(\frac{\alpha}{2}\right). \tag{1.3}$$

Under the action of the time reversal operator, an electron state flips its spin. This can be seen by applying the operator to a spinor, which then shows that the components of this spinor are swapped after applying the time-reversal operator to it:

$$\hat{T}\begin{pmatrix}\psi_+(x)\\ \psi_-(x)\end{pmatrix} = \begin{pmatrix}0 & 1\\ -1 & 0\end{pmatrix}\begin{pmatrix}\psi_+^*(x)\\ \psi_-^*(x)\end{pmatrix} = \begin{pmatrix}\psi_-^*(x)\\ -\psi_+^*(x)\end{pmatrix}. \tag{1.4}$$

Since we also know that under time reversal symmetry momentum changes direction, we can conclude that under time-reversal an electron state changes momentum and spin at the same time. A second important property of time-reversal for spin-1/2 particles is that $\hat{T}^2 = -1$, so that if we have an eigenstate of a $\hat{T}$ invariant Hamiltonian, it has to be at least twofold degenerate. Indeed, should we have a non-degenerate state $|\phi\rangle$ then we would have:

$$\hat{T}|\phi\rangle = c|\phi\rangle \quad \Rightarrow \quad \hat{T}^2|\phi\rangle = |c|^2|\phi\rangle, \tag{1.5}$$

which is obviously impossible since $|c|^2 \neq -1$. This property is known as Kramers doubling theorem.

The first property of time-reversal tells us how we can make the quantum hall state invariant under time-reversal. Indeed, instead of one conduction channel at each edge, we should have two and these two conduction channels should exist for electrons with opposite spin and momentum. These states are, just like the quantum hall states, robust against (elastic) backscattering. This is trivial in the case where the scattering process does not effect spin. In the case that the scattering does affect spin, it should rotate the electron state by $\pm\pi$ in order to get to the other state. These two possible backscattered states are just as likely, as long as we are dealing with non-magnetic impurities, so that their amplitudes are equal. Because, however, electrons are fermions, these states have opposite sign since they are rotated over 2π relative to each other. As a consequence, we have perfect destructive interference of the backscattered states. The phase that we just described is known as the quantum spin hall insulator, which is the two dimensional topological insulator.

We now use Kramers doubling theorem to formulate a band description of topological insulators. Consider a Bloch Hamiltonian $\hat{H}(\mathbf{k})$, which, if it is time-reversal invariant, has to satisfy:

$$\hat{T}\hat{H}(\mathbf{k})\hat{T}^{-1} = \hat{H}(-\mathbf{k}). \tag{1.6}$$

We know that this is always the case at the points in the Brillouin zone which are connected by a reciprocal lattice vector and at $\mathbf{k} = 0$. This means that

we have a Kramer degenerate pair at these special points in the Brillouin zone for *any* material that has a time-reversal invariant Hamiltonian. Away from these special points, the spin-orbit interaction lifts the degeneracy. The way the Kramer pairs are connected is what determines if we have an ordinary or a topological insulator. In figure 1.2 we plotted the two distinct manners that Kramer pairs can be connected. For a trivial insulator, the degenerate states connect pairwise, which makes it possible to raise the chemical potential above these bands and as such end up with an ordinary insulator. In the case of a topological insulator, this is not possible and there is always an odd number of bands in the positive half of the Brillouin zone that cross the Fermi surface. We also note that close to these Kramer degenerate points, the dispersion of the bands is linear for topological insulators.

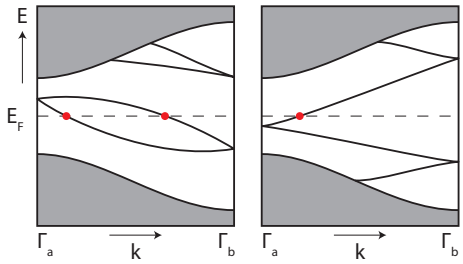

Figure 1.2: A schematic plot of the bandstructure for a trivial insulator (left) and a topological insulator (right). Note that only half of the Brillouin zone is shown since time-reversal invariance require $\hat{H}(\mathbf{k}) = \hat{H}(-\mathbf{k})$. This means there for every crossing of the E_F at $\mathbf{k}$, there is an additional one at $-\mathbf{k}$.

It is now easy to generalize things to a three dimensional topological insulator. We already mentioned that the dispersion between the Kramer degenerate points is linear for the two dimensional topological insulator. For the three dimensional topological insulator, we have Dirac cones near these special points. If we consider the two dimensional Brillouin zone of the surface of a material, we need to determine if there is an odd number of bands crossing E_F between these special points. A similar statement is that we need to determine how many of the Kramer degenerate points are enclosed by the Fermi circle. Either an even number of these points is enclosed by the Fermi circle and in those cases we have weak topological insulators, or an odd number of points are enclosed and then we have strong topological insulators. It is of course also possible that no Dirac cones are present and then we have an ordinary insulator. The weak topological insulators exhibit edge states which are not robust against backscattering. In this case the valence bands with the same spin-polarization of two Dirac cones can connect as well as the conduction bands. The result is then that we end up with an ordinary insulator. In the case of a strong topological insulator, the connection of conduction bands from one Dirac cone to another is also possible but since there is an odd number of cones, there are always at least two metallic states. We summarize this discussion in figure 1.3.
To end this short introduction to topological insulators, we make the connection again with the change of topology across the edge of the material that we employed to determine the existence of the edge state in the quantum hall effect.

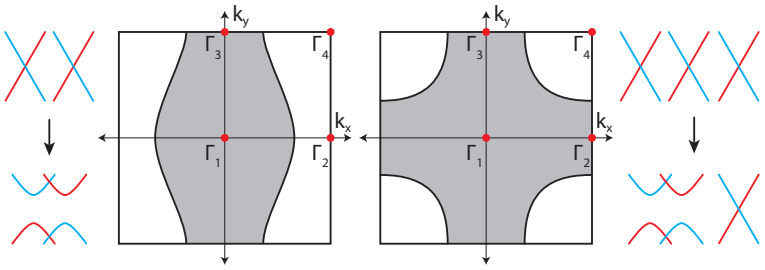

Figure 1.3: Schematic plot of the Fermi circle in the two dimensional Brillouin zone. The grey area denotes the occupied states of the band crossing the Fermi-energy and the white area the unoccupied ones. In the left figure, two Kramer degenerate points are encircled, which corresponds with a weak topological insulator. In the right figure three Kramer degenerate point are encircled, which then corresponds with a strong topological insulator. At the sides, we show schematically the enclosed Dirac cones when no disorder is present (top) or when disorder is present (bottom). The color of the lines denotes the spin-polarization.

The topology of the electronic structure inside the bulk is described by four $\mathbb{Z}_2$ invariants (numbers that are either 0 or 1) and together they determine wether a material is an ordinary insulator, a weak topological insulator or a strong topological insulator. The determination of these numbers is in general quite involved and requires the knowledge of the details of the occupied Bloch states. A necessary condition for a topological insulator is, though, that the bandstructure shows a band inversion. This means that the normal energetic ordering of atomic orbitals inside the bulk of the material is different than in vacuum. Let us examine the example of Bi_2Se_3 [58]. The configurations of the valence electrons for Bi is given by $6p^3$ and for Se by $4p^4$. In figure 1.4, a diagram shows the effect of the chemical bonding between the atoms, the crystal field splitting and the spin-orbit coupling on the energy levels of the p-orbitals. The band inversion occurs in the last step where the spin-orbit coupling is switched on. Since this ordering is topological distinct from the vacuum case, an analogous reasoning than in the case of the quantum hall phase shows that a conducting edge state has to exist.

1.3 Overview of this thesis

We have several goals in this thesis. Firstly, we want to determine if Ps bound states are possible near the surfaces of the topological insulators Bi_2Te_2Se and graphene. Secondly, if bound states are possible, we want to know the effect of the topological edge states on their binding energy. Finally, we want to improve upon the recipe from literature. The rest of this work is organized as follows.

In chapter two we discuss some theory that we need in the rest of the work. Most importantly, this is the recipe that we follow to determine the bound states. The formulas for the Van der Waals attraction that turn up in this description

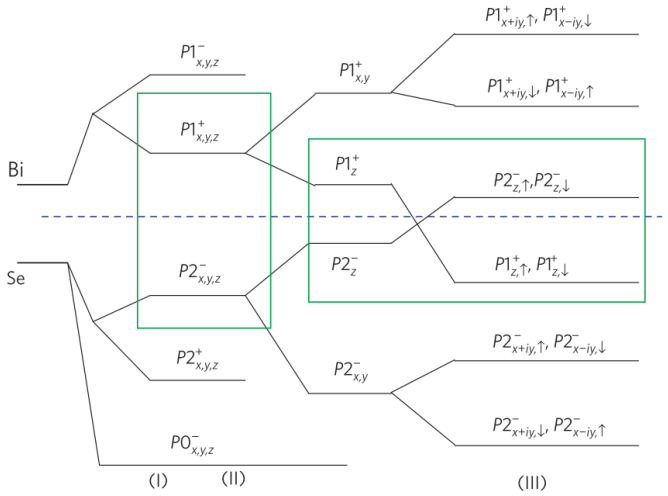

Figure 1.4: A schematic diagram of the evolution of the energy levels of the p-orbitals from the atomic limit (left) to crystalline Bi_2Te_3 at the Γ-point in the Brillouin zone (right). The first stage (I) shows the effect of the chemical bonding, (II) shows the effect of the crystal potential and (III) the effect of the spin-orbit coupling. The dashed blue line represents the Fermi-energy. Figure taken from [58].

are derived in appendix A. Since we need first-principles techniques to determine the quantities in the recipe accurately, we also discuss density functional theory (DFT). We do not use a plane wave package but rather a package that employs the linearized augmented plane wave (LAPW) method. The basics of this method are discussed in chapter two, where we also motivate our choice for the method. More detailed information about the method is given in appendix B.

Chapter three deals with all the DFT calculations of Bi_2Te_2Se. We give all necessary details of the parameters in the calculations. The results are checked against DFT results already available in literature and if possible also against available experimental data. In this chapter we pinpoint quantities that may be influenced by the topological edge states.

The calculation of the Ps bound states are carried out in chapter four. This includes some post processing of the DFT data as well as calculating some quantities that we did not get from chapter three. Once we determined the bound state, we evaluate the dependence of the Ps binding energy of the different parameters in the model. This helps pinpointing those quantities which are most crucial. Armed with that knowledge, we discuss the influence of the topological edge state on the binding energy.

In chapter five we carry out the calculation for graphene. The first-principles study will be less extensive than for Bi_2Te_2Se since we do not have separate bulk

and surface properties because graphene is a two-dimensional material. Also, in Bi_2Te_2Se it is possible to 'turn off' the edge states by including or excluding the spin-orbit coupling but this correction is too small in the case of graphene. At the end of the chapter, we present the calculation for the possible Ps bound states.

In chapter six we propose a more accurate model to determine Ps bound states. We motivate in detail the proposed model as well as our approach to solve it.

Finally, we close off with a conclusion where we summarize the most important findings.

Chapter 2

Theoretical background

In this chapter, we discuss the theory necessary to calculate the Ps bound states. In the first section, we discuss the recipe from literature, which describes the Ps as a neutral particle bound to the surface by the Van der Waals interaction. We derive the formulas that describe the Van der Waals interaction in appendix A, since it is quite long and technical. To evaluate the expressions in the bound state description, we need to determine quantities that are specific for the material in question and we will use density functional theory to obtain them. The second section gives an introduction to density functional theory in general and goes into more detail about the LAPW method. In the third section, we discuss the PAW method in a nutshell.

2.1 Bound state description

In 2007, R. Saniz [43] described the effective potential for the physisorped positronium state as:

$$V(z) = [V_R(z) + V_{VW}(z)]\,\theta(z > z_0) + V_0\,\theta(z \leq z_0), \tag{2.1}$$

where z_0 is the background edge, V_0 is the Ps work function (both discussed further on) and $V_R(z)$ is a repulsion due to the overlap of the wavefunction of the electrons of the solid with the electron of the Ps. The Van der Waals interaction is given by:

$$V_{VW}(z) = -\frac{C}{(z - z_{VW})^3} f(k_c(z - z_{VW})), \tag{2.2}$$

where z_{VW} is the reference plane of the Van der Waals interaction and f is a damping function that we discuss further on. The Van der Waals constant is given by:

$$C = \frac{\hbar}{4\pi} \int_0^\infty d\xi \alpha(i\xi) \left(\frac{\epsilon(i\xi) - 1}{\epsilon(i\xi) + 1} \right), \tag{2.3}$$

where $\alpha(i\xi)$ is the dipole polarizability of the Ps atom evaluated at imaginary frequencies and $\epsilon(i\xi)$ is the dielectric function of the solid which is also evaluated

at imaginary frequencies. This constant described the response of the solid to the instantaneous dipole of the atom. The introduction of the damping function is necessary because the Van der Waals attraction diverges at $z = z_{VW}$ and it was pointed out in the work of Zaremba and Kohn [57] that their description breaks down so close to the surface. The damping function makes sure that the Van der Waals attraction stays finite. In the letter of Saniz, the damping function given in the paper of P. Nordlander and J. Harris [34] was used. This result is, however, approximate and was derived in the case of metals. In the more recent paper of Patil at all. [36], the authors assume that the interaction between the surface and the atom can be modeled by a sum of pairwise interactions between the atom and all the atoms of the surface. For the atom-atom interaction they use an analytic model, which allowed them to write down an exact result for the damping function:

$$f(x) = 1 - e^{-x}\left(1 + x + \frac{x^2}{2} + \frac{2x^3}{15} + \frac{x^4}{60}\right). \tag{2.4}$$

In the argument of the damping function, we wrote a cutoff wave vector k_c and in Saniz' work, the inverse of the positronium hard-core radius was used to determine this value. The physical significance of this is that the response vanishes at short wavelengths. This choice is, however, phenomenological. In the paper of Patil, however, this wave vector is related to the exponential repulsion near the surface:

$$V_R(z) = V_0\, e^{-(z-z_0)/l}. \tag{2.5}$$

Here $1/l$ plays the role of the cutoff wave vector in the damping function, so we chose $k_c = 1/l$ in our description. In the repulsive interaction, l is determined by the electron density decay length at the surface. The next parameter is V_0, for which we take the work function of Ps, i.e. the energy required to remove Ps from the bulk of the material. Finally, z_0 is the background edge position which basically defines the 'edge' of the material. Once we have the potential, we can solve a one dimensional Schrödinger equation:

$$-\frac{\hbar^2}{2m}\nabla^2\psi(z) + V(z)\psi(z) = E\psi(z). \tag{2.6}$$

The negative eigenvalues of this equation, if present, then give us the binding energy of the Ps bound states near the surface.

We now have a recipe for calculating the potential, but let us discuss a bit more in detail how we will proceed to obtain these quantities. The first thing that we need to know is the dielectric function and we can employ density function theory (DFT) to obtain it. This involves carrying out a ground state density calculation for the bulk material and from this result, the dielectric function can be readily calculated. For the materials we consider, the dielectric response is not isotropic. Because the instantaneous dipole of the atom can point in any direction, we shall take an average over these different components to calculate the Van der Waals constant. The work function V_0 can also be determined from bulk properties. The other quantities we obtain from DFT are the background edge position z_0 and the electron density decay length l. For

this we calculate the ground state electron density for a slab and then plot the density, averaged over the (x, y)-plane, as a function of z. In the vacuum above the material, we expect the electron density to start decaying exponentially. The value of z for which this decay starts, determines the background edge position z_0. Also, if we make a linear fit to the logarithm of the density in the region of this exponential decay, the slope of this fit will be the value for l. We will suppose that the Van der Waals reference plane z_{VW} equals the background edge position z_0. This choice actually makes our bound state description independent of the exact value of z_0, as can be see from formulas (2.2) and (2.5). The only quantity left to determine is the atomic polarizability for the Ps, for which we take expressions from literature that are valid for the hydrogen atom. We can do this because the Ps atom is identical to the hydrogen atom apart from its mass. By rescaling the expressions for hydrogen, we can easily obtain results for the Ps atom.

2.2 The LAPW method

Since we perform DFT calculations to obtain the quantities needed to determine the Ps bound states, we shortly introduce this computational approach. In the introduction of this section, we take a look at the Kohn-Sham method for finding the ground state density. The more common approach to solve the Kohn-Sham equations is the pseudopotential method. In our calculations we use another approach, the LAPW method and the bulk of this section deals with explaining it in some detail. The material presented in this section is mainly based on the book of D. J. Singh and L. Nordstrom [47].

2.2.1 Introduction

In DFT calculations, we search for the ground state electron density of a system instead of the wavefunction that can be found by solving the many-particle Schrödinger equation. Since the density is a function of only 3 variables and the many-particle wave function is function of 3N variables, where N is the amount of particles, it is obvious that this an enormous simplification. Since it is the electron density that is the observable and not the wavefunction itself, we expect that all observable quantities can be found from this density. The second Hohenberg-Kohn theorem [19] shows that for the ground state of a system, this is indeed true *if* we know the exact functional for the total energy. The theorem, however, gives no clue about how this exact functional looks like. We can assume, though, we can write it as:

$$E[\rho] = T[\rho] + E_{ee}[\rho] + E_{ext}[\rho], \tag{2.7}$$

where T gives the kinetic energy associated with the density, E_{ee} describes the electron-electron interactions and E_{ext} bundles the electron-ion, ion-ion interaction and possible interactions with external fields. With adequate guesses for these functionals, the problem could be solved within a variational scheme. Too bad, no guess for the kinetic energy functional up to date has been made that produces sufficiently accurate results. Kohn and Sham [25] formulated an approach that circumvents this problem by posing that the kinetic energy of

the density is given by the non-interacting electron gas with the same density. Concretely, in this approach we write the energy functional as:

$$E[\rho] = T_s[\rho] + E_H[\rho] + E_{xc}[\rho] + E_{ext}[\rho] \tag{2.8}$$

where T_s is the kinetic energy of the electrons in the non-interacting system, E_H is the Hartree energy and E_{xc} is the exchange and correlation energy. The latter is the only one that we do not know exactly and approximate forms have to be devised. The Kohn-Sham approach works if this exchange and correlation term is much smaller than the kinetic energy and this is mostly the case. In strongly correlated systems, the approach may, however, break down and then other approaches are necessary.
Let us see how we can construct the system of non-interacting particles such that is has the same density as the real system. The first Hohenberg-Kohn theorem already tells us that there is a unique external potential with which we can realize the same density. We will denote this external potential for the fictitious system by V_f to avoid possible confusion with E_{ext} that we used previously. Also if we mention external potential from now on, we mean the external potential that we pass on to the fictitious system. Suppose that we found the density that minimizes the energy functional. This means that under variations of the density, with the constraint that the amount of particle N does not change, we have:

$$\delta \left\{ E[\rho] - \mu \left(\int d\mathbf{r}\, \rho(\mathbf{r}) - N \right) \right\} = 0. \tag{2.9}$$

In the non-interacting system we know that all terms that turn up in the Hamiltonian are the kinetic energy operators for each particle and the external potential that we are searching. We thus know the energy functional exactly and it is given by:

$$E_f[\rho] = T_s[\rho] + \int d\mathbf{r}\, \rho(\mathbf{r}) V_{\mathrm{f}}(\mathbf{r}) = -\frac{1}{2} \sum_{i=1}^{N} \langle \phi_i | \nabla^2 | \phi_i \rangle + \int d\mathbf{r}\, \rho(\mathbf{r}) V_{\mathrm{f}}(\mathbf{r}). \tag{2.10}$$

We come back to how we can find the one electron states $|\phi_i\rangle$ later. The kinetic energy of the real system in the ground state should of course be given by the lowest kinetic energy we can realize in the fictitious system, given the external potential. We thus also have:

$$\delta \left\{ E_f[\rho] - \mu \left(\int d\mathbf{r}\, \rho(\mathbf{r}) - N \right) \right\} = 0. \tag{2.11}$$

By equating (2.9) and (2.11) we find that the external potential for the fictitious system is given by:

$$V_f(\mathbf{r}) = V_H(\mathbf{r}) + V_{ext}(\mathbf{r}) + V_{xc}(\mathbf{r}) \quad \text{with} \quad V_{xc}(\mathbf{r}) = \frac{\delta E[\rho]}{\delta \rho(\mathbf{r})}. \tag{2.12}$$

Here, $V_H(\mathbf{r})$ is the Hartree potential due to the presence of the other electrons and $V_{ext}(\mathbf{r})$ is the potential caused by the presence of the ions and external fields applied to the real system.

We now consider the system of non-interacting particles to explain how we can find the single particle states $|\phi_i\rangle$. The Hamiltonian is given by:

$$\left(-\frac{1}{2}\sum_{i=1}^{N}\nabla_i^2 + V_f(\mathbf{r})\right)\Psi = E\Psi. \tag{2.13}$$

We know that the exact solution of this Hamiltonian is given by a Slater determinant built from one-electron wavefunctions. By inserting this solution and applying the variational principle, we end up with a set of single particle equations, which form the Kohn-Sham equations:

$$\left(-\frac{1}{2}\nabla^2 + V_f(\mathbf{r})\right)\phi_i(\mathbf{r}) = \varepsilon_i\phi_i(\mathbf{r}). \tag{2.14}$$

This set of equation has to be solved self-consistently since the density of the fictitious system turns up in $V_f(\mathbf{r})$ and the density is determined by putting the N particles of the system in the N lowest energy states $|\phi_i\rangle$:

$$\rho(\mathbf{r}) = \sum_{i=1}^{N}|\phi_i(\mathbf{r})|^2. \tag{2.15}$$

After solving the Kohn-Sham equations self-consistently, we know the kinetic energy of the interacting system and, since we constructed the fictitious system in that way, also the ground state density of the interacting system. The latter is of course only true if we did not get stuck in a local minimum during the self-consistent procedure of solving the Kohn-Sham equations.
When searching for the one-particle states in the Kohn-Sham equations, we must use some finite basis set. Because the equations are derived from the variational principle, the results are then the best approximations we can make with the finite basis and they always have a higher energy than the 'true' one-electron wavefunctions[1]. This explains why a more complete basis set leads to a lower total energy of the system and why convergence w.r.t. the basis always has to be carried out in DFT calculations. We now discuss the basis expansion in more dept.

Because of the Fermi-exclusion principle, every one-electron wavefunction must be orthogonal to all other one-electron wavefunctions. The consequence is that the wavefunctions of valence electrons have a highly oscillatory part near the nucleus, which means that a lot of plane waves have to be used to approximate them and this is usually prohibitive if one wants to perform a practical calculation. One possibility to decrease the required amount of plane waves is to replace the Coulomb potential along with the contribution of the core electrons by a fictitious potential, better known under the name pseudopotential. The first advantage of this approach is that we do not need the wavefunction of the core electrons anymore, because their effect on the result is completely contained in the pseudopotential. A consequence hereof is that when we compute the valence wavefunctions, they are in general not orthogonal to the wavefunctions of the core electrons. Instead we get a smooth version of the wavefunction

[1] We should keep in mind that this applies to the one-electron wave functions in the fictitious system. The total energy in the interacting system is not a rigorous upper bound.

near the nuclei, i.e. the highly oscillatory part needed for the orthogonality with the core states is gone. This forms the second advantage. Far away from the nuclei, the valence wavefunctions should still equal the true valence wavefunctions. Most material properties are determined by the valence electrons in that region. This means that we can expect to find the correct material properties if we get this part of the electron density right. The recipe thus relies on the assumption that core electrons only feel a small influence from the other atoms of the material so that their contribution can be treated as unchanging, which is called the 'frozen core' approximation. So if the pseudopotential reproduces the same electron density at the relevant distances from the atoms, the introduction of a pseudopotential should produce the same answers as an all-electron calculation. From now on we refer to the wavefunctions we find when using a pseudopotential, as pseudo-wavefunctions. The above condition still leaves some freedom for the actual form of the pseudopotential, what leads to different types, like norm conserving and ultrasoft pseudopotentials.
The first one demands that the pseudo-wavefunctions equals the actual valence wavefunctions and potential outside the core radius r_c and also that the norm of both are the same inside the core radius:

$$\int_0^{r_c} dr \int_0^{\pi} d\theta \int_0^{2\pi} d\phi\, r^2 \sin(\theta)\psi^*_{PS}(\mathbf{r})\,\psi_{PS}(\mathbf{r}) = \int_0^{r_c} dr \int_0^{\pi} d\theta \int_0^{2\pi} d\phi\, r^2 \sin(\theta)\psi^*(\mathbf{r})\psi(\mathbf{r}). \tag{2.16}$$

Here ψ_{PS} stands for the valence pseudo-wavefunctions and ψ for the actual valence wavefunctions. A pseudopotential that satisfies these conditions ensures that it is transferable between different systems. By this we mean that a pseudopotential which produces good results for a specific environment of atoms, will also give accurate results for other environments of atoms.
An ultrasoft pseudopotential also has the demand that the pseudopotential reproduces the actual valence wavefunctions and potential outside the core radius r_c but now the pseudo-wavefunctions do not have norm conservation restriction inside the core radius. Instead one wants that as few plane waves as possible should be needed to approximate the valence wavefunctions, hence the name. This approach comes with a couple of complications, one of these being that pseudo-wavefunctions cannot be used directly to compute the charge density since the norm is different from the actual wavefunctions. Another consequence is that ultrasoft pseudopotentials are generally less transferrable to other systems.
The LAPW method takes another approach to deal with the strongly oscillating wavefunctions but there is a close connection between this method and the use of ultrasoft pseudopotentials. Before we explain the LAPW method, we take a look at the original idea Slater published in 1937, namely the APW method.

2.2.2 The APW method

As mentioned in the previous section, the problem with a plane wave basis set is that it is not particularly suited to approximate highly oscillatory functions. In the interstitial regions, that is far away from nuclei, the wavefunctions are however smooth and plane waves are the basis set of choice, certainly also because in reciprocal space the Laplace operator becomes diagonal. Near the nuclei we

can expect that the wavefunctions resemble those of an isolated atom and are thus spherical. A suitable set of basis functions would of course be the spherical harmonics. We can exploit the usefulness of both basis sets, which is the essence of the APW method, by drawing spheres around each nucleus in a way such that none of the spheres overlap. Inside the spheres we use the spherical harmonics to approximate wavefunctions and in the interstitial regions the plane waves basis:

$$\psi(\mathbf{r}) = \begin{cases} \Omega^{-1/2} \sum_{\mathbf{G}} c_{\mathbf{G}} e^{i(\mathbf{G}+\mathbf{k})\cdot\mathbf{r}} & \mathbf{r} \in I \\ \sum_{l,m} A_{lm} u_l(r) Y_l^m(\hat{\mathbf{r}}) & \mathbf{r} \in S, \end{cases} \tag{2.17}$$

where Ω is the volume of the unit cell, $\mathbf{G}$ are the reciprocal lattice vectors of the crystal, Y_l^m are the spherical harmonics and $c_{\mathbf{G}}$ and A_{lm} are the expansion coefficients that need to determined. The $u_l(r)$ are the solutions of the radial Schrödinger equation:

$$\left[-\frac{1}{2r^2} \frac{d}{dr} \left(r^2 \frac{d}{dr} \right) + \frac{l(l+1)}{2r^2} + V(r) \right] u_l(r) = E_l u_l(r), \tag{2.18}$$

where we used atomic units $\hbar = m_e = e = 1$. The potential $V(r)$ in this equation is the spherical component of the potential inside the sphere. The energy parameter E_l requires some further discussion to appreciate its importance in this scheme.

To make sure that the kinetic energy is well defined, the APW method demands that on the boundary of the sphere the wavefunction is continuous by defining the coefficients A_{lm} in terms of the plane wave coefficients $c_{\mathbf{G}}$. To do this we start with the spherical harmonics expansion of a plane wave [29]:

$$e^{i\mathbf{k}\cdot\mathbf{r}} = 4\pi \sum_{l,m} i^l j_l(kr) Y_l^m(\mathbf{r}) Y_l^{m*}(\mathbf{k}), \tag{2.19}$$

where the $j_l(kr)$ are spherical Bessel functions and the spherical harmonics Y_l^m of course only depend on the direction of the argument. If we now demand that the wavefunction is continuous at the sphere boundary r_s, we get:

$$\sum_{l,m} A_{lm} u_l(r_s) Y_l^m(\mathbf{r}_s) = \frac{4\pi}{\sqrt{\Omega}} \sum_{\mathbf{G}} c_{\mathbf{G}} \sum_{l'm'} i^{l'} j_{l'}(|\mathbf{k}+\mathbf{G}|r_s) Y_{l'}^{m'}(\mathbf{r}_s) Y_{l'}^{m'*}(\mathbf{k}+\mathbf{G}). \tag{2.20}$$

If we multiply both sides by $Y_l^{m*}(\mathbf{r}_s)$ and then integrate over the unit sphere, we can use the orthogonality between the spherical harmonics:

$$\int_0^{\pi} d\theta \int_0^{2\pi} d\phi \, Y_l^m(\mathbf{r}_s) Y_{l'}^{m'*}(\mathbf{r}_s) = \delta_{l,l'} \delta_{m,m'} \tag{2.21}$$

to extract a single coefficient A_{lm}:

$$A_{lm} = \frac{4\pi i^l}{\Omega^{1/2} u_l(r_s)} \sum_{\mathbf{G}} c_{\mathbf{G}} j_l(|\mathbf{k}+\mathbf{G}|r_s) Y_l^{m*}(\mathbf{k}+\mathbf{G}). \tag{2.22}$$

The important part here is that these coefficients depend through u_l on the energy parameter E_l and on the plane wave expansion coefficients. The individual functions, consisting of a single plane wave outside the sphere and the set of spherical functions inside the sphere to which this plane waves are matched, are called augmented plane waves (APW) and are labelled by the reciprocal vectors $\mathbf{G}$ and the wave vectors $\mathbf{k}$.
Let us now examine the case where E_l would be fixed. The variational parameters in our problem would then be the coefficients $c_{\mathbf{G}}$ and we would have to solve a secular equation with a non-trivial overlap matrix because the APW are not orthogonal. If we would solve this equation for each $\mathbf{k}$-point, we would find the band energies and the corresponding wavefunctions. But the spherical functions that we used to construct for the APW are only solutions to the radial Schrödinger equation at energies E_l. This means that we would only get the correct result if the band energies exactly matched the values E_l. This shows we must treat the energies E_l as variational parameters.
Still, if we treat E_l as a variational parameter, we would have to start with a guess for E_l, then determine the band energies by solving the secular equation after which the value of E_l can be updated. By repeating this process we could determine all the roots of the secular equation (one for each band in the system) at every $\mathbf{k}$-point as a function of E_l. This is, however, computationally too demanding to be a practical method.
Another problem with the APW method is that in general values for the E_l are needed for which u_l (nearly) disappears at the boundary of the sphere. The plane waves and spherical functions are then decoupled and with the relation between the expansion coefficients (2.22), we see that the secular equation becomes a strongly varying function of E_l, which in turn leads to numerical difficulties.
A last difficulty with the APW method arises when a non-spherical potential would be used in the spheres. That is because bands usually have different orbital characters inside the spheres, in the sense of the linear combination of atomic orbitals with which the state can be constructed. For example, $c_1 d_0 + c_2 d_1$ which have the angular dependence:

$$d_0 = 3\cos^2\theta - 1 \quad d_1 = \sin\theta\cos\theta e^{i\phi}. \tag{2.23}$$

Due to this difference in angular dependence, the orbitals feel a different effective potential which differs from the spherical average that is used the construct the $u_l(r)$. A consequence of this is that the optimal choice of E_l is no longer the band energy and it is hard to determine what value to chose in such cases.

2.2.3 The basics of the LAPW method

In 1975, O. K. Andersen came up with the idea to, instead of only using the u_l inside the spheres, use both the radial functions and their derivative towards the energy parameter E_l, denoted $\dot{u}_l$ [3]. In other words he makes a Taylor expansion around the correct energy parameter ϵ (the band energy) up to first order. It turns out that this linearization of the APW method solves the problems mentioned in the previous section.

More concretely, in the LAPW method we add extra flexibility to the functions inside the spheres by adding the derivatives with respect to E_l of the u_l

to the basis. The wavefunctions are now expanded as:

$$\psi(\mathbf{r}) = \begin{cases} \Omega^{-1/2} \sum_{\mathbf{G}} c_{\mathbf{G}} e^{i(\mathbf{G}+\mathbf{k})\cdot\mathbf{r}} & \mathbf{r} \in I \\ \sum_{l,m} \left[A_{lm} u_l(r) + B_{lm} \dot{u}_l(r)\right] Y_{lm}(\hat{\mathbf{r}}) & \mathbf{r} \in S \end{cases}, \tag{2.24}$$

where the $u_l(r)$ are still solutions to the radial Schrödinger equation:

$$\left[-\frac{1}{2r^2}\frac{d}{dr}\left(r^2\frac{d}{dr}\right) + \frac{l(l+1)}{2r^2} + V(r)\right] u_l(r) = E_l u_l(r) \tag{2.25}$$

and the $\dot{u}_l(r)$ are the derivatives of the $u_l(r)$ with respect to the energy parameters E_l. They are determined by taking the derivative of the radial Schrödinger equation towards E_l:

$$\left[-\frac{1}{2r^2}\frac{d}{dr}\left(r^2\frac{d}{dr}\right) + \frac{l(l+1)}{2r^2} + V(r)\right] \dot{u}_l(r) = u_l(r) + E_l \dot{u}_l(r). \tag{2.26}$$

The coefficients are now determined by demanding that the wavefunction and its radial derivative are continuous at the sphere boundary. The coefficients are thus found by solving the following equations:

$$\begin{aligned} A_{lm} u_l + B_{lm} \dot{u}_l &= \frac{4\pi i^l}{\Omega^{1/2}} \sum_{\mathbf{G}} c_{\mathbf{G}} j_l(|\mathbf{k}+\mathbf{G}|r_s) Y_l^{m*}(\mathbf{k}+\mathbf{G}) \\ A_{lm} \frac{du_l}{dr} + B_{lm} \frac{d\dot{u}_l}{dr} &= \frac{4\pi i^{l+1}}{\Omega^{1/2}} \sum_{\mathbf{G}} (\mathbf{k}+\mathbf{G}) c_{\mathbf{G}} j_l(|\mathbf{k}+\mathbf{G}|r_s) Y_l^{m*}(\mathbf{k}+\mathbf{G}). \end{aligned} \tag{2.27}$$

An important property of the radial functions is that they are orthogonal to any function of the same Hamiltonian that vanishes on the sphere boundary. Indeed, consider the radial Schrödinger equation (2.25) in the following form:

$$\left[-\frac{1}{2}\frac{d^2}{dr^2} + \frac{l(l+1)}{r^2} + V(r) - E_l\right] r u_l(r) = 0, \tag{2.28}$$

from which one can easily show the following relation:

$$(E_2 - E_1) r u_1(r) u_2(r) = \frac{u_2}{2}\frac{d^2 r u_1(r)}{dr^2} - \frac{u_1}{2}\frac{d^2 r u_2(r)}{dr^2}. \tag{2.29}$$

Now if we multiply both side by r and integrate, we find:

$$(E_2 - E_1) \int_0^{r_s} dr\, r^2 u_1(r) u_2(r) = \frac{1}{2} \int_0^{r_s} \left[u_2(r)\frac{d^2 r u_1(r)}{dr^2} - u_1(r)\frac{d^2 r u_2(r)}{dr^2}\right] dr, \tag{2.30}$$

where r_s is the radius of the sphere. The integral in the left hand side of this equation is the overlap between the two function $u_1(r)$ and $u_2(r)$. After partial integration, the right hand side of the equation becomes:

$$\frac{1}{2}\left(r^2 u_1(r)\frac{du_2(r)}{dr}\bigg|_0^{r_s} - u_2(r)\frac{du_1(r)}{dr}\bigg|_0^{r_s}\right) \tag{2.31}$$

Now if either $u_1(r)$ or $u_2(r)$ vanishes on the sphere boundary, i.e. both the value and the derivative go towards zero, this equals zero. This means that the overlap between $u_1(r)$ and $u_2(r)$ must also equal zero or, in other words, $u_1(r)$ and $u_2(r)$ are orthogonal. A similar proof can be given for the $\dot{u}_l(r)$. This shows that core electrons, for which the wavefunction vanishes at the boundary of the sphere (in good approximation), are automatically orthogonal to all valence states. This is an important property that the LAPW method exploits since it allows to make a separation between core and valence electrons. We discuss this more thoroughly in the next section.
The connection with pseudopotential codes can now also be made. Since the valence electrons are automatically orthogonal to the core electrons, the contribution of the core electrons can be seen as an external potential that turns up in the one-electron Hamiltonian for the valence electrons. Now, since the wavefunctions inside the spheres are determined by the coefficients of the plane waves outside and the potential inside the spheres, one could think of a clever way to leave out this contribution entirely (for the potential inside the spheres, for example one could take a 'frozen core' approximation) and to compensate for it in the calculation of the electron densities, potentials, etc. This would then deliver us pseudo-wavefunctions analogous to the ones discussed in the introduction of this section. The contribution of the core can be seen as a very fluffy pseudopotential[2], since the core radius r_s is in general larger than r_c for pseudopotentials and consequently the plane wave cutoff is lower. The approach where one would calculate the core contribution once and then use it as a pseudopotential would, however, not work very well because the pseudopotential we obtain in this way is highly non transferable. Either way, it shows how the two approaches are related.

Let us now go back to the problems we had with the APW method and see how the LAPW method solves them. Consider the case where we calculated the u_l with the energy parameter E_l set to a specific value. If we solve the secular equation for a certain **k**-point, we find a band energy with value ϵ. If the difference between the band energy ϵ and the energy parameter E_l is small, then we can write the correct result, that is the u_l calculated at ϵ, as a Taylor expansion around E_l:

$$u_l(\epsilon, r) = u_l(E_l, r) + (\epsilon - E_l)\dot{u}_l(E_l, r) + O((\epsilon - E_l)^2). \tag{2.32}$$

The u_l and $\dot{u}_l$ in the right hand side are exactly the functions we use inside the spheres to make linear combinations with. If we keep in mind that we construct trial wavefunctions with the results of the u_l and realize that with the variational principle an error of ε in the trial wavefunction yields an error of only ε^2 in the energies, we find that the actual band energies have a final error of order $(\epsilon - E_l)^4$. This shows that if we start with any reasonable guess for the E_l, there is no need to iteratively solve the secular equation. In fact, in practical calculations one can mostly calculate all valence bands in one or two energy windows (different values for E_l), which means that equations (2.25) and (2.26) only need to be solved once or twice (for every value of l in the basis set).
The second problem we had is that it is possible that $u_l(r)$ disappears at the boundary of the spheres around the nuclei. In general the radial derivative of

[2]Softer than ultrasoft!

the $u_l(r)$ as well as the $\dot{u}_l(r)$ do not disappear, which ensures that the plane waves do not decouple from the spherical basis functions inside the spheres.
The last difficulty we mentioned, namely that it is hard to chose the value of the parameter E_l inside the spheres in the case of a non spherical potential, is no longer present. Although we still do not know the optimum value for E_l, errors in the band energies due to this non-optimal choice can be anticipated to be small because of the linearization. The use of a non-spherical symmetric potential inside the spheres is, though, still not as straightforward is it may seem. We give a brief discussion of how this is dealt with in appendix B.

Why do we not try to add the second derivative $\ddot{u}_l(r)$ to the basis set inside the sphere? We could surely expect that the residual error would then be of the order $(\epsilon - E_l)^6$, which could be beneficial when we would have to use more than one value for the E_l in our current scheme to obtain accurate results. The answer to this is that adding extra derivatives increases the required amount of plane waves needed to achieve convergence, while bringing down the required amount of plane waves needed was our initial goal. Indeed, consider an electron state with the exact wavefunction $\psi(\mathbf{r})$. Since plane waves form a complete basis, we can expand this exact wavefunction at the boundary in plane waves:

$$\psi(\mathbf{r}) = \sum_{\mathbf{G}} c_{\mathbf{G}} e^{i(\mathbf{k}+\mathbf{G})\cdot\mathbf{r}} = \sum_{|\mathbf{G}|\leq G_{\max}} c_{\mathbf{G}} e^{i(\mathbf{k}+\mathbf{G})\cdot\mathbf{r}} + \sum_{|\mathbf{G}|>G_{\max}} c_{\mathbf{G}} e^{i(\mathbf{k}+\mathbf{G})\cdot\mathbf{r}}, \quad (2.33)$$

where $G_{\max}$ defines the plane wave cutoff. The derivative of the exact wavefunction is given by:

$$\psi'(\mathbf{r}) = \sum_{|\mathbf{G}|\leq G_{\max}} i(\mathbf{k}+\mathbf{G}) c_{\mathbf{G}} e^{i(\mathbf{k}+\mathbf{G})\cdot\mathbf{r}} + \sum_{|\mathbf{G}|>G_{\max}} i(\mathbf{k}+\mathbf{G}) c_{\mathbf{G}} e^{i(\mathbf{k}+\mathbf{G})\cdot\mathbf{r}}. \quad (2.34)$$

If we now realize that a wavefunction inside the spheres is determined by the plane wave expansion coefficients $c_{\mathbf{G}}$ in the interstitial through the matching conditions, then it is clear that the quality of the wavefunction inside the spheres is determined by the quality of the expansion at the sphere boundary. In the APW method, the matching of the value alone can in principle be done exactly with a finite amount of expansion coefficients. But let us imagine for a moment that we select some cutoff and that the resulting error at the boundary is $\varepsilon_1 = \sum_{|\mathbf{G}|>G_{\max}} \varepsilon_{\mathbf{G}}$. If we now look at the LAPW method, then the error for the value of the wavefunction is still the same but the first derivative has an error $\varepsilon_2 = \sum_{|\mathbf{G}|>G_{\max}} (\mathbf{k}+\mathbf{G}) c_{\mathbf{G}} \varepsilon_{\mathbf{G}}$, which is clearly larger. As a consequence, the resulting error in the wavefunction inside the spheres is larger in comparison with the APW method and a higher plane wave cutoff is needed for the same level of convergence. It should be clear that the error introduced through the matching of subsequent derivates grows quickly and thus the required plane wave cutoff also does. In practice it turns out that methods of higher order than the linearized augmented plane wave cutoffs do not pay off in terms of computation time. A more suitable approach is to select different values of E_l to minimize the resulting errors or, even better, use the local orbital extension that we discuss in appendix B.

2.2.4 Motivation for using the LAPW method

In positron spectroscopy techniques, core electrons play an important role. In the Doppler broadening technique for example, the largest broadening is caused by annihilation of positrons with the core electrons since they have the largest momentum. In plane wave codes, the contribution of the core electrons is modeled as a static potential. This is a good approximation for most purposes because the core electrons are the least influenced by the environment of the atom and because most physical properties of interest are determined by the valence electrons. It is, however, unclear how good this approximation is in the case when the core electrons play an important role in the quantity of interest, e.g. when one wants to calculate the Doppler shift of the radiation of a positron annihilating with core electrons. In the LAPW method, the core electrons are explicitly taken along (see appendix B) and as such, it may offer more accurate results. How large these corrections are, is unclear and for as far as we know, no studies on this topic have been carried out so far.
In this thesis we need properties that are determined by the valence electrons so it is likely still unclear why we chose to use the method anyways. The reason is that the LAPW method is more complex than plane wave codes since a lot more parameters enter in the calculations. Because the properties we want to calculate depend on the electronic structure of the valence electrons, we know that we should obtain similar results in comparison with plane wave codes. If available, we will of course verify our results against experimental data. We hope to build up sufficient experience with the method in this thesis to be able to carry comparative studies like the one mentioned above in the future.

2.3 The PAW method

Because we will employ the PAW method to calculate the work function of Ps, we explain the method in a nutshell. We base our brief discussion on the thesis of O. Leenaerts [26].

The projector augmented wave (PAW) method can be seen as an improvement on pseudopotential methods. In the latter method, the wavefunctions are only correct in the interstitial region where the valence bonds are located. Inside some core radius r_c of each atom, we get smooth pseudo-wavefunctions. In the PAW method, the true wavefunctions $|\psi_i\rangle$ are constructed from these pseudo-wavefunctions $|\psi_{PS,i}\rangle$ by applying a linear transformation operator $\hat{T}_i$ to them inside the spheres:

$$|\psi_i\rangle = \hat{T}_i|\psi_{PS,i}\rangle. \tag{2.35}$$

The linear transformations are obtained by first carrying out an all electron calculation in which the true wavefunctions are obtained. Afterwards, one performs a pseudopotential calculation that delivers smooth wavefunctions, called auxiliary wavefunctions in this case, inside the spheres. Outside the spheres, both results should of course be the same. In the next step, the linear transformations are determined to get from the auxiliary wavefunctions to the true wavefunctions. The transformation to get from the smooth version to the real

wavefunction is defined as:

$$|\psi_i\rangle = \hat{T}_i|\psi_{PS,i}\rangle = (1 + \hat{T}_{0,i})|\psi_{PS,i}\rangle, \tag{2.36}$$

where $\hat{T}_0$ only has an effect inside the spheres. From this equation, it is easy to see that the transformation inside the spheres applied to the pseudo-wavefunction is the same as taking the difference between the real and the pseudo-wavefunction:

$$\hat{T}_{0,i}|\psi_{PS,i}\rangle = |\psi_i\rangle - |\psi_{PS,i}\rangle. \tag{2.37}$$

When studying a certain system, one ends up with a set pseudo-wavefunctions $|\phi_{PS,i}\rangle$ that are different from the auxiliary wavefunctions. The idea is then to expand the obtained pseudo-wavefunctions in the basis determined by the auxiliary wavefunctions. Since the latter are not orthogonal (they are nodeless by construction), projectors are defined that will project the appropriate part of the pseudo-wavefunctions on each of the auxiliary wavefunctions:

$$\langle p_i|\psi_{PS,j}\rangle = \delta_{i,j}. \tag{2.38}$$

The true wavefunction of any system can then, in principle, be written as:

$$|\phi\rangle = |\phi_{PS}\rangle + \sum_i \left(|\psi_i\rangle - |\psi_{PS,i}\rangle\right) \langle p_i|\phi_{PS,i}\rangle. \tag{2.39}$$

The required data, i.e. the true wavefunctions, the auxiliary wavefunctions and the projectors along with the potential defined by the nucleus and the core electrons, are stored in a PAW dataset. It is clear that for each element a separate PAW dataset is required.

Compared to pseudopotential methods, the PAW method is more accurate and the plane wave basis set can be lower. The latter is possible since the core radius can be chosen larger in the PAW method because it gets the wavefunctions correct over the whole unit cell and not only in the interstitial region. In practice, only a finite amount of auxiliary wavefunctions and real wavefunctions can be taken along in the calculations. But because they are only required inside the spheres, they are conveniently expanded in spherical harmonics and a small basis is usually sufficient.

Chapter 3

Frist-principles calculations of Bi_2Te_2Se

3.1 Introduction

The material that we are interested in in this chapter is Bi_2Te_2Se, which is a topological insulator in the family of the second generation materials [18]. Experimentally it has been confirmed to have a topological edge state, while the bulk resistivity of the material is large compared to other members of the family, like Bi_2Se_3 and Bi_2Te_3. The low bulk resistivity in the latter two topological insulators is mostly due to defects [32, 42], while the large bulk resistivity of Bi_2Te_2Se tells us that it is very likely that defects do not play an important role in describing its bulk properties. The low bulk conductivity makes Bi_2Te_2Se a well-suited material for testing properties of 3-dimensional topological insulators.
In the rest of this introductory section, we give the structural parameters of Bi_2Te_2Se as well as the parameters we used in the rest of the DFT calculations. In the rest of the chapter we present and discuss the results of the calculations. We first determine the bulk electronic structure and then the bulk dielectric function of the material. Afterwards we move on to the surface properties, i.e. the electronic structure, the charge density and dielectric tensor of the surface. When we look at these surface properties, we try to determine the effect of the edge states.

Crystal structure: Bi_2Te_2Se has a layered structure, where each layer consists of five atoms in the order Te-Bi-Se-Bi-Te which form covalent bonds while the different layers are held together by Van der Waals forces. We will call such a layer of five atoms a quintuple layer (QL). The space group of the material is $R\bar{3}m$ and the unit cell can be chosen to be either rhombohedral, which consists of 5 atoms, or hexagonal, which consists of 15 atoms. Figure 3.1 shows both unit cells. The experimental cell parameters of the *hexagonal* are given by [31]:

$$\begin{aligned} a_H &= 4.298\,\text{Å} = 8.122\,\text{bohr} \\ c_H &= 29.774\,\text{Å} = 56.265\,\text{bohr}. \end{aligned} \tag{3.1}$$

The paper also provides following fractional positions of the atoms in the *rhombohedral* unit cell:

$$\begin{aligned} &\text{Bi} = \pm(u,u,u) \quad \text{where} \quad u = 0.3958 \\ &\text{Te} = \pm(v,v,v) \quad \text{where} \quad v = 0.2118 \\ &\text{Se} = (0,0,0). \end{aligned} \tag{3.2}$$

Since we will use both unit cells, we mention how the transformation between the two can be carried out. For more detailed information we refer to the International tables of Crystallography Vol. A [17]. Basically, the hexagonal unit cell consists of three rhombohedral units cells with their origins at $(0,0,0), (2/3,1/3,1/3)$ and $(1/3,2/3,2/3)$ inside the hexagonal unit cell, where of course periodicity is used to transport sections of the rhombohedral cells that fall outside the hexagonal cell to the other side of the cell. The atom Se is at Wyckoff position $a : (0,0,0)$ in the rhombohedral cell and thus this translates in the hexagonal cell to the three positions:

$$\text{Se} : (0,0,0), \left(\frac{2}{3},\frac{1}{3},\frac{1}{3}\right), \left(\frac{1}{3},\frac{2}{3},\frac{2}{3}\right). \tag{3.3}$$

The Bi and Te atoms are at Wyckoff position $c : \pm(x,x,x)$ in the rhombohedral cell. The same Wyckoff position in the hexagonal cell is given by $\pm(0,0,z)$ so that the six positions of the Bi and Te atoms are given by:

$$\begin{aligned} \text{Bi} &= (0,0,\pm u), \left(\frac{2}{3},\frac{1}{3},\frac{1}{3}\pm u\right), \left(\frac{1}{3},\frac{2}{3},\frac{2}{3}\pm u\right) \quad \text{where} \quad u = 0.3958 \\ \text{Se} &= (0,0,\pm v), \left(\frac{2}{3},\frac{1}{3},\frac{1}{3}\pm v\right), \left(\frac{1}{3},\frac{2}{3},\frac{2}{3}\pm v\right) \quad \text{where} \quad v = 0.2118 \end{aligned} \tag{3.4}$$

In cartesian coordinates the hexagonal cell is described by:

$$\begin{aligned} \mathbf{a}_1^H &= \frac{a_H}{2}(1,-\sqrt{3},0) \\ \mathbf{a}_2^H &= \frac{a_H}{2}(1,\sqrt{3},0) \\ \mathbf{a}_3^H &= c_H(0,0,1), \end{aligned} \tag{3.5}$$

while the rhombohedral cell axes are given by:

$$\begin{aligned} \mathbf{a}_1^R &= \frac{1}{3}(0,\sqrt{3}a_H,c_H) \\ \mathbf{a}_2^R &= \frac{1}{6}(3a_H,-\sqrt{3}a_H,2c_H) \\ \mathbf{a}_3^R &= \frac{1}{6}(-3a_H,-\sqrt{3}a_H,2c_H). \end{aligned} \tag{3.6}$$

We use the rhombohedral cell to calculate the bulk properties, that is the bandstructure of bulk Bi_2Te_2Se and the dielectric function, for the obvious reason that it contains less atoms and requires less computation time. For the surface properties we use the hexagonal unit cell to construct cells with one or four quintuple layers.

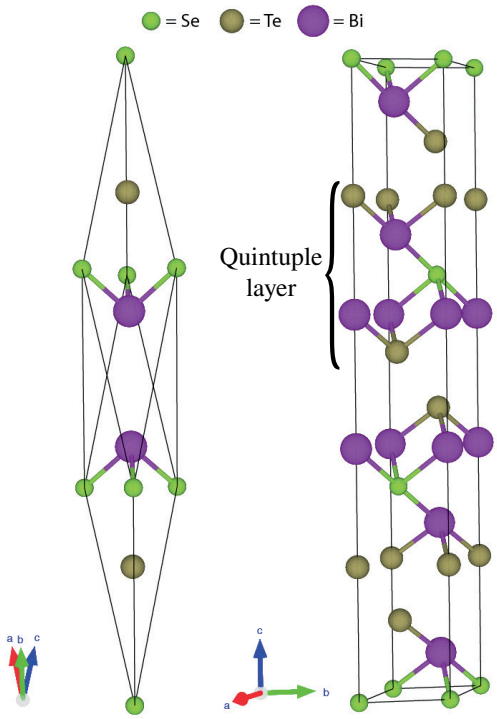

Figure 3.1: The rhombohedral (left) and hexagonal (right) unit cell of Bi_2Te_2Se.

Computational parameters: Unless mentioned otherwise, the first-principles calculations we present are carried out with the DFT code 'Elk', which is an implementation of the LAPW method. Before we started calculating the required properties we carried out the convergence study w.r.t. the k-grid and the basis set. In each step we converged a specific parameter by raising it in steps of 1 (with the exception of rgkmax which was raised in steps of 0.5) until the total energy was converged to within 1 meV, which is certainly strict enough for our purpose. For the individual meaning of each parameter, I refer the reader to appendix B where they are discussed. Below, we give the set of converged parameters that we used in the input file for Elk. The convergence criteria for the self-consistent loop and the smearing function along with the temperature are also mentioned.

kgrid	10 10 10	rgkmax	7.5
gmaxvr	16	lmaxvr	8
lmaxmat	7	lmaxapw	10
nempty	10	lorbcnd	true
epsengy	1×10^{-5}	epspot	1×10^{-7}
stype	Fermi-Dirac	swidth	9.5×10^{-4}

We should mention here that setting the local orbitals on, did not effect the total energy much but since they mainly have an effect on the accuracy of high lying conduction bands (for which the energy parameter $E_l = 0.15\,\text{Ha}$ is not

close enough to the band value), that is actually what we expect. It is, however, not correct to conclude that we can just as well leave them out of the calculation because we need to determine the high lying conduction bands accurately for an accurate prediction of the dielectric function. This is also the reason why we included extra empty bands, while in our convergence study of the total energy, we could be tempted to do with less.
Other parameters in the calculation that we should mention are that the occupation of electron states was smeared out by the Fermi-Dirac distribution with a temperature of $T = 9.5 \times 10^{-4}\,\mathrm{Ha} = 300\,\mathrm{K}$ and that spin-orbit coupling was taken into account by means of a second variational step. All calculations were carried out in the generalized gradient approximation (GGA) of Perdew, Burke and Ernzerhof (PBE) [38].

We attempted to relax the structure but we found erroneous results for the internal relaxation, that is the position of Bi and Te in the unit cell. After the optimization the positions of Bi and Te were no longer given by $\pm(x, x, x)$, i.e. the symmetry got broken. This should be impossible by symmetry considerations alone[1]. Furthermore, with the use of the relaxed internal positions, the bandstructure of the system shows that Bi_2Te_2Se is metallic, which is in contradiction with the experiment (as we will discuss more thoroughly in the following). The relaxation w.r.t. the unit cell parameters was also carried out and here we found values that differed $\sim 1\%$ in comparison with the experimental parameters. It is unsure however, how accurate this is since the internal positions had to be kept fixed. This is why we decided to work with the experimental parameters in all calculations.

3.2 Bulk electronic structure

As a first step in the calculation of the dielectric function, we present the bandstructure as this gives us an important hint as to what we can expect from the dielectric function and since the bandstructure has been presented in other papers with which we can compare our results. Also, we carry out the bandstructure calculation with and without spin-orbit coupling because it is interesting to see how the spin-orbit coupling causes the band inversion, which is necessary to make Bi_2Te_2Se a topological insulator.

We calculated the bandstructure along the lines of the first Brillouin zone, shown in figure 3.2, that connect the time-reversal invariant symmetry points. The coordinates of these high symmetry points in the Brillouin zone of a rhombohedral structure are given, w.r.t. the reciprocal basis vectors, by [44]:

Γ:	(0,0,0)	Z:	$(1/2, 1/2, 1/2)$
F:	$(1/2, 1/2, 0)$	L:	$(1/2, 0, 0)$

The bandstructures with and without spin-orbit coupling taken into account are shown in figure 3.3. For the bandstructure without spin-orbit coupling we find a direct bandgap at the Γ-point of 38 meV. After spin-orbit coupling is taken into account, the bandgap is no longer direct and is situated along the Z-F line

[1] That the symmetry for some systems gets broken is known problem in the Elk code. This was pointed out for us by Dr. J. K. Dewhurst, the main developer of the code.

and has a value of 291 meV, which is remarkably close to the values reported in the experimental studies of Ren [42] and Akrap [2]. We also show the relative contributions of the p-orbitals of each atom to the states of the bands. When we do not take spin-orbit coupling into account we find the normal band ordering Te($5p$) < Bi($6p$). If we include spin-orbit coupling we see that we get the ordering Bi($6p$) < Te($5p$) near the Γ-point. This shows that the spin-orbit coupling causes a band inversion in the bulk and we are indeed dealing with a topological insulator. We explicitly show the Dirac cone in the surface band structure when we study the surface properties.

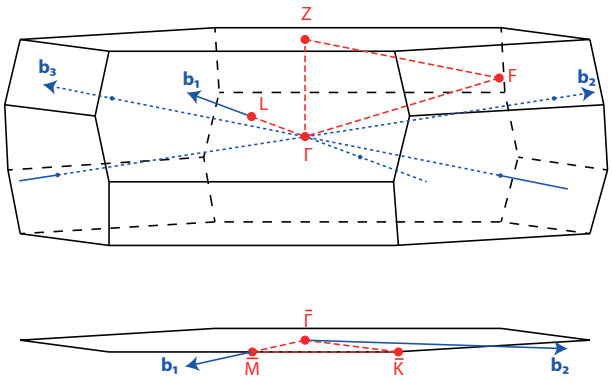

Figure 3.2: The first Brillouin zones for bulk (top) and the slab (bottom). The dashed red lines indicate the path in the reciprocal space used for plotting the band structures.

We compare our results with three papers which have all performed first-principles studies of Bi_2Te_2Se with the PAW method using the DFT package VASP. In the first paper by Dai [12], the bandstructure without spin-orbit coupling does not agree very well with our result in the sense that it shows significant quantitative as well as qualitative differences. The be more precise, the authors of the paper found a direct bandgap with a magnitude of 260 meV at the Γ-point and, for example, the second highest valence band in our bandstructure is shifted downwards by 0.5 eV compared to their result. For the case where spin-orbit coupling is taken into account, the results are in good qualitative agreement with our findings although there are quantitative differences (e.g. near the Γ-point). The bandgap they predict in this case is 0.229 eV. The second paper, by Chang [8], shows much better agreement with our result, with bandgaps of 76 meV without spin-orbit coupling and 272 meV with. From the details they give in their paper, however, no large differences between this paper and the first should be expected. Both papers used the PBE functional and the only differences in the parameters are the plane wave energy cutoff and the k-grid. The third paper, from Wang [54], predicts a bandgap of 0.28 eV for the case with spin-orbit coupling.
It is hard to say what exactly causes the differences for the case without spin-orbit coupling but they could, quite satisfactory, be explained by supposing that the scalar relativistic terms were not included in the calculations of Dai. The

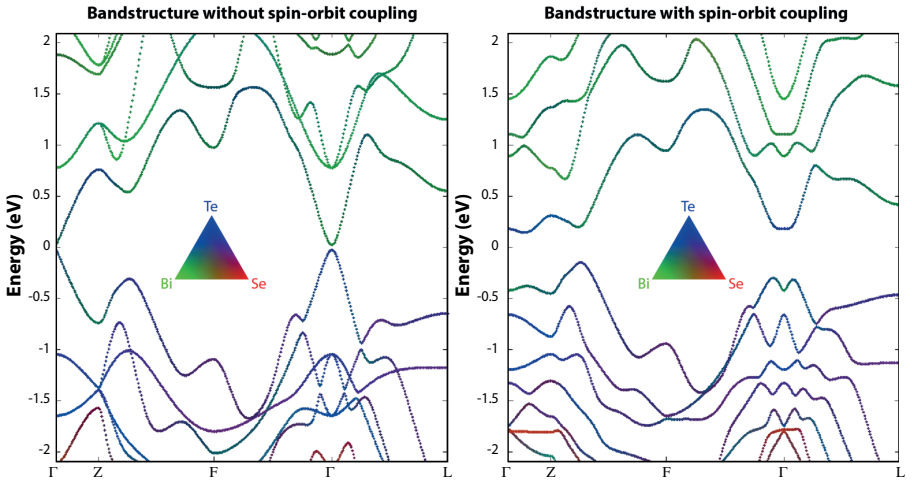

Figure 3.3: Bandstructure of Bi_2Te_2Se with and without taking spin-orbit coupling into account. The different colors show the relative contribution to the states of the p-orbitals from each atom. We only show the p-character here since the other orbital characters of the states is negligible.

scalar relativistic terms are the relativistic mass and the Darwin term and are always included in the Elk code[2]. The first causes electrons to become more concentrated around the nucleus and this leads to a downward shift in the energy. This downward shift in energy gets partially compensated by the Darwin term[3], that gives the extra localized electron additional kinetic energy through the Heisenberg uncertainty principle. The resulting shift of the two contributions is, however, negative [60] and since Bi is a heavier element than Te, the downward shift is larger for the former. Comparing the contribution to the states in the bandstructure from the different atoms, the shifts in comparison with the results of Dai could be explained. We found in some scattered sources, though, that the VASP code normally also includes the scalar relativistic terms. The other option is then to assume that the difference is caused by the use of a different set of PAWs, which could have a significant influence on the results. It stays, however, a guess due to the lack of documentation in the different papers on the details of the PAWs used. Either way, mainly the result with spin-orbit coupling is of interest since it corresponds with the real system and the agreement over the different papers and experiments gives us confidence that it is reliable. The case without spin-orbit coupling we only use in the calculations for the slab to see what effect edge states have on the binding energy of Ps.

[2]Dr. J. K. Dewhurst, the main developer of the Elk code, pointed this out on the forums of the package.

[3]That the Darwin term only affects s-states is only valid for the $1/r$ potential. In a realistic crystal potential, it is most important for the s-states but other states will also experience an influence from this term.

3.3 Bulk dielectric function

Before we discuss our results of the dielectric function, we give the formulas that are used to calculate the function in order to discuss the parameters used in the calculation. The formula for the RPA dielectric function is given by two contributions [33]. The first is the Drude term, which describes intraband transitions and is only present in the case of metals:

$$\epsilon_{\text{Drude}}(\omega) = 1 - \frac{\omega_p^2}{\omega(\omega+\eta)}, \tag{3.7}$$

where $\eta = i/\tau$ is a phenomenological relaxation constant, which can be interpreted as the lifetime of the excitations. Its net effect is a smearing of the peaks in the spectrum. The plasma frequency is given by [37]:

$$\omega_p = \frac{4\pi N e^2}{m^*}, \tag{3.8}$$

where m^* is the effective mass of the electrons in the solid and N the electron density. Since we found a finite bandgap, we know that we do not have to include this contribution for calculating the dielectric function. We just keep in mind that we need to take this term into account when we are dealing with metals as it is a parameter that has to be set explicitly in Elk. The second contribution to the dielectric function is given by the interband transitions. In Elk, the optical conductivity is calculated rather than this part of the dielectric tensor but the latter is easily obtained from the former through the transformations:

$$\Re[\epsilon_{\alpha\beta}(\omega)] = \delta_{\alpha\beta} - 4\pi\Im\left[\frac{\sigma_{\alpha\beta}(\omega)}{\omega+\eta}\right] \tag{3.9}$$

and

$$\Im[\epsilon_{\alpha\beta}(\omega)] = 4\pi\Re\left[\frac{\sigma_{\alpha\beta}(\omega)}{\omega+\eta}\right], \tag{3.10}$$

where $\alpha,\beta = \{x,y,z\}$, $\sigma_{\alpha\beta}$ is a specific element of the optical conductivity tensor, ω is the frequency and $\eta = i/\tau$ is again the inverse of a phenomenological lifetime times the imaginary number. The optical tensor itself is calculated by evaluating following formula[4] [41]:

$$\begin{aligned}\sigma_{\alpha\beta}(\omega) = i\int_{\text{BZ}} d^3\mathbf{k}\sum_{l,n}\frac{1}{\omega_{ln}(\mathbf{k})}\left[\frac{\Pi^\alpha_{ln}(\mathbf{k})\Pi^\beta_{nl}(\mathbf{k})}{\omega-\tilde{\omega}_{nl}(\mathbf{k})+\eta}+\frac{(\Pi^\alpha_{ln}(\mathbf{k})\Pi^\beta_{nl}(\mathbf{k}))^*}{\omega+\tilde{\omega}_{nl}(\mathbf{k})+\eta}\right] \\ \times f(E_n(\mathbf{k}))f(E_l(\mathbf{k})).\end{aligned} \tag{3.11}$$

Here $\tilde{\omega}_{nl}(\mathbf{k})$ is the energy difference between the states n and l, $f(E_n(\mathbf{k}))$ gives the occupation of the state n and $\Pi_{ln}(\mathbf{k})$ are the matrix elements:

$$\Pi_{ln}(\mathbf{k}) = \langle\Psi_l(\mathbf{k})|\left(\mathbf{p}+\frac{\boldsymbol{\sigma}\times\nabla V(\mathbf{r})}{4}\right)|\Psi_n(\mathbf{k})\rangle, \tag{3.12}$$

[4]Other schemes are frequently implemented in other codes, see [41] for a more detailed discussion.

where $\mathbf{p} = -i\hbar\nabla$ is the crystal momentum and the second term describes spin-orbit coupling. The point we want to make is that (3.11) tells us to integrate over the whole Brillouin zone while in practice, we only have a finite k-mesh. At each of these grid points we get a delta function-like contribution to the optical conductivity, which is smeared out depending on the value of η.
We now carry out a calculation in which we try to converge the spectrum of the dielectric response, which is more strict than obtaining a converged value for the Van der Waals constant. This is because the dielectric response at imaginary frequencies depends on an integral over the real frequencies, as we show later, and the Van der Waals constant in turn is determined by an integral over the imaginary frequencies. The converged spectrum, however, allows us to compare with experiment. In our calculations we used the Fermi-Dirac distribution to determine the occupancy of the states, that is:

$$f(E_n(\mathbf{k})) = \frac{1}{1 + \exp\left(\frac{E_n(\mathbf{k}) - E_F}{k_B T}\right)}, \tag{3.13}$$

in which the temperature T is a parameter we can choose in Elk. We put its value to room temperature, which corresponds to $T = 9.5 \times 10^{-4}$ Ha for calculating the ground state density. In the Elk code the same T determines the value of η but we found that with this smearing we could not converge the dielectric function without having to select a k-grid which is prohibitive in terms of both computation time and memory usage[5]. The reason for this is twofold, the first is that the k-point mesh we used was not dense enough for the smeared delta peaks to overlap sufficiently and the second is that when we increased the k-grid, the k-points were not located at the same points in reciprocal space. Combined, this gave rise to wiggles in the dielectric function that were different for each k-grid. This is why we decided to increase the smearing in the dielectric function[6], although it also smooths out the features the dielectric function has. By increasing the smearing with small steps, we found that the dielectric function was sufficiently converged with a $32 \times 32 \times 32$ k-grid with a smearing of $\eta = 0.0025$ Ha. The final results for the dielectric function are shown in figure 3.4.
We now compare our result with the experimental study of Akrap [2] who measured the optical conductivity of Bi_2Te_2Se in the planes of the quintuple layers, i.e. $\sigma_{xx} = \sigma_{yy}$. Therefor we plot the optical conductivity calculated by equation (3.11) in the units employed in the article. The result is shown in figure 3.5. The experimental result shows five clear peaks in the optical conductivity. One is a phonon mode at low energies which is missing in our spectrum because we did not take phonons along in our calculation. The other four we can find in our plot, the first and second one (starting from the left) are at $4600\,\mathrm{cm}^{-1}$ and $7500\,\mathrm{cm}^{-1}$ respectively. Compared to the experimental findings[7] of $\sim 3000\,\mathrm{cm}^{-1}$ and $\sim 6000\,\mathrm{cm}^{-1}$ at 295 K both peaks are shifted towards

[5] We started with a $8 \times 8 \times 8$ k-grid up to a grid of $36 \times 36 \times 36$ in steps of $+4 \times 4 \times 4$.

[6] As mentioned already, Elk uses the same parameter for both the smearing width η as the temperature for the Fermi-Dirac distribution. Because we are not interested in the ground state at high temperatures, we carried out the ground state calculation with $T = 9.5 \times 10^{-4}$, which also determined the occupancies of the different states. Afterwards we changed the parameter to the desired value of η before calculating the dielectric function.

[7] The values I cite here are only approximate since it is difficult to determine these values accurately from a logarithmic plot.

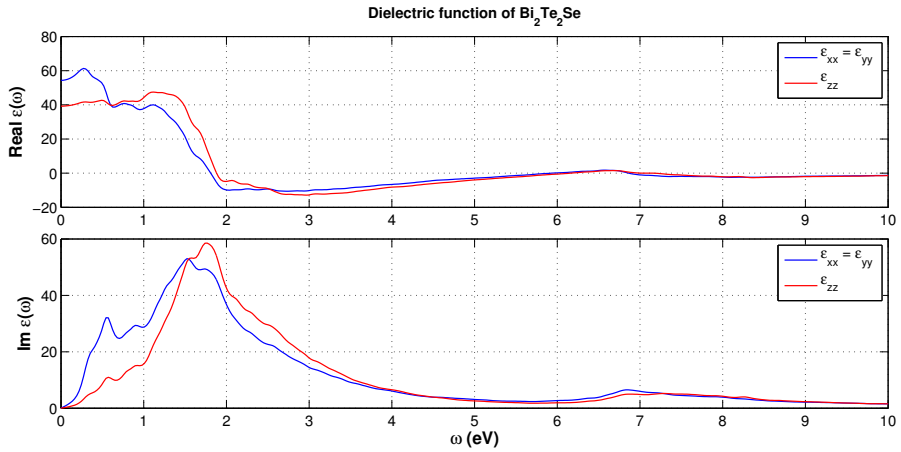

Figure 3.4: Plot of the dielectric function in the (x, y)-plane (blue) and along the z-direction (red). We calculated the dielectric function up to 1 Ha $\approx 27\,\text{eV}$ but since it is very featureless for high frequencies, we only show the more interesting part here.

higher frequencies by about $1500\,\text{cm}^{-1}$, which corresponds to 186 meV. Both of these peaks are somewhat closer to our result if we would compare with the measurements at lower temperatures in the inset of figure 3.5. The third and fourth peak appear in the experimental spectrum as one peak at $\sim 13000\,\text{cm}^{-1}$ which is in quite good agreement with our result of $13500\,\text{cm}^{-1}$ that we obtain by taking the mean of the positions of the two peaks. The last peak of the experimental spectrum can be identified with the two small bumps or shoulders in our result. Taking the mean again, we find a 'peak' at $19535\,\text{cm}^{-1}$ which agrees well with the experimental result of $\sim 20000\,\text{cm}^{-1}$. We can conclude the peak positions are in reasonable agreement with the experiment. Actually, we can anticipate that small differences will not have a large influence on the possible existence and binding energy of the positronium, since we will always take an integral of the dielectric function. This will become clear when we discuss the analytic continuation. We discuss the sensitivity of the Van der Waals constant on the dielectric function further on in this work.

3.4 The Ps work function

The work function of the Ps is the net energy required to remove a Ps from the bulk of the material towards the vacuum. This energy can be calculated by taking the difference between the Ps binding energy and the electron and positron work functions combined [5]:

$$\phi_{PS} = \phi_- + \phi_+ - \frac{1}{4}, \tag{3.14}$$

where we used atomic units. For clarity, we give a schematic overview of the different energy contributions mentioned in the following discussion in figure 3.6. The electron work function is determined by (1) the energy required to move an

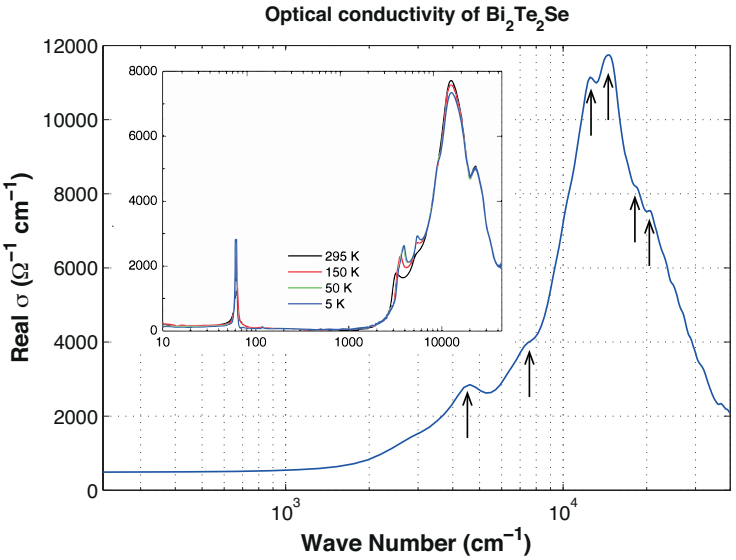

Figure 3.5: Plot of the optical conductivity in the planes of the quintuple layers. The arrows indicate the characteristic peaks in the spectrum. The inset shows the experimental result taken from [2].

electron from the highest occupied state in the crystal to the 'crystal zero', i.e. minus the chemical potential, and (2) the energy required to physically drag the electron from the bulk to the vacuum. The positron work function is determined by (1) the energy required to move the positron from the lowest possible state in the crystal to the crystal zero and then (2) the energy required to physically move the particle from the crystal to the vacuum. If we determine the crystal zero from electrostatic energy alone, the second contribution is the same in magnitude but opposite in sign for the two particles. We stress, though, that this does not work if the zero in the calculations is determined from quantities that are not electrostatic in nature, e.g. if the zero is determined by the average Kohn-Sham energy in the unit cell. This is because the exchange and correlation energy is different for the electron than it is for the positron, i.e. the crystal zero and (2) would be different for both particles. Under the assumption that the crystal zero is determined from electrostatic energy alone, the Ps work function is determined by:

$$\phi_{Ps} = (-\mu^- + \Delta) + (-\mu^+ - \Delta) - \frac{1}{4} = -\mu^- - \mu^+ - \frac{1}{4}, \tag{3.15}$$

where μ^-, μ^+ are the electron and positron chemical potentials respectively and Δ is the energy required to physically drag the electron from the bulk to the vacuum. In our calculation, the Kohn-Sham eigenvalue of the highest occupied electron state determines the value of the electron chemical potential. For the positron, we take the Kohn-Sham eigenvalue of the lowest possible state in the material.

In principle we have to solve the two-component DFT problem self-consistently to determine the Kohn-Sham eigenvalues values. This means that we first calcu-

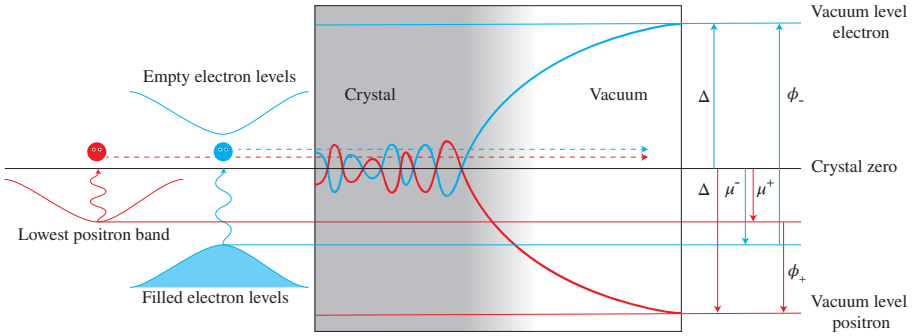

Figure 3.6: Schematic overview of the energy levels and differences discussed above. The blue lines and arrows denote electron related quantities and the red lines the positron related quantities. In the box, we have drawn the electrostatic potential for both particles, which has the opposite sign. At the left side we have drawn the energy bands for the electron and the positron. Note that the crystal zero in principle can lie anywhere, i.e. it does not have to lie in between occupied and unoccupied energy levels.

late the ground state electron density in absence of the positron. In the second step one adds the positron to the system and calculates its ground state while keeping the electron density fixed. Then, the ground state electron density is calculated again but this time in the presence of the positron density. Afterwards the positron density is calculate again, etc. The process is iterated until convergence for both the electron and positron density is reached. This approach is usually very demanding in terms of computation time. In our case, however, it suffices to calculate the positron density once in the ground state electron density, obtained in absence of the positron. Indeed, in the case where we are dealing with a perfect crystal and if we assume only one positron is present in the material at any given time, which is very reasonable, the particle is delocalized over a large region. The resulting positron density at any given point is then very low and it can be expected that the effect on the electron density is very small. In the case of vacancy defects, the approach is not justifiable but this is a problem we do not deal with here.
To calculate the positron states in the material, we need to use a different functional than for electrons. This is because there is no exchange with the electrons of the material since the positron and electrons are distinguishable particles. Also the correlation between electrons mutually is different than between a positron and electrons.

Unfortunately, there are no algorithms implemented in the Elk package to carry out positron related calculations. Instead, we use the plane wave package Abinit, in which the crystal zero is determined by setting the average Hartree and local potential equal to zero[8]. We used a PAW method with the PAW

[8]This is explicitly mentioned on the Abinit website where the output of the code is explained. We quote literally: 'In the present implementation, the average Hartree potential and local potential are imposed to be zero, but not the average exchange-correlation potential.' The local potential is the potential due to the presence of the ions.

data files we could find on the Abinit website. We carried out the convergence study w.r.t. to the plane wave cutoff and the cutoff for expanding the density. We found that 35 Ha and 118 Ha respectively gave results for which the total energy was converged to within 1 meV. The amount of auxiliary wavefunctions that were used were left at the standard value defined in the PAW datasets. The functional that we used is again the PBE for the electron ground state calculation while for the positron state we used the GGA functional of Barbiellini reported in [10]. In our calculation, we included the spin-orbit coupling because we saw from the bandstructure that it has a significant effect on the location of the Kohn-Sham levels. For each Se and Te atom in the unit cell, we have six valence electrons and for Bi we have five, which means that 28 states are occupied at each k-point.
From the bandstructure, we know that the valence band maximum is located along the $Z - F$ line in the Brillouin zone. The value we found for the valence band maximum is given by $\mu^- = -0.22977$ Ha. The lowest available positron state is always located at the Γ-point and we found that its value is given by $\mu^+ = -0.02990$ Ha. The result for the Ps work function is thus given by $\phi_{Ps} = 9.67\,\text{mHa} = 0.263\,\text{eV}$.

3.5 Electronic structure near the surface

We now move from bulk properties towards surface properties of Bi_2Te_2Se. Previous DFT studies show that 4 QLs are necessary before the conducting edge states show up [8,12]. Since we are interested in the effects of the edge states, we calculate all surface properties with a unit cell that contains 1 QL as well as with a unit cell that contains 4 QLs. Since Elk uses periodic boundary conditions in three directions, we included 14 bohr of vacuum to avoid interactions between the images of the slabs. The spin-orbit interaction is taken into account in the case of 1 QL and in the case of 4 QLs we carry out the calculations both with and without. We selected a k-grid of $24 \times 24 \times 1$ while all parameters in the calculation of the surface properties were kept the same as in the case of the bulk properties.

We first present the electronic structure of the Bi_2Te_2Se surface. The path in the Brillouin zone is shown in figure 3.2 and the coordinates of the time-reversal invariant points in the reciprocal basis are given by:

Γ: (0,0)	M: $(1/2, 0)$	K: $(2/3, 1/3)$

We calculated the electronic structure for a slab consisting of 1 QL and 4 QLs with the spin-orbit coupling taken into account and for the case of 4 QLs also without. The results are shown in figure 3.7. In agreement with Dai's paper [12], we find that a finite bandgap is present in the case of 1 QL and that it disappears in the case of 4 QLs. The reason for this bandgap is that for 1 QL, there is a significant overlap of the wavefunctions of the edge states at the opposite edges of the slab. The interaction between these states at the opposite edges opens a bandgap [8]. If the slab consists of more QLs, the overlap becomes smaller and the case of 4 QLs the gap at the Dirac cone becomes insignificant. The only difference with the results of Dai we notice is that the Fermi-energy is shifted ~ 0.06 eV in the case with spin-orbit coupling. As a consequence the last valence

band along the $\Gamma - M$ in our result stays well below the Fermi-energy while in his result, it passes very slightly above.
The electronic structure at the surface also shows that Bi_2Te_2Se is indeed a

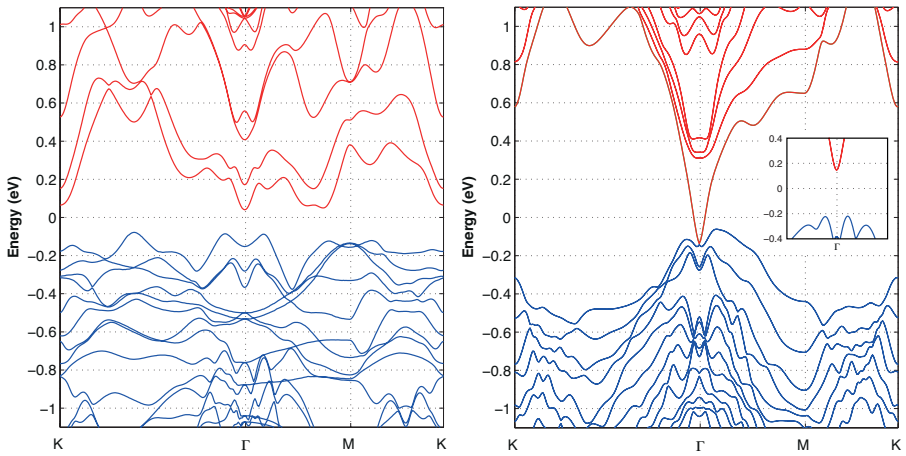

Figure 3.7: The electronic structure of a slab consisting of 4 QLs when the spin-orbit interaction is excluded (left) or included (right). The inset in the right figure shows that a bandgap opens when the calculation with spin-orbit coupling is carried out for a slab consisting of 1 QL.

strong topological insulator. As explained in the introduction, the Fermi circle should enclose an odd number of Kramer degenerate points, which is clearly the case here.

3.6 The surface electron density

We are now interested in obtaining the background edge position z_0, which tells us at what point the electron density starts decaying exponentially, and the electron decay length l. To obtain these quantities, we averaged the calculated ground state electron density over an equidistant 25×25 grid in the unit cell in the plane of the surface and then plotted the logarithm of this averaged density along the z-axis. We found that 14 bohr was not enough to 'separate' the surface electron densities of both sides of the slab. By this we mean that the electron density started increasing again before it reached the minimal representable value with the chosen basis set, i.e. the electron density in the vacuum was nowhere approximately constant in the plot. This is why redid the calculation with 33 bohr (one and a half times the size of a QL) of vacuum in the cell. The result is shown in the left plot of figure 3.8 for both the 1 QL as the 4 QLs case with spin-orbit coupling. We see that the densities are nearly identical with the exception of the region far away from the surface, where the electron density stops decaying exponentially and reaches the minimal representable value of the basis set. Outside this region, the maximal relative difference between the two densities is 0.27%. This result already shows us that in our description of the Ps bound state, we can only expect a negligible difference in the repulsive part

of the potential between the 1 QL and 4 QLs layer case.
Let us discuss in some more detail the differences in the charge densities when we consider 1 or 4 QLs and include or exclude the spin-orbit interaction. In figure 3.9, we show the absolute and relative differences in the electron densities between the different cases. To make these plots, we calculated the charge density of the 1 QL case over the whole unit cell and then shifted the origin to the middle of the QL. In the case of the 4 QLs, we calculated the charge density from the first atom of the last QL up to the first atom at the other side of the slab. This density was then shifted to correspond with the positions of atoms in the 1 QL case. The difference shown in the inset of the right plot is of course calculated over the whole unit cel of the 4 QLs slab. The first thing we like to point out is that the relative difference in the vacuum part becomes large and that it should be compared with the absolute difference which in fact becomes very small in that region. Comparing the cases with and without spin-orbit coupling, we see that in the case of 4 QLs the differences in the density towards the middle of the slab are slightly smaller than closer towards the surface. We also checked this by plotting the difference in charge density over the whole slab. We expect that this difference is due to the presence of the edge states but we have to conclude that the effect of these states is small compared to other differences in the charge density caused by the spin-orbit interaction. To further motivate that the effect of the edge state on the density is small, we consider the difference between 1 QL and the last QL of the 4 QLs slab. We already stated that in the case with the spin-orbit interaction, the edge states are present in both cases. This means that at the vacuum edge for the 4 QLs (to the right side of the plot), we expect that the difference is small, which is indeed what we see on the plot. The difference grows further to the middle of the slab so that we might think this is due to the second edge state that is present for the 1 QL. We notice, however, that the difference is nearly identical when we leave out the spin-orbit coupling. The effect of the edge state can then only be the resulting difference between the green and black curves on the plot. We thus do not expect to see large differences in the electron density decay length and furthermore, we cannot claim that these differences are prominently caused by the edge states.

To determine the value of the electron decay length we used linear regression in a region where the electron density is clearly decaying exponentially. The electron decay length is given by the inverse of the slope of the resulting fit. We avoided the regions too close to the surface, where the electron density shows different behavior, and the region far away from the surface, where the electron density decays slower. The latter is caused by the fact that we used a finite plane wave basis set to expand the electron density. The interval that we deemed appropriate for the fit is given by $[3.25, 5.00]$ bohr, where we took the position of the topmost atom in the last QL as origin. The fitting region is indicated in the plot by arrows. The resulting electron decay length for the 4 QLs layer case with spin-orbit coupling included is given by $l = 0.6781 \pm 0.0001$ bohr $= 0.3588 \pm 0.0001$ Å. The background edge position z_0 is determined by the point, measured from the position of the topmost atom of the slab, where the electron density starts decaying exponentially. We determined this by calculating the relative difference between the electron density and the linear fit. Then we searched, from the region where we fitted towards the surface, for the first point

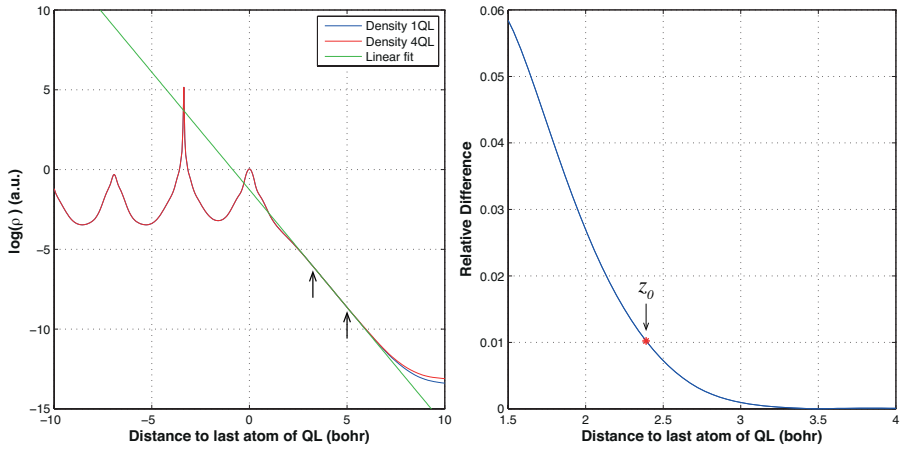

Figure 3.8: The left plot shows the electron averaged electron density at the surface for 1 QL and 4 QL, where the spin-orbit interaction is taken into account, as well as the linear fit to the logarithm of the density. The arrows indicate the left and right boundary of the fitting region. The right figure shows the relative difference between the electron density and the linear fit. The point where this differences becomes larger than 1% determines the background edge position.

that has a relative difference larger than 1%. The value we found in this way is given by $z_0 = 2.39\,\text{bohr}$.
In the case of 4 QLs where we did not take spin-orbit coupling into account, we found, using the same fitting region, $l = 0.6761 \pm 0.0002\,\text{bohr} = 0.3578 \pm 0.0001$ Å and $z_0 = 2.39\,\text{bohr}$. In the case of 1 QL where spin-orbit coupling was included we found $l = 0.6771 \pm 0.0001\,\text{bohr} = 0.3583 \pm 0.0001$ Å and $z_0 = 2.39\,\text{bohr}$. The differences between these three results are very small and of the order of the changes we get by changing the fitting region, which confirms what we expect from our discussion of the differences in the charge density between the different cases.

3.7 Dielectric function near the surface

We just discussed that the edge states have a negligible effect on the electron decay length l and thus we do not expect that the edge states alters the repulsive part of our potential in a significant way. The attractive part, however, depends on the dielectric tensor and we can expect that the metallic edge state has a larger impact on this quantity. This because for metals we have a larger response at longer wavelengths in comparison with insulators. The form of the Van der Waals interaction we discussed in appendix A is valid for long wavelengths and thus for an atom far away from the surface. We saw that the response of the solid in our description is the response to an infinite oscillating charge density at a distance z far away from the surface. To link the surface's response function with the dielectric tensor of the bulk, we argued that the induced charged density at the surface has to be fed by a current coming from deep within the solid.

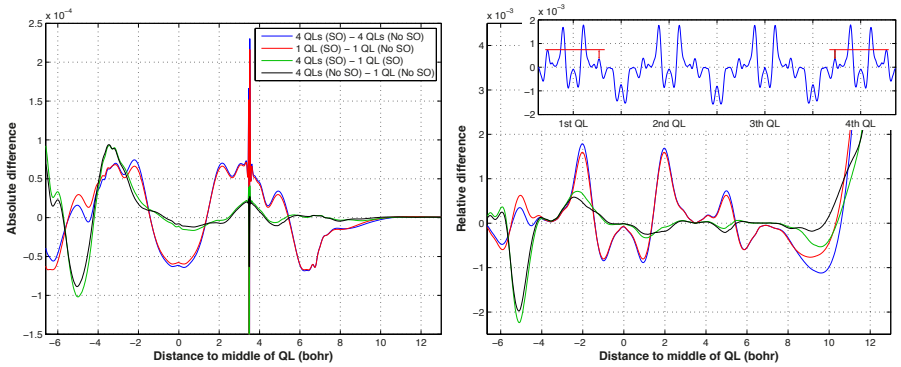

Figure 3.9: Comparison of the absolute and relative differences of the averaged charge densities between the 4 different situations. The inset in the right figure shows the relative difference in charge density in the 4 QLs case with and without spin-orbit coupling over the whole slab. The peak in the left plot can be ignored since it corresponds with the position of a core, where the electron density is very high. The right plot in fact shows that the relative difference there is in fact negligible.

Intuitively, we can argue, however, that the solid actually feels an oscillating spherical charge density from the instantaneous dipole of the atom. The induced charge then does not necessarily come from the bulk of the material and can come from surface as well. This is why we calculate the dielectric response of a slab with both 1 QL and 4 QLs with the spin-orbit coupling taken into account. We know that the difference in the dielectric response then comes from wether or not the edge state shows metallic behavior. We do not consider the case without spin-orbit coupling because the difference in electronic structure is too large to claim that it only comes from the edge state. We mention that we had to lower the parameters in our calculation since we ran into memory problems. The parameters we changed are given by:

rgkmax	7.0	lmaxapw	9
gmaxvr	15	lmaxvr	3

We carried out a convergence study w.r.t. the change in the dielectric function for 1 QL and found that increasing them does not significantly change the output. Also for reasons of computation time, we chose a k-grid of $24 \times 24 \times 1$ for which we selected a smearing of $\eta = 0.01$.
We need to be careful, however, since the dielectric response we calculated is in fact a bulk response function and it does not immediately translate to a surface response function by adding vacuum. Indeed, the surface dielectric response in fact depends on the distance to the surface, as pointed out in the paper of Cheng [9]. This because the translational invariance perpendicular to the surface is broken and one then carries out a Fourier transform only in directions parallel to the surface. In the long wavelength limit, Cheng relates the surface and bulk dielectric function by means of a sum rule. For the bulk dielectric

function, the f-sum rule is given by:

$$\int_0^\infty d\omega\, \omega\, \Im\left[\frac{1}{\epsilon_b(q,\omega)}\right] = -\frac{\pi}{2}\omega_p^2, \tag{3.16}$$

where $\epsilon_b(q,\omega)$ is the bulk dielectric function and ω_p is the bulk plasma frequency (3.8). For the surface we have a similar rule:

$$\int_0^\infty d\omega\, \omega\, \Im\left[\frac{1}{\epsilon_s(Q,\omega)}\right] = -\frac{\pi}{2}\omega_s^2(1+\alpha Q+\dots), \tag{3.17}$$

where $\epsilon_s(Q,\omega)$ is the surface dielectric function, Q is a reciprocal wave vector parallel to the surface, α is a quantity that depends on the details of the considered surface and ω_s is the surface plasma frequency. The latter is related to the bulk plasma frequency by $\omega_s = \omega_p/\sqrt{2}$ in the $Q = 0$ limit. If we thus evaluate the l.h.s. of (3.16) with the bulk dielectric function we calculated previously, we obtain the bulk plasma frequency. From (3.17), we see that if we carry out the same integral for the dielectric function we calculated for the slab, we should obtain half this value. If we do the rescaling like this, we model the case where the experiment is carried out for a semi-infinite material.
Because experiments can be carried out for thin films of Bi_2Te_2Se, we also consider the dielectric response of a slab of material. In this case, we also need to rescale the dielectric function and we explain this in more detail in section 5.1.4, where we calculate the dielectric function of graphene. In this rescaling, we need to multiply by the length of of c-axis and afterwards divide by the thickness of the slab. For the latter we take the distance between the first and the last atom of the slab plus twice the background edge position z_0.
The result for a thin film of Bi_2Te_2Se is shown in figure 3.10 and the result rescaled with the sum rule in figure 3.11. The first thing we notice is the extra peak in the spectrum at low frequencies for the imaginary part of the dielectric tensor present in the case of 4 QLs. The extra low frequency contribution is caused by the Drude contribution (3.7) to the dielectric response and has to be included for the 4 QLs, because in that case we are dealing with a metal. For 1 QL, we left this contribution out because we found earlier that we then have a finite bandgap. Because the plasma frequency for the ϵ_{zz}-component we found is an order of magnitude lower than for the other components, the Drude contribution shows no significant contribution to component. The rest of the peaks in the imaginary part of the dielectric tensor in the case of 4 QLs are also shifted towards lower frequencies compared to the case of 1 QL.

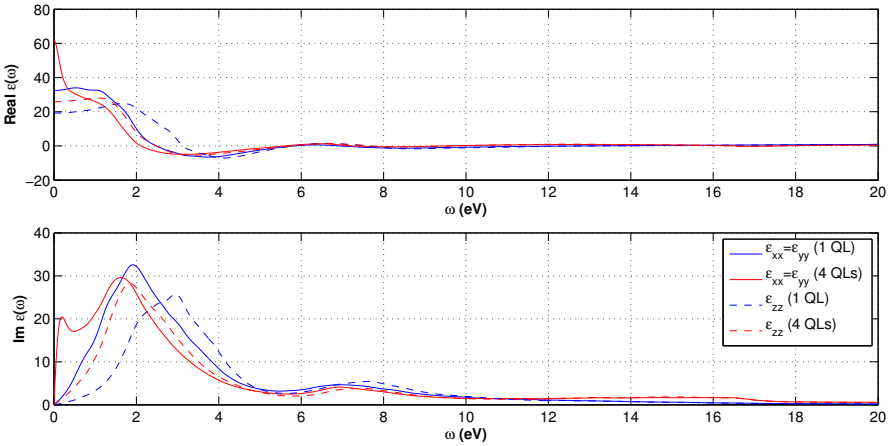

Figure 3.10: The dielectric response of a slab of Bi_2Te_2Se with 1 or 4 QLs with the spin-orbit coupling taken into account. This figure shows the output of the Elk code after rescaling to account for the vacuum in the unit cell, i.e. to correspond with the response of a thin film.

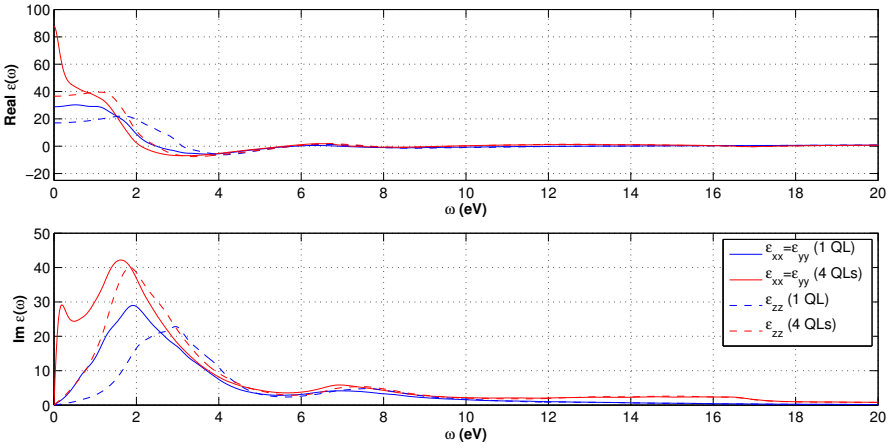

Figure 3.11: The dielectric response of a slab of Bi_2Te_2Se with 1 or 4 QLs with the spin-orbit coupling taken into account. We obtained this result by rescaling the output of the DFT calculation with the sum rules.

Chapter 4

Positronium bound states near Bi_2Te_2Se

So far, we determined the reference plane position z_0, the electron density decay length l and the work function V_0 from the DFT data. We also calculated the dielectric function of the bulk material but in our description of the potential, we need to evaluate this function at imaginary frequencies. In the following we explain the analytic continuation that allows us to find these values. Afterwards, we discuss the atomic polarizability, which is the last ingredient we need. The rest of this chapter is devoted to study the bound state. The first step is to determine the bound state and its binding energy. Afterwards we evaluate the sensitivity of the binding energy w.r.t. all the parameters in the description. At the end of the chapter we discuss the influence of the edge states on the binding energy of Ps.

4.1 Dielectric function for imaginary frequencies

From the DFT calculations, we obtained the real and imaginary part of the dielectric function but only for real valued frequencies. We can get the value of the dielectric function for imaginary frequencies by analytic continuation. To do this, we start from the Cauchy theorem:

$$\oint_C \frac{\chi(\omega)}{\omega - v} d\omega = 0. \tag{4.1}$$

The contour we consider is shown in figure 4.1, so the Cauchy theorem is valid if $\chi(\omega)$ is analytic in the upper half plane since the pole is not included in the contour. Now if we also have that $\chi(\omega)/|\omega| \to 0$ if $\omega \to \infty$, then the contribution to the contour integral due to the big half circle in the upper plane vanishes and we can write:

$$\int_{-\infty}^{\infty} \frac{\chi(\omega')}{\omega' - v} d\omega' - 2\pi i \lim_{\omega \to v} \chi(\omega) = 0 \tag{4.2}$$

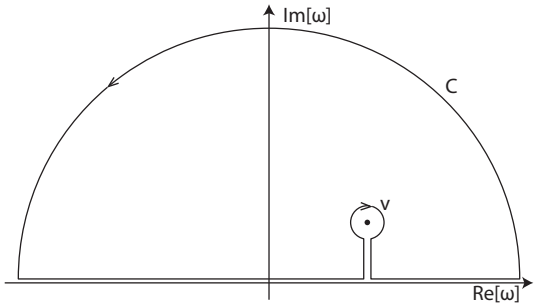

Figure 4.1: The contour C used in the Cauchy Theorem.

or:

$$\chi(v) = \frac{1}{2\pi i} \int_{-\infty}^{\infty} \frac{\chi(\omega')}{\omega' - v} d\omega'. \tag{4.3}$$

The dielectric function minus one satisfies the above conditions, which can be understood by, for example, looking at relations (3.9) and (3.10). Indeed, the term $\sigma_{\alpha\beta}/(\omega + \eta)$ vanishes at high frequencies. Another argument is that the dielectric tensor gives us the relation between the external electrical field and the displacement field $\mathbf{D}(\omega) = \epsilon(\omega)\mathbf{E}(\omega)$. At high frequencies the response of the material vanishes and we need to have $\mathbf{E}(\omega) = \mathbf{D}(\omega)$. This allows us to write:

$$\epsilon(i\xi) - 1 = \frac{1}{2\pi i} \int_{-\infty}^{\infty} \frac{\epsilon(\omega) - 1}{\omega - i\xi}. \tag{4.4}$$

If we multiply the nominator and denominator by $(\omega + i\xi)$ we get:

$$\epsilon(i\xi) = 1 - \frac{1}{2\pi i} \int_{-\infty}^{\infty} \frac{\epsilon_1(\omega) - 1 + i\epsilon_2(\omega)}{\omega^2 + \xi^2} (\omega + i\xi) d\omega, \tag{4.5}$$

where $\epsilon_1(\omega)$ is the real part of the dielectric function and $\epsilon_2(\omega)$ is the imaginary part. Because $\epsilon_1(\omega)$ is an even function of ω, the integral over $\omega\epsilon_1(\omega)$ will give zero. Similarly, since $\epsilon_2(\omega)$ is an odd function of ω, the term $\xi\epsilon_2(\omega)$ will drop [55]. So we find:

$$\epsilon(i\xi) = 1 + \frac{1}{\pi} \int_{0}^{\infty} \frac{\xi(\epsilon_1(\omega) - 1) + \omega\epsilon_2(\omega)}{\omega^2 + \xi^2} d\omega \tag{4.6}$$

We know $\epsilon_1(\omega)$ and $\epsilon_2(\omega)$ from the DFT calculations, up to a certain cutoff value for ω. Now because $\lim_{\omega\to\infty} \epsilon_1(\omega) = 1$, $\lim_{\omega\to\infty} \epsilon_2(\omega) = 0$ and the ω^2 in the denominator, we can get accurate results by numerically integrating the equation up to the cutoff frequency. To do the numerical integration, we used the

composite Simpson rule:

$$\int_a^b f(x)dx = h\left[\frac{1}{3}(f(x_1)+f(x_n)) + \frac{4}{3}\sum_{n=1}^{n/2-1} f(x_{2n}) + \frac{2}{3}\sum_{n=1}^{n/2-1} f(x_{2n+1})\right], \tag{4.7}$$

where $f(x_1) = f(a)$, $f(x_n) = f(b)$ and $x_i - x_{i-1} = h$.

4.2 Polarizability of positronium

Rescaling of units The polarizability of Ps can be obtained easily from the polarizability of a hydrogen atom. Indeed, by going to the center of mass coordinates of the system, the mathematics is nearly identical. The only difference is that the positron mass enters the equations instead of the proton mass. This means that all expressions stay the same but we have to rescale our units. The centre of mass and relative coordinates become:

$$\mathbf{R} = \frac{m\mathbf{r}_1 + m\mathbf{r}_2}{2m} = \frac{1}{2}(\mathbf{r}_1 + \mathbf{r}_2) \tag{4.8}$$

$$\mathbf{r} = \mathbf{r}_1 - \mathbf{r}_2 \tag{4.9}$$

The inverse mass is given by:

$$\mu = \frac{1}{m} + \frac{1}{m} = \frac{2}{m} \tag{4.10}$$

The energy levels of the Ps atom are then given by:

$$E_n = -\frac{E_I}{n^2}, \tag{4.11}$$

where n is the principal quantum number. The ionization energy is given by:

$$E_I = \frac{\mu e^4}{2\hbar^2} = \frac{1}{2}\frac{me^4}{2\hbar^2} = \frac{E_I^H}{2}, \tag{4.12}$$

where E_I^H is the ionization energy of the hydrogen atom. So whenever we encounter parameters with the dimension of energy that were derived for the hydrogen atom, we have to divide by a factor of two. The classical orbit radii of the Bohr model are given by:

$$r_n = n^2 a_0, \tag{4.13}$$

in which the bohr radius for the Ps atom is given by:

$$a_0 = \frac{\hbar^2}{\mu e^2} = 2\frac{\hbar^2}{me^2} = 2a_0^H. \tag{4.14}$$

This means we have to multiply by two for every parameter that has the dimension of length if it was derived for the hydrogen atom.

Eigenfrequency and oscillator strength formulation. We use the numerical results for the dipole polarizability of hydrogen tabulated in the paper of A. Dalgarno and G. A. Victor [13]. Since they made a few mistakes with prefactors and units throughout their paper, we give the correct expressions here. The polarizability α is defined as:

$$\mathbf{p} = \alpha \mathbf{E}, \tag{4.15}$$

where $\mathbf{p}$ is the induced electric dipole moment, which has SI units $[\,\mathrm{C}\cdot\mathrm{m}]$. The electric field has SI units $[\,\mathrm{N}\cdot\mathrm{C}^{-1}]$ so that the polarizability should have SI units $[\,\mathrm{C}^2\cdot\mathrm{m}^2\cdot\mathrm{J}^{-1}]$. In their paper, Dalgarno and Victor express the polarizability as:

$$\alpha(\omega) = \frac{2}{3}\int_n \frac{\tilde{\omega}_n |\langle\psi_0|\hat{\mathbf{d}}|\psi_n\rangle|^2}{\tilde{\omega}_n^2 - \omega^2}, \tag{4.16}$$

where the integration is assumed over both the discrete states and the continuum. The electric dipole operator is given by $\hat{\mathbf{d}} = \sum_i e_i \hat{\mathbf{r}}_i$, the $|\psi_n\rangle$ and $|\psi_0\rangle$ are respectively the eigenfunctions and the ground state of the atom and the eigenfrequencies are defined by the energy difference between the ground state and excited states[1]:

$$\tilde{\omega}_n = E_n - E_0. \tag{4.17}$$

Next, they introduce the dipole oscillator strength but make a mistake with the prefactor. The correct expression is given by:

$$f_n = \frac{2m_e}{3\hbar^2 e^2}\tilde{\omega}_n |\langle\psi_0|\hat{\mathbf{d}}|\psi_n\rangle|^2, \tag{4.18}$$

which is a dimensionless quantity as it should be. If we also approximate the sum over discrete states plus the integral over the continuum by a sum over the first N lowest discrete states, we find:

$$\alpha(\omega) = \frac{\hbar^2 e^2}{m_e}\sum_{n=1}^{N}\frac{f_n}{\tilde{\omega}_n^2 - \omega^2}, \tag{4.19}$$

or for imaginary frequencies:

$$\alpha(i\omega) = \frac{\hbar^2 e^2}{m_e}\sum_{n=1}^{N}\frac{f_n}{\tilde{\omega}_n^2 + \omega^2}. \tag{4.20}$$

Let us now rescale the quantities given in the paper. The eigenfrequencies have the dimension of energy so we have to divide those by two, the oscillator strengths are dimensionless so they do not have to be rescaled. Finally the prefactor has the dimension of $[\,\mathrm{J}\cdot\mathrm{m}^2\cdot\mathrm{C}^2]$ so we have to multiply the final result by two to arrive at a quantity in atomic units. The final expression in atomic units that is valid for the Ps is:

$$\alpha(i\omega) = 2\sum_{n=1}^{N}\frac{f_n}{(\tilde{\omega}_n/2)^2 + \omega^2}, \tag{4.21}$$

[1] Dalgarno and Victor defined the eigenfrequency without the expected $\hbar$.

with:

n	f_n	$\tilde{\omega}_n$(Ha)
1	0.44560	0.37646
2	0.29185	0.51711
3	0.20838	0.90146
4	0.05417	2.60497

4.3 Bound states

We gathered all the ingredients necessary to calculate the potential described by equations (2.1) en (2.2). We summarize the parameters and give the values we found in the case of 4 QLs with spin-orbit coupling. Inside the material, $z < z_0 = 2.39\,\text{bohr}$, the potential is given by the value of the work function of the material $V_0 = 9.67\,\text{mHa}$. The exponential repulsion for $z > z_0$ is determined by the work function and the electron decay length $l = 0.6781\,\text{bohr}$. The long range Van der Waals interaction is determined by the damping function (2.4), which has the electron decay length l as argument, and the Van der Waals constant (2.3). This constant depends on the atomic polarizability (4.21) and the dielectric function evaluated at imaginary frequencies. We can obtain the latter from the dielectric function shown in figure 3.4, by using the formula for analytic continuation (4.6). If we put everything together, we find that the Van der Waals constant is given by $C = 15.69\,\text{eV bohr}^3$. The potential is plotted in figure 4.2.

We now solve the Schrödinger equation in the effective potential we calculated. We use two different methods to calculate the possible binding energy of the Ps to be sure that the result does not depend on the method we used. In the shooting method, we integrate the Schrödinger equation:

$$-\frac{\psi''}{4} + V\psi = E\psi. \tag{4.22}$$

by rewriting it as a set of coupled linear differential equations:

$$\begin{cases} \psi' = f \\ f' = 4(V - E)\psi. \end{cases} \tag{4.23}$$

We still need boundary conditions to start integrating this equation. Because the wavefunction has to vanish at infinity, the solution for $z < z_0$, where $V(z < z_0) = V_0$ is constant, can be written as:

$$\psi(z < z_0) = e^{2\sqrt{V_0 - E}z}. \tag{4.24}$$

Here we divided the normalization constant away and we assumed that $E < 0$ since we are only looking for bound states. Very far away from the surface $z \gg 0$, we have $V(z \gg 0) \approx 0$, so that we can write the solution as:

$$\psi(z \gg 0) = Ae^{-2\sqrt{-E}z}. \tag{4.25}$$

We can thus start integration the equation at $z = z_0$ with the boundary conditions:

$$\begin{cases} \psi(z = z_0) = e^{2\sqrt{V_0 - E} z_0} \\ f(z = z_0) = 2\sqrt{V_0 - E}\, \psi(z = z_0) \end{cases} \tag{4.26}$$

towards some value z_1 for which $V(z_1) \approx 0$. At this border we have to check whether or not the boundary conditions of (4.25) are met:

$$\begin{cases} \psi(z = z_1) = Ae^{-2\sqrt{-E} z_1} \\ f(z = z_1) = -2A\sqrt{-E}\, \psi(z = z_1). \end{cases} \tag{4.27}$$

Or, if we divide the second of these equations by the first, we do not have to know the constant A:

$$\frac{f(z = z_1)}{\psi(z = z_1)} = -2\sqrt{-E}. \tag{4.28}$$

If this boundary condition is not met for a specific choice of E, we know that there is no bound state possible for that value. In practice, we swept over a range of energy values and plotted the left hand side of (4.28). Intersections between this line and the right hand side were then identified as bound states. The integration of the equation was performed with the Runge-Kutta method as implemented in the MATLAB function 'ode45'. We carried out a convergence study w.r.t. the value of z_1 by increasing it in steps of $\Delta z = 2\,\text{bohr}$ and found that for $z_1 = 14\,\text{bohr}$ the energy of the bound state was converged to within 1 meV. The result we found is there is that one bound state for Ps is possible with a binding energy of $E = -150\,\text{meV}$. We also plotted the probability density we found in figure 4.2 and the result confirms that a physisorbed Ps can be used to probe very selectively only the surface of the material. Indeed, the probability density is mainly located above the last atom of the surface and becomes negligible further than $5\,\text{bohr} = 2.65\,\text{Å}$ beyond this first atom.

In the second approach, we solve the equation numerically on a equidistant grid, i.e. we write the Schrödinger equation as:

$$-\frac{\psi_{i+1} + \psi_{i-1} - 2\psi_i}{4h^2} + V_i\psi_i = E\psi_i. \tag{4.29}$$

Finding the bound states then comes down to finding the negative eigenvalues of this matrix equation. We carried out a convergence study with respect to the boundaries[2], which we took symmetrically around $z = 0$. We found that $-25\,\text{bohr} \leq z \leq 25\,\text{bohr}$ was necessary to convergence the binding energy to within 1 meV. A converged value for the distance between the grid points was found to be $h = 0.01\,\text{bohr}$. We conclude from this calculation that at the surface of Bi_2Te_2Se a Ps bound state exists with an energy of $E = -150\,\text{meV}$, consistent with the previous result.

[2]Because beyond the boundaries the wavefunction is zero, a grid method always treats the problem as if the particle is localized in a box. This gives a spurious confinement energy contribution that can be eliminated by increasing the size of the box.

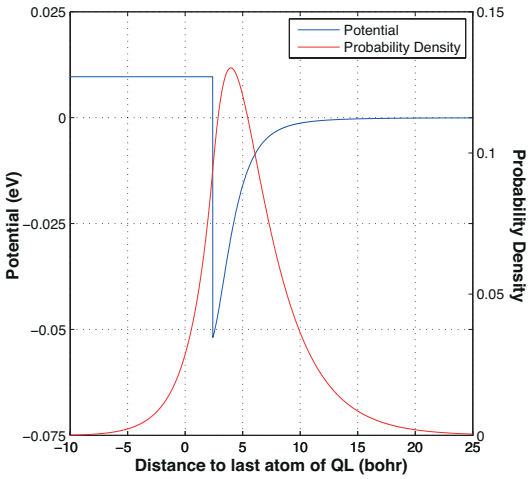

Figure 4.2: A plot of the effective potential for the Ps (blue line) and the resulting probability density of the Ps bound state in the well (red).

4.4 Influence of the parameters on the binding energy

Although we found that a Ps bound state exists near a Bi_2Te_2Se surface, it is interesting to evaluate the recipe in general. That is, determine the sensitivity of the energy of the bound state w.r.t. the different parameters. As a first step we determine the binding energy of the Ps as a function of the Van der Waals constant. Afterwards, we discuss this constant as a function of the frequency cutoff of the dielectric function and the dependence on the bandgap as well as the influence of the atomic dipole polarizability. This gives us an idea of what the most important quantities in the recipe are and where we can improve our approach.

4.4.1 Influence of the Van der Waals constant on the binding energy

The first step in our discussion of the importance of the different parameters, is to investigate how sensitive the binding energy is w.r.t. the Van der Waals constant. To do this, we solved the matrix equation (4.29) and looked how the lowest eigenvalue changed as a function of C. The result is shown in figure 4.3. We also investigated if it was possible for a second bound state to exist but we found none for $C \in [0, 27]\,\text{eV}$. In this step, we moved the right boundary to $100\,\text{bohr}$ because the wavefunction of the excited state will be more spatially extended than the lowest bound state. To avoid memory problems we had to change the step between the grid points to $h = 0.05\,\text{bohr}$.
The value we found for the Van der Waals constant is $C = 15.69\,\text{eV}\,\text{bohr}^3$. A deviation of $C \pm 1\,\text{eV}\,\text{bohr}^3$ around this value changes the binding energy with $\pm \sim 25\,\text{meV}$. From this calculation we can conclude that the existence of a bound state and possible extra bound states is quite insensitive to the exact

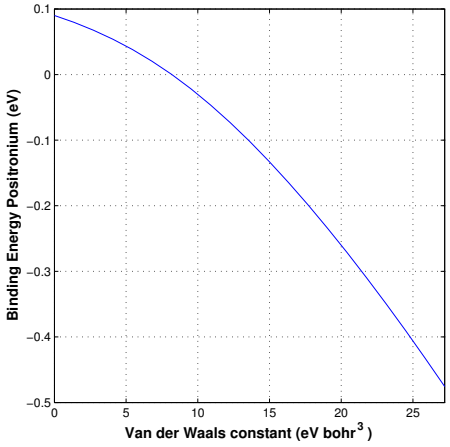

Figure 4.3: The binding energy of positronium as a function of the Van der Waals constant.

value of the Van der Waals constant, while the binding energy of the state feels a significant influence.

4.4.2 Influence of the bandgap

Even though we found that the calculated bandgap for Bi_2Te_2Se agrees very well with experimental data, this is certainly not always the case in DFT calculations. This is usually because the exchange term is not accounted for correctly by the simplest LDA and GGA functionals. Hybrid functionals, for which a Hartree-Fock calculation is carried out in addition to the DFT calculation, tend to get better results but are much more computationally intensive. It is thus worthwhile to determine wether the bandgap has a significant influence on the energy of the bound state. We do this by shifting the real and imaginary part of the dielectric function towards higher frequencies. The result is displayed in figure 4.4.
We find that, by shifting the spectrum by 100 meV towards higher frequencies, which roughly corresponds with a bandgap that is 100 meV larger, C changes from 15.69 eV bohr^3 to 15.99 eV bohr^3. This translates into a change in the binding energy of 7 meV. If one is dealing with a material for which LDA or GGA functionals predict the bandgap accurately in the order of $\sim$ 10 meV, it might not be worth the extra computational effort by using a hybrid functional. In the case where there is a large bandgap that is inaccurately predicted by LDA or GGA functionals, it might though be necessary to use a hybrid functional. If however, the bandgap is the only problem and the rest of the bands are predicted accurately, applying a scissor shift when calculating the dielectric tensor may be a much more computational efficient way to obtain accurate results. The scissor shift basically pulls open the bandgap to correspond with the experimental value. This shift in band energies will also lead to a shift of dielectric response towards higher frequencies but is more subtle than our crude approach here. For details, we refer to the article of Hughes [20] where the

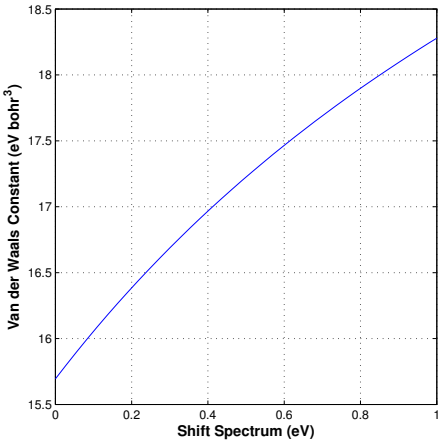

Figure 4.4: The Van der Waals constant as a function of the shift applied to the dielectric function.

adaptations to the linear response function under the scissor shift are discussed.

4.4.3 Influence of the frequency cutoff

We can expect that high frequencies do not have a significant influence on the Van der Waals constant, since from (3.9), (3.10) and (3.11), we see that the dielectric function falls off as $\sim 1/\omega^2$ and the analytic continuation (4.6) falls off as $\sim \epsilon_2(\omega)/\omega$. Despite that, we want some more quantitative results so we calculate the Van der Waals constant as a function of the frequency cutoff in the range of $\omega \in [0, 27]$ eV. The result is given in figure 4.5.

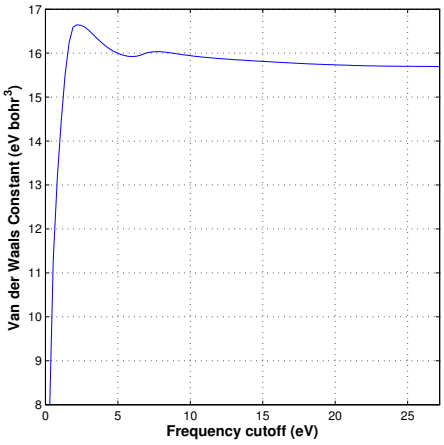

Figure 4.5: The Van der Waals constant as a function of frequency cutoff up to which the dielectric function is calculated.

The difference between the Van der Waals constant for a cutoff of 10 eV, which

includes all significant features of the dielectric function, and a cutoff of 27 eV, is 0.26 eV bohr^3. This results in a difference in binding energy of 6 meV, which is quite small. That aside, if we want to determine the binding energy within a precision of 1 meV, we should select a frequency cutoff that lies well above the significant features of the dielectric function. By this we mean that the real part of the dielectric function should be approximately 1 and the imaginary part approximately 0.

4.4.4 Influence of the atomic polarizability

So far, we used the parametrization of A. Dalgarno and G. A. Victor [13] to determine the polarizability of the positronium. The parameters in this paper are determined numerically and since it is a quite old calculation, we check if we cannot determine this quantity more accurately. Exact expressions for hydrogen like atoms exist today and we use the expression that is given in the introduction of R. Szmytkowskis paper [50]. In this paper he also derives a relativistic expression for the polarizability, but since Ps is very light, we expect that it only gives a negligible correction. The formulas given in the paper are:

$$\alpha_H(\omega) = \alpha_H^{(+)}(\omega) + \alpha_H^{(-)}(\omega), \tag{4.30}$$

where:

$$\alpha_H^{\pm}(\omega) = \frac{a_0^3}{Z^4}\frac{2^9(\xi^{\pm})^7}{(\xi^{(\pm)}+1)^{12}}\sum_{n=0}^{\infty}\binom{n+3}{n}\frac{(n+2-2\xi^{(\pm)})^2}{n+2-\xi^{(\pm)}}\left(\frac{\xi^{(\pm)}-1}{\xi^{(\pm)}+1}\right)^{2n-2} \tag{4.31}$$

with:

$$\xi^{(\pm)} = \frac{Z}{\lambda^{(\pm)}a_0} \quad , \quad \lambda^{\pm} = \sqrt{-\frac{2m(E^{(0)}\pm\hbar\omega)}{\hbar^2}} \quad , \quad E^{(0)} = -\frac{Z^2e^2}{2a_0}. \tag{4.32}$$

In these expressions we can put $Z = 1$ and we can rescale it to obtain an expression that is valid for positronium. That is we substitute $a_0 \to 2a_0$ and in $\lambda^{(\pm)}$ we divide by 2 under the root. This is because $2m/\hbar^2$ has units of $\left[1/\,\mathrm{J}\cdot\mathrm{m}^2\right]$. We calculated the expression at imaginary frequencies, where we truncated the sum after the first fifty terms since additional terms gave no corrections within the numerical precision of our computer. Somewhat surprisingly, the maximal relative difference in the polarizability obtained from the expression of Dalgarno's work and the analytic expression is as small as 0.1%. The difference in the Van der Waals constant is 1.43×10^{-4} eV bohr^3, which leads to a difference in binding energy of 3.60×10^{-3} meV. This value is far below the numerical precision we achieved with the methods we used to determine the binding energy. We can thus conclude that the atomic polarizability will certainly not be a source of error in our results.

4.4.5 Influence of the decay length

The electron decay length enters twice in our description of the effective potential for the Ps. The first time is to determine the exponential repulsion (2.5) due to the overlap of the electron with the electrons of the surface. The second is

to determine the strength of the damping function (2.4) for the Van der Waals interaction (2.2). We determined this quantity by making a fit to the electron density in a logarithmic density plot at the surface but the region where we made the fit could be open for discussion. We studied the effect on the binding energy as a function of this decay length. The result for a wide range of values is given in figure 4.6 but it is clear that the value of l should be determined quite accurately to achieve an accuracy of the binding energy in the meV range.

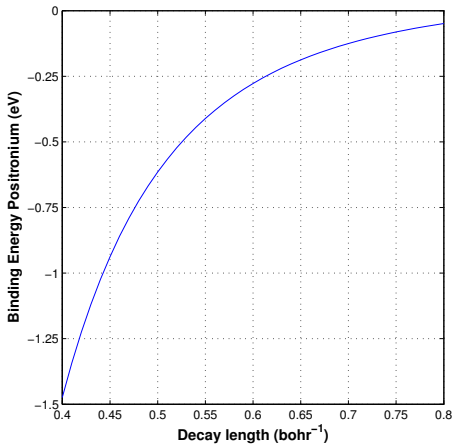

Figure 4.6: The binding energy of Ps as a function of the electron density decay length l.

So, how much does l vary if we change the region where we make the fit to the density? We checked this by making the interval to which we fitted our data smaller by moving the borders symmetrically away from the surface and the region where the numerical smallest representable value was approached. The value changed as little as $\Delta l = \pm 1 \times 10^{-3}$ bohr which corresponds with a difference in the binding energy of only 1 meV. The value of l changes more rapidly when moving out the region where the decay is purely exponential but this is an issue that can easily be avoided by making the fitting region smaller. We can conclude that, even though the binding energy is strongly dependent on the electron density decay length, for a given system it will not be critical in determining the binding energy of Ps, because the value can be accurately determined.

4.4.6 Influence of the work function

The last parameter in our model we did not yet check is the Ps work function. We assume that we are dealing with a perfect crystal such that the positron is delocalized over the solid. In this case the positron density at any given point is very low and we could determine the positron energy levels from the ground state electron density, for which we can assume it is not perturbed by the presence of the positron density. While this approximation is well justified, we can expect that if the bandgap of the material in question is inaccurately predicted,

the chemical potential for the particles and thus the Ps work function also are. This argument can be understood from our discussion of the Ps work function in the previous chapter. Indeed, the chemical potential is determined by the energy difference between the crystal zero, which does not depend on the energy functional used, and the Kohn-Sham levels, which do depend on the functional used. In figure 4.7 the dependence of the binding energy of Ps for a large range of values for the work function is given.

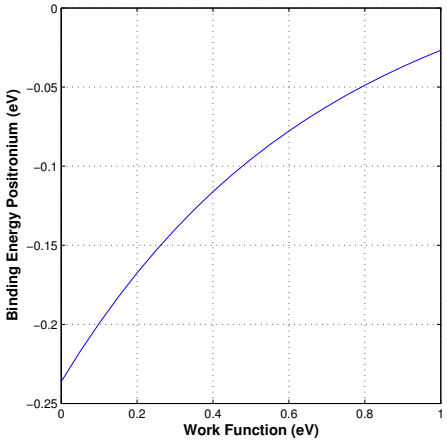

Figure 4.7: The binding energy of Ps as a function of the work function V_0.

We changed the work function by $\Delta V_0 = \pm 0.01\,\text{eV}$ and found that the binding energy changed with $\pm 3\,\text{meV}$, which shows that the binding energy is relatively strongly dependent on this quantity. We can conclude that the use of appropriate energy functionals is essential for an accurate determination of the Ps work function. For the electron exchange and correlation energy functional, the bandgap can serve as a measure of the accuracy while for the positron functional it is more difficult.

4.5 Influence of the edge states on the Ps bound state

In the previous chapter, we determined the effect of the edge state on the parameters in the Ps description and we now calculate their effect on the Ps binding energy. The parameters that are influenced by the edge state are the electron decay length l in the repulsive part of the potential and, as we argued in the previous chapter, the dielectric function in the attractive part of the potential. To study the effect of the edge states, we found that excluding the spin-orbit coupling is in general a poor approach since the effect of the edge state is small in comparison with other differences. Either way, the effect on the electron density decay is very small and likewise the difference in binding energy. We show the results below:

1 QL with SO	$l = 0.6771\,\text{bohr}$	$E = -151\,\text{meV}$
4 QLs with SO	$l = 0.6781\,\text{bohr}$	$E = -150\,\text{meV}$
4 QLs without SO	$l = 0.6761\,\text{bohr}$	$E = -152\,\text{meV}$

We argued that for the attractive part, we should take the dielectric response of the surface instead of the dielectric response of the bulk. We calculated the dielectric response of a slab consisting of 1 QL as well as 4 QLs to see the effect of the metallic edge state. We now calculate the binding energy of the Ps in the case where we rescaled the output to correspond with a thin film consisting of 1 QL or 4 QLs as well as where we rescaled the output to correspond with surface dielectric tensor of a semi-infinite surface. The effect on the Van der Waals constant and the binding energy of the Ps by rescaling the output to correspond with a thin film is given by:

Bulk	$C = 15.69\,\text{eV}\cdot\text{bohr}^3$	$E = -150\,\text{meV}$
1 QL with SO	$C = 15.79\,\text{eV}\cdot\text{bohr}^3$	$E = -152\,\text{meV}$
4 QLs with SO	$C = 15.47\,\text{eV}\cdot\text{bohr}^3$	$E = -144\,\text{meV}$

The results obtained by rescaling the dielectric tensor with the sum rules, i.e. to correspond with a semi-infinite solid, are given by:

Bulk	$C = 15.69\,\text{eV}\cdot\text{bohr}^3$	$E = -150\,\text{meV}$
1 QL with SO	$C = 15.16\,\text{eV}\cdot\text{bohr}^3$	$E = -137\,\text{meV}$
4 QLs with SO	$C = 17.27\,\text{eV}\cdot\text{bohr}^3$	$E = -188\,\text{meV}$

In the case of the thin film, it is surprising that the Van der Waals constant is actually smaller than in the case of 1 QL because we intuitively expect a larger response from the 4 QLs. Although the differences in the binding energy are larger than in the case of the electron decay length, they can be considered small since they are still situated in the meV range.
The case where modeled a semi-infinite solid by rescaling the dielectric tensor with the sum rule discussed in the previous chapter, shows a very different picture. Here, we clearly see that the increased response at low frequencies due to the edge state leads to a larger Van der Waals constant, with an improved binding of the Ps to the surface as a consequence. The relative difference in the binding energy we find when using the dielectric function for the 4 QLs or the bulk is 22% while between the 1 QL and 4 QLs cases, this relative difference is 31%.
We would like to point out that, although it gives an idea of the importance of the edge states, the method of rescaling the dielectric tensor is in fact somewhat ad hoc. If we want to treat this effect more rigorously, we should use the description of the Van der Waals interaction in terms of the surface's density-density response function derived in Zaremba and Kohn's paper [57], equations (A.45), (A.46) and (A.47). The description we used so far is an approximation of these formulas.

Chapter 5

Graphene

In this chapter we study Ps bound states near graphene. The approach is very similar as for Bi_2Te_2Se with the exception that, because graphene is a two dimensional system, we do not have bulk properties. In 2005, Kane [23] predicted that the spin-orbit coupling in graphene can open a finite bandgap and causes an electronic structure that is topologically distinct from an ordinary insulator. In this quantum spin hall phase, two states with opposite spin and momentum exist at each of the edges of a finite graphene sheet. The first-principles study of Yao [56] shows, however, that the bandgap caused by the spin-orbit coupling is as small as 10^{-3} meV and that these states can likely not be observed for temperature above $T = 0.02$ K. Because of this we will not look into the effects of these states on the binding energy of Ps.
In the first section of this chapter we present the results from the first-principles study, which are the electronic structure, the dielectric function, the electron density and the Ps work function of graphene. In the second section we apply the recipe from the previous chapter to determine if Ps bound states are possible.

5.1 First-principles study

5.1.1 Introduction

Crystal structure: Graphene exhibits a honeycomb type of lattice, where the nearest neighbor distance is given by $a_0 = 1.42$ Å $= 2.68$ bohr [35]. Figure 5.1 shows the crystal structure and the first BZ. In cartesian coordinates, the unit vectors are given by:

$$\begin{aligned} \mathbf{a}_1 &= \frac{a_0}{2}(3, \sqrt{3}) \\ \mathbf{a}_2 &= \frac{a_0}{2}(3, -\sqrt{3}) \end{aligned} \tag{5.1}$$

and the fractional positions of the carbon atoms in the unit cell by:

$$\begin{aligned} C_1 &= (1/3, 1/3) \\ C_2 &= (2/3, 2/3). \end{aligned} \tag{5.2}$$

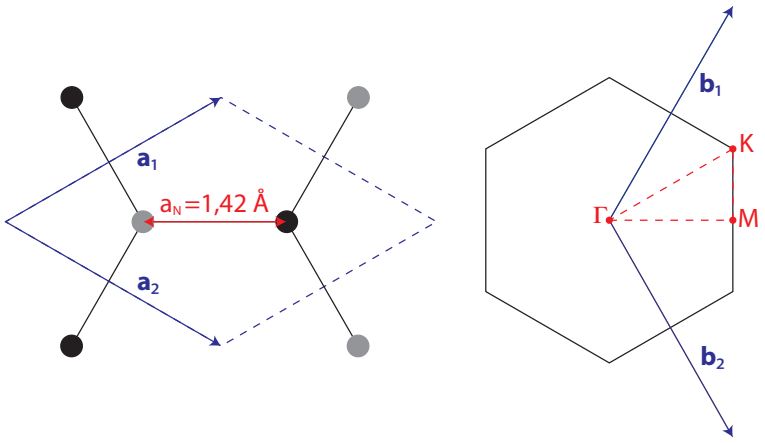

Figure 5.1: The left figure shows the crystal structure of graphene, where the two inequivalent carbon atoms of the lattice have been given a different color. The right figure shows the first BZ and the high symmetry points in it. The dashed red line shows the path followed for plotting the bandstructure.

Computation parameters for Elk: Unless mentioned otherwise, the first-principles calculations we present were carried out with the DFT code Elk. Just as for Bi_2Te_2Se, we carried out the convergence study w.r.t. the k-grid and the basis set. We started with a convergence study w.r.t. the k-grid until the difference in the total energy was less than 1 meV. The parameters that have to do with the basis set were raised in steps of 1, with the exception of rgkmax, the plane wave cutoff, which was raised in steps of 0.5. The occupancy of the energy levels is determined by the Fermi-Dirac distribution at room temperature. We took 10 empty bands into account and included the local orbitals because these are required to determine accurately the energy of high lying bands, which is important for the calculation of the dielectric function. The list of converged parameters and the other parameters in the calculations are given below. The meaning of each of these parameters can be found at the end of appendix B.

kgrid	30 30 1	rgkmax	7.5
gmaxvr	14	lmaxvr	7
lmaxmat	8	lmaxapw	8
nempty	10	lorbcnd	true
epsengy	1×10^{-5}	epspot	1×10^{-7}
stype	Fermi-Dirac	swidth	9.5×10^{-4}

In the calculations, we did not take spin-orbit coupling into account because carbon is such a light element that these corrections are negligible. The exchange and correlation function that we used is the PBE GGA, the same one as we used for Bi_2Te_2Se.
We relaxef the structure and found no difficulties in the case of graphene. We determined the optimal value for the nearest neighbor distance by calculating the total energy for $a_N \in \{0.98, 0.99, 1.00, 1.01, 1.02\} \times a_0$ and then making a parabolic fit to the total energy as a function of a_N. We found the minimum to lie at $a_N = 2.67$ bohr. Afterwards, the atomic position of C_2 was shifted slightly

away from its experimental equilibrium position (which is fixed by symmetry) and then we carried out the internal relaxation. The result was that the atom moved back towards $(1/3, 1/3)$, which is the value we take in the rest of the DFT study.

5.1.2 Band structure

Before we calculate the dielectric function of graphene, we check if we manage to reproduce the correct electronic structure. The bandstructure was calculated along the high symmetry directions in the Brillouin zone, shown in figure 5.1. Figure 5.2 shows the result, which determines graphene as a zero-bandgap semiconductor with a linear dispersion near the K-point. This forms one of the well-known properties of graphene [7].

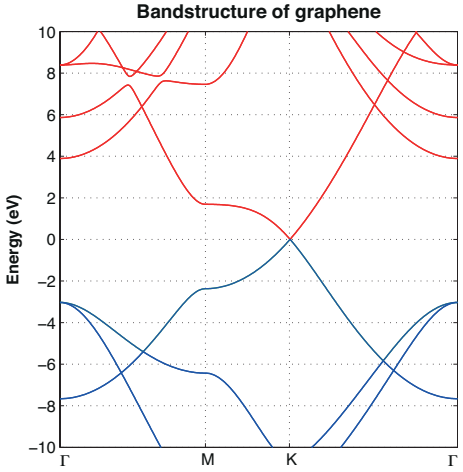

Figure 5.2: The bandstructure of graphene along the high symmetry directions in the Brillouin zone.

Our result is in reasonable agreement with the first-principles calculation shown in the paper of Zhang et al. [59]. The lower part of the spectrum is nearly identical but at the Γ-point, the second conduction band shows strong dispersion, so that at the Γ-point it ends up with an energy of $\sim 9\,\mathrm{eV}$ w.r.t. the Fermi-energy. Their calculation was, however, carried out with a LDA functional and with a full-potential linearized muffin-tin orbital method. This method is similar to the FLAPW method but in the interstitial region, Hankel functions are used as the basis instead of plane waves. In their paper, they did not mention that conduction local orbitals were included in the basis, so that we can argue that our result should, in principle at least, be more accurate. Another result was presented by Mohan [30], where the bandstructure was calculated with local numerical orbital method with a norm conserving pseudopotential and with the PBE functional. The valence bands shown in this paper are also in close agreement with our result but the conduction bands are strongly shifted towards higher energies, with exception of the first conduction band near the K-point. At the Γ-point, the conduction band minimum is located near $\sim 8\,\mathrm{eV}$ w.r.t. the

Fermi-energy. An explanation for the differences in the conduction states can be found in the thesis of O. Leenaerts [26]. The nearly parabolic bands that we see in the spectrum are there because we use periodic boundary conditions in three dimensions and correspond with free electron states. By increasing the size of the vacuum, these states shift down in energy because they are less confined in the direction perpendicular to the graphene plane. In the limit of an infinitely large box in this direction, these states form a continuum, starting from the vacuum energy level. A fourth result we cite, is a detailed GW calculation carried out by Schilfgaarde [53], who started with a ground state density calculation with a LDA functional. An interesting result shown in their paper, though, is that there is a significant correction to the dispersion of the bands near the K-point. The experimental value of the Fermi-velocity of the massless Dirac particles, which is obtained from the slope of the Dirac cone at the K-points, is given by 1.1×10^6 m/s. The LDA result from the paper is 0.82×10^6 m/s, which is an underestimation of 25%, while their most accurate prediction from GW is given by 1.20×10^6 m/s, which is an overestimation of 9%. A second correction is a shift of the valence band maximum at the Γ-point towards $\sim 5\,\text{eV}$ w.r.t. the Fermi-energy.
To summarize, DFT results in literature agree on the location of the valence bands and the lowest conduction band near the K-point. The dispersion near the K-point, however, shows a significant correction due to excitonic effects, as found by GW calculations and in agreement with experiment. In the conduction spectrum of the bandstructure, we have free electron states and the energy of these states are determined by the amount of vacuum in the cell.
We are not able to carry out GW calculations since this feature is not implemented in the Elk code. Our results will thus be approximate and the question raises if we could not better use 'exact' results available in literature for the properties we are interested in. The exact results in literature we refer to are derived for the low energy excitation around the K-points, which are described by the massless Dirac (Weyl) equation. We need the dielectric tensor up to high frequencies in order to carry out the analytic continuation (4.6) to imaginary frequencies. The high frequencies correspond with energies for which this effective description is no longer valid and this is why we refrain from using these results.

5.1.3 Charge density

To determine the electron decay length l and the background edge position z_0, we averaged the charge density again over a 25×25 grid in the unit cell. Afterwards we plotted the logarithm of this averaged density as a function of z. The region in this plot where we have a linear dependence on z, tells us where the electron density is decaying exponentially. We made a linear fit in the region $z \in [2.5, 4.0]$ bohr using linear regression and this gave us a value for the electron decay length of $l = 0.5457 \pm 0.0003\,\text{bohr} = 0.2888 \pm 0.0002\,\text{Å}$. The value of z_0 was determined by the first point, starting from the interval of the fit and moving towards the material, where the relative difference between the electron density and the linear fit was more than 1%. The result we found in this way is given by $z_0 = 1.64\,\text{bohr} = 0.87\,\text{Å}$.

5.1.4 Dielectric function

We calculate the dielectric function in the same manner as for Bi_2Te_2Se: First, we obtain the ground state to determine the Kohn-Sham energy levels. The occupancy of these states is determined by the Fermi-Dirac distribution at room temperature. Afterwards we calculate the optical conductivity with a smearing of $\eta = 0.01\,\text{Ha}$, from which the dielectric tensor is obtained.
We should check if the free electron bands give no significant contribution by increasing the vacuum in the cell. We started with a c-axis of 3.0 Å and increased it with steps of 0.5 Å up 7.0 Å. By doing this we found that the peak positions for the ϵ_{xx} and ϵ_{yy} components of the dielectric tensor stayed at the same position but decreased in amplitude as the size of the vacuum increased. This decrease in amplitude also happens for the ϵ_{zz} component but some absorption peaks in the imaginary part of the dielectric function also shift to lower frequencies when we include more vacuum. From these two observations, we can conclude that the vacuum levels only have an influence on the absorption in the direction perpendicular to the plane. The scaling of the amplitude with the size of the vacuum, we can understand by looking at the formula which is implemented to calculate the optical conductivity, equation (3.11). Indeed, the integral is replaced by a sum over the k-points determined by the chosen grid, in which each k-point has a weight determined by a finite volume element. In the case of graphene, we are dealing with a two dimensional crystal so we select a k-grid with only one point in the k_z direction. This means that the volume element is determined by the length of the reciprocal basis vector of the c-axis, i.e. the optical conductivity scales as $1/c$. This is indeed what we found by plotting the amplitude of a certain point of the spectrum against $1/c$. If we multiply with the length of the c-axis, we remove this scaling but then we obtain a optical conductivity with the dimension of length. This is something we do not want and to obtain a dimensionless result, we divide again with the thickness of the graphene layer for which we can take twice the background edge position z_0. The relations between the optical conductivity and the dielectric tensor (3.9) and (3.10) tell us that we have to rescale our result as:

$$\epsilon_1 \to \frac{c}{2z_0}(\epsilon_1 - 1) + 1 \quad \text{and} \quad \epsilon_2 \to \frac{c}{2z_0}\epsilon_2 \tag{5.3}$$

We show the result in figure 5.3, where we also included the intraband contribution (3.7) to the dielectric tensor.

5.1.5 Work function

As before, we used Abinit to calculate the work function of graphene. As a first step we carried out the convergence study with respect to the plane wave cutoff for the wavefunction and the density, for which we found 30 Ha and 80 Ha to be necessary to converge the total energy to within 1 meV. The PAW data for the carbon atoms was taken from the Abinit website. The energy functional we used for calculating the ground state is the PBE functional. The positron state in turn was calculated with the GGA of Barbiellini [10].
In the calculations we had four valence electrons per carbon atom so that in total we have eight occupied states at each k-point. From the bandstructure, we know that the valence band maximum is located at the K-point. The value

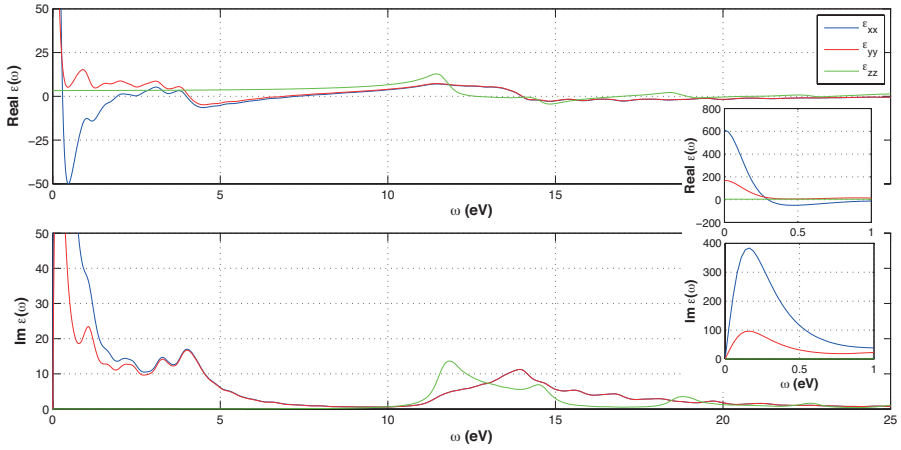

Figure 5.3: Plot of the real and imaginary parts of the components of the dielectric function of graphene calculated with 6 Å in the cell. The inset shows the values for small frequencies.

we find is $\mu^- = -0.02108\,\mathrm{Ha}$ while for the positron state at the Γ-point we find $\mu^+ = -0.17923\,\mathrm{Ha}$. The value for the Ps work function is thus given by $\Phi_{Ps} = -0.04904\,\mathrm{Ha} = -1.35\,\mathrm{eV}$.

5.2 Bound states

We solve again the Schrödinger equation for Ps in the effective potential as described in section 2.1. From the DFT study, we already determined the dielectric function, the electron decay length l, the background edge position for which we assume it is the same as the Van der Waals reference plane position $z_0 = z_{VW}$ and the work function V_0. We do the analytic continuation of the dielectric function in the same way as described in section 4.1. We use the exact formulas given in section 4.4.4 for the atomic polarizability.
Before we calculate if there is a possible bound state, we check the convergence of the Van der Waals constant value w.r.t. the amount of vacuum in the cell. Starting from 4.5 Å in the cell, we found this value converges to within 10 meV and from our discussion in the previous chapter, we know this should give a binding energy with a precision of 1 meV. In the rest of the calculation, we use the value we found for the largest unit cell, with 6.0 Å of vacuum, which gives a result of $C = 17.27\,\mathrm{eV}\cdot\mathrm{bohr}^3$. This is higher than in the case of bulk Bi_2Te_2Se and we can attribute this to the Drude contribution to the dielectric tensor at low frequencies.
We carried out the calculation on an equidistance grid $z \in [-25, 25]\,\mathrm{bohr}$ with a grid spacing of $h = 0.0075\,\mathrm{bohr}$ in which we first considered an asymmetrical potential well, i.e. we took $V(z) = V_0$ for $z < z_0$. This is a rough model for the potential well the Ps would feel if the graphene sheet lies on a substrate. In principle, following the recipe, we should take the work function of Ps in the substrate for $z < -z_0$ and we should calculate the dielectric tensor for the

graphene-substrate composite but we do not address this situation here. We found a single bound state with a binding energy of $E = -253\,\text{meV}$. If we consider suspended graphene, however, the potential well is symmetric around $z = 0$. Actually, for any material with inversion symmetry, we have a symmetrical potential well but if the material is sufficiently thick, we expect that this does not have any influence on the bound state. We carried out the calculation again but this time with a symmetrical potential well, where we took the same interval and grid spacing as before. In this case we found two bound states with an energy of $E = -383\,\text{meV}$ and $E = -133\,\text{meV}$, which shows that there is a significant difference with the asymmetrical case. We show the bound states and potential of both cases we considered in figure 5.4.

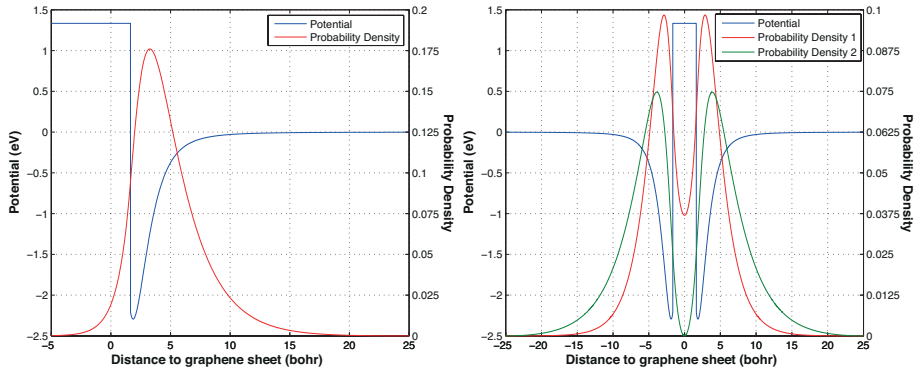

Figure 5.4: Plots of the potential and bound states in the case of the asymmetrical potential well (left) and the symmetrical potential well (right). In the right figure, the red curse shows the state with a binding energy of $E = -383\,\text{meV}$ and the green curve shows the state with a binding energy of $E = -133\,\text{meV}$.

For completeness, we prove that a bound state always exists if we consider a symmetrical potential well. We divide the solution in three parts, the first is $\psi_1(z < -z_1)$, the second $\psi_2(-z_1 < z < z_1)$ and the third $\psi_3(z > z_1)$, where $z_1 \gg z_0$ is far away from the surface. Since we are searching for bound states, we have $E < 0$ and the solutions in the first and third region, where $V(z) = 0$, can be written as:

$$\psi_1(z) = Ae^{2\sqrt{-E}z} \quad \text{and} \quad \psi_3(z) = De^{-2\sqrt{-E}z}, \tag{5.4}$$

where we used atomic units and we assumed we are dealing with the Schrödinger equation for a Ps atom. Because the potential well is symmetrical around $z = 0$, $\psi_2(z)$ can be expanded as:

$$\psi_2(z) = \sum_{i=0}^{\infty} B_i \sin(k_i z) + C_i \cos(k_i z), \tag{5.5}$$

where the k_i are determined by the details of the potential $V(z)$. From very general considerations, Feynman argued that for bosons the many-body ground state wavefunction has to be positive-definite in the coordinate representation.

The same argument can be applied here. Indeed, imagine that we start from a wavefunction that is negative somewhere. Since the physics is determined by the probability density, we can just as well take the absolute value of this wavefunction because it gives the same probability density and thus the same energy. This argument also follows from the Honenberg-Kohn theorems that tell us that the ground state energy can be determined from the density, which equals the norm of the wavefunction in this case. At the location of the node, we now have a kink in the wavefunction. The wave function we have now does certainly not represent the ground state since kinetic energy can be lowered by smoothing the wave function near this point. We thus have to conclude that the wave function has to be positive everywhere and thus has to be symmetric around $z = 0$. As a consequence, we have $A = D$ and any sines in the expansion of $\psi_2(z)$ can be excluded. If we now write out the matching of the value of wavefunction and its derivative, we arrive at the two conditions:

$$\begin{aligned} Ae^{-2\sqrt{-E}z_1} &= \sum_{i=0}^{\infty} C_i \cos(k_i z_1) \\ 2\sqrt{-E}Ae^{-2\sqrt{-E}z_1} &= \sum_{i=0}^{\infty} C_i k_i \sin(k_i z_1), \end{aligned} \tag{5.6}$$

or, if we divide the second by the first:

$$2\sqrt{-E} = \frac{\sum_{i=0}^{\infty} k_i C_i \sin(k_i z_1)}{\sum_{i=0}^{\infty} C_i \cos(k_i z_1)}. \tag{5.7}$$

Since the left hand side is a positive constant, we can always determine a set of C_i such that this condition is satisfied. In other words, there is *always* a bound state[1]. This does, however, not mean that this bound state is always relevant for experiment since it is possible that its binding energy is very low.

[1]It might seem from the boundary condition that for any value of E, we can find an appropriate set of C_i such that it is satisfied, which is in fact perfectly true. We should keep in mind, however, that the boundary condition itself only holds for the ground state energy $E = E_g$.

Chapter 6

Improved Ps bound state description

In the chapter four, we identified that the work function and the electron decay length play an important role in determining the energy of the Ps bound state. Even though we can determine those quantities with high precision, the question rises how valid the Ps description we used so far is close to the surface. The short range description of the potential is a simple approximation and instead of trying to derive a more accurate expression for this potential, we wonder if it is valid to describe the Ps as a neutral particle when it comes close to the surface. After all, the positron likely feels an attractive force from the electron density near the surface while the electron gets repelled. The current description might fail to capture this accurately and this is why we try to set up a two particle description in this chapter. Once we have such a description, we can see what it predicts for the binding energies of the Ps and see if they are consistent with the previous model.
The first section of this chapter is devoted to setting up the Hamiltonian of the two particle system we consider. In the subsequent section, we discuss in detail how we solve the resulting Schrödinger equation.

6.1 Hamiltonian set up and discussion

One way to improve upon the Ps description is to use DFT calculations. We could for instance take a slab and add an extra electron and positron to the cell and then calculate their eigenstates and wavefunctions self-consistently. While it is certainly possible, carrying out a two-component DFT calculation is a computational very demanding task, because we would not have one self-consistent loop (for the electron density) but three. The first extra loop is required to calculate the positron state in a fixed electron density and can be carried out quickly so it does not form the problem. The second loop, however, requires to recalculate the electron (positron) density after the positron (electron) density has been found. If we are dealing with large unit cells, this is not exactly a feasible approach. This is why instead we set up a two-particle description in which we take the contribution of the solid into account as some fixed input. Furthermore, such an approach simplifies the setup of an effective potential for

the neutral Ps atom since in the DFT description, the extra electron would not be distinguishable from the rest of the electrons in the solid.

In 1985, Cuthbert published a paper in which he studied the physisorption of a Ps atom to a metal surface [11]. He also used a two-particle description and considered following Hamiltonian:

$$\hat{H} = -\frac{1}{2}\nabla_e^2 - \frac{1}{2}\nabla_p^2 - \frac{1}{|\mathbf{r}_e - \mathbf{r}_p|} + \hat{H}_{\text{plasma}} + \hat{H}_{\text{int}} + \hat{H}_{\text{step}}, \tag{6.1}$$

where the first three terms form the Hamiltonian for the isolated electron-positron system. The fourth term is the Hamiltonian of the metal, which is modeled by a gas of non-interacting plasmons. The fifth term describes the interaction energy of the particles with the plasmon gas. The last term was introduced because the plasmon picture fails to describe the correct energy of an electron and positron in the bulk of the metal. It is taken such that if an electron or positron are located inside the material, their energy is given by their respective work functions. The model is too simple to accurately predict the Ps binding energy, which is our goal, because it does not accurately describe the short-range effects. It does give some important insights, however, that we will take into account when proposing our model. More specifically, Cuthbert derived expressions such that all attractive effects of the metal are contained in effective potentials for the electron and positron. This effective potential consists of three terms, the first two are the effective potentials for the electron and positron separately. The leading order term far away from the surface is given by the classic image potential. The third term depends on the position of both the electron and positron and describes the interaction of the electron with the image charge of the positron and the other way around. The most important thing is that the combination of these three terms leads to the correct $1/Z^3$, where Z is the distance of the Ps to the surface, dependence for large distances, which we expect for the neutral Ps atom.

If we want to accurately predict Ps binding energies to the surface, we need a description of the interaction between the two particles and the solid that is more accurate than the one in Cuthberts paper. Even though we argued that we will not use DFT to calculate the electron and positron states self-consistently, we can still use the theory to derive accurate potentials for both particles. If we keep the ground state electron density of the solid fixed, we can calculate the Coulomb and Kohn-Sham potential for the electron and the positron using an appropriate energy functional. This is in fact what we will do and it will deliver us some effective potential V_S that depends on the position of the particle in question. How exactly we are going to calculate this potential, is discussed later. We should realize though, that LDA and GGA functionals fail in describing the long range interactions of the image potentials, which is crucial certainly if we want to make the connection with the previous description. We correct for this shortcoming by taking the classical electrostatic energy along, which gives the correct long-range description. We discuss how we interpolate between the two later on in this chapter.

Based on our discussion so far, we propose the following two particle Hamil-

tonian:

$$\hat{H} = -\frac{\hbar^2}{2m_e}\nabla_e^2 - \frac{\hbar^2}{2m_p}\nabla_p^2 + V_S(\mathbf{r}_e) + V_S(\mathbf{r}_p) + W(\mathbf{r}_e, \mathbf{r}_p), \tag{6.2}$$

where $W(\mathbf{r}_e, \mathbf{r}_p)$ is the electrostatic energy. The $V_S(\mathbf{r}_{e,p})$ determines the interaction energy of the two particles with the solid. In principle, this potential should contain completely the effect of the solid but as discussed before, it fails to describe the long range interaction. We include the classical electrostatic energy to compensate for this problem [48]:

$$W(\mathbf{r}_e, \mathbf{r}_p) = \frac{1}{2}\int d\mathbf{r}\left[e\delta(\mathbf{r}-\mathbf{r}_e) - e\delta(\mathbf{r}-\mathbf{r}_p)\right] \times \left[V(\mathbf{r}, \mathbf{r}_e) - V(\mathbf{r}, \mathbf{r}_p)\right]. \tag{6.3}$$

Here $V(\mathbf{r}, \mathbf{r}_{e,p})$ is the electrostatic potential at position $\mathbf{r}$ due to a charge at position $\mathbf{r}_{e,p}$. The potential, that we derive in appendix C, is given by[1]:

$$V(\mathbf{r}, \mathbf{r}_{e,p}) = \frac{e}{\sqrt{\varrho^2 + (z - z_{e,p})^2}} - \frac{e_i}{\sqrt{\varrho^2 + (z + z_{e,p})^2}} \quad z > 0, \tag{6.4}$$

where we adopted cylindrical coordinates (with the strange looking rho to avoid confusion with the densities), $z_{e,p}$ denotes the distance of the charge to the 'surface'[2], ϱ the polar distance to the charge and [16]:

$$e_i = \left(\frac{\chi_e}{\chi_e + 2}\right) e. \tag{6.5}$$

Here, e is the charge of the electron. The electric susceptibility of the solid χ_e is related to the dielectric constant by:

$$\epsilon = 4\pi(1 + \chi_e) \quad \Rightarrow \quad \chi_e = \frac{\epsilon}{4\pi} - 1, \tag{6.6}$$

where the dielectric constant is obtained from $\epsilon = \lim_{\omega \to 0} \epsilon(\omega)$. As pointed out for Bi_2Te_2Se, the dielectric constant is different depending on wether metallic edge states are present or not. This allows us to investigate the influence of these states again. If we work out the electrostatic energy (6.3), we end up with four terms:

$$\begin{aligned} W(\mathbf{r}_e, \mathbf{r}_p) &= \frac{e}{2}\left[V(\mathbf{r}_e, \mathbf{r}_e) + V(\mathbf{r}_p, \mathbf{r}_p) - V(\mathbf{r}_e, \mathbf{r}_p) - V(\mathbf{r}_p, \mathbf{r}_e)\right] \\ &= \frac{e}{2}\left[-\frac{e_i}{2z_e} - \frac{e_i}{2z_p} - \frac{2e}{\sqrt{\varrho^2 + (z_e - z_p)^2}} + \frac{2e_i}{\sqrt{\varrho^2 + (z_e + z_p)^2}}\right]. \end{aligned} \tag{6.7}$$

To go from the first step to the second, we dropped the divergent self-interaction terms of the electron en positron since we know they should not be there. The first two describe the interaction between the electron and the positron with their own image charge. The third term is the Coulomb interaction between the

[1] We changed the sign of the induced charge because then it becomes clearer which terms give an attractive or repulsive contribution.

[2] In classical electrostatics, the surface of the material is well-defined but in a microscopic theory it is not. The discussion is similar to the position of the Van der Waals reference plane. If we would start from a microscopic description to derive the image potential, we could likely find an expression that defines the position of the image plane.

pair and the last term is the interaction of the electron and positron with the image of the other particle. We give an overview of the interactions in figure 6.1. Note that the interaction is a function of only the distance between the two particles and the distance between each of them and the solid $W(\mathbf{r}_e, \mathbf{r}_p) = W(\varrho, z_e, z_p)$. From our discussion of Cuthberts paper, we are confident that the image potentials give us the correct $1/z^3$ dependence of the Van der Waals attraction at large distances for the neutral composite.

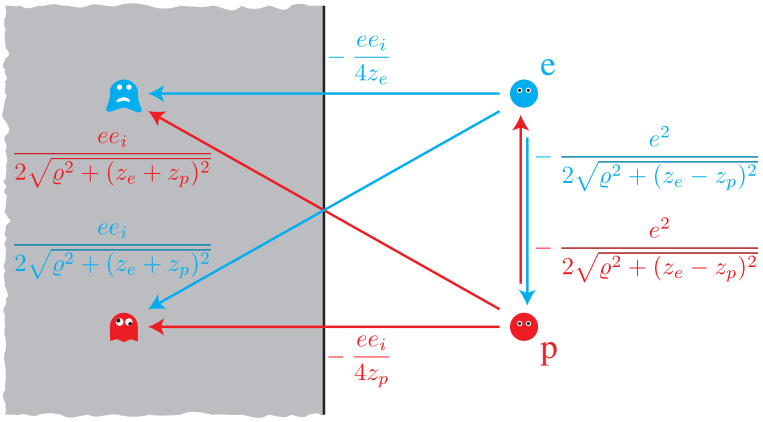

Figure 6.1: An overview of the contributions to the electrostatic energy due to the interaction between the electron and positron.

In the expression for the electrostatic energy, we assumed that the position of the surface is given by $z = 0$, which we chose at the position of the last atom of the surface. In a microscopic theory, the 'edge' of a material is, however, ill defined and it is likely not situated at this position. The discussion is analogous to the discussion of the position of the Van der Waals reference plane. One can likely derive an expression for the image potential reference plane position by starting from a microscopic theory to derive this interaction. We assume that we can just take $z_{im} = z_0$, for which we determined the value in the previous chapter. The image charge contribution of electrostatic energy diverges when $z_{e,p} \to z_{im}$. We discussed, however, that we only need this term to correctly incorporate the long-range interaction. Therefore we cut off the image charge contribution with a Heaviside function at some $z_1 > 0$, that for instance can be chosen at the point far from the surface where the image potential becomes larger in magnitude than the exchange and correlation potential. The final form of the electrostatic energy is:

$$\begin{aligned} W(\mathbf{r}_e, \mathbf{r}_p) &= V_{im,e}(z_e) + V_{im,p}(z_p) + V_C(\varrho, z_e, z_p) + V_{ci}(\varrho, z_e, z_p) \\ &= -\frac{ee_i\,\theta(z_e > z_1)}{4(z_e - z_{im})} - \frac{ee_i\,\theta(z_p > z_1)}{4(z_p - z_{im})} - \frac{e^2}{\sqrt{\varrho^2 + (z_e - z_p)^2}} \\ &\quad + \frac{ee_i\,[\theta(z_e > z_1) + \theta(z_p > z_1)]}{2\sqrt{\varrho^2 + (z_e + z_p - 2z_{im})^2}}, \end{aligned} \tag{6.8}$$

where we introduced the notations $V_{im,e}, V_{im,p}, V_{ci}$ for the electron, positron and cross-image potentials respectively as well as V_C for the Coulomb potential.

We assume that the ground state density of the solid will not be perturbed by the presence of the extra electron and the positron. This is of course an approximation but, as discussed previously, if we would not make it, we would end up solving the two component DFT problem self-consistently. We can write the particle-solid interaction energy as:

$$V_S(\mathbf{r}_{e,p}) = V_{C,S}(\mathbf{r}_{e,p}) + V_{XC}(\mathbf{r}_{e,p}) \tag{6.9}$$

The Coulomb potential for the particles $V_{C,S}$ is a fixed input to the problem since it only depends on the charge density of the solid. The exchange and correlation energy is somewhat harder because, in principle, it depends on the total density so each time we update our wave function, these terms should have to be recalculated. From the density of the solid and the density of the electron or positron, we can calculate the exchange and correlation potential for the respective particles. We model the exchange and correlation energy between the solid and the electron by the Perdew-Zunger LDA functional [39] and the exchange and correlation energy between the positron and the solid by the LDA functional given in [14]. We give the required expressions for the latter in appendix D since it is not implemented in Elk. As a final step, we will average the potentials over the unit cell such that it becomes a function of z only:

$$V_S(\mathbf{r}_{e,p}) \to V_S(z_{e,p}). \tag{6.10}$$

This approximation makes the problem considerably easier.

6.2 Solution for the Schrödinger equation

First proposition: Transformation to center of mass coordinates. Since the electrostatic interaction is only a function of the distance between the two particles and the distance between the particles and the solid, we can adopt center of mass coordinates in the plane:

$$\begin{aligned} &X = \frac{m_e x_e + m_p x_p}{M}, \quad Y = \frac{m_e y_e + m_p y_p}{M}, \quad x = x_e - x_p, \quad y = y_e - y_p, \\ &M = m_e + m_p, \quad \frac{1}{\mu} = \frac{1}{m_e} + \frac{1}{m_p} \end{aligned} \tag{6.11}$$

If we carry out the transformation and if we adopt polar coordinates for the relative coordinates, then we find:

$$\begin{aligned} \hat{H} = &-\frac{\hbar^2}{2M}\left(\frac{\partial^2}{\partial X^2} + \frac{\partial^2}{\partial Y^2}\right) - \frac{\hbar^2}{2\mu}\frac{1}{\varrho}\frac{\partial}{\partial \varrho}\left(\varrho\frac{\partial}{\partial \varrho}\right) - \frac{\hbar^2}{2\mu}\frac{1}{\varrho^2}\frac{\partial^2}{\partial \theta^2} - \frac{\hbar^2}{2m_e}\frac{\partial^2}{\partial z_e^2} \\ &- \frac{\hbar^2}{2m_p}\frac{\partial^2}{\partial z_p^2} + V_S(z_e) + V_S(z_p) + W(\varrho, z_e, z_p). \end{aligned} \tag{6.12}$$

In the rest of this chapter we adopt atomic units $\hbar = m_e = e = 1$, so that $1/\mu = 1/2$ and $M = 2$. By examining the form of (6.12), we can easily see that we can write the wavefunction of our problem as:

$$\Psi(\mathbf{r}_e, \mathbf{r}_p) = e^{ik_X X} e^{ik_Y Y} \Psi(\varrho, \theta, z_e, z_p). \tag{6.13}$$

We are, however, not interested in the kinetic energy due to the center of mass motion in the plane so we chose $k_X = k_Y = 0$. The observation that the center of mass behaves as a free particle can be used to introduce an additional simplification. Indeed, we can assume that the electron and positron are delocalized over the surface. This means that the electron density at each point above the surface is negligible and can be left out when calculating the exchange and correlation potential for this particle. In other words, we can calculate the exchange and correlation potential once from the electron density of the solid and keep it fixed when solving the two-particle problem. We have periodic boundary conditions for the angular part $\Psi(\varrho, \theta = 0, z_e, z_p) = \Psi(\varrho, \theta = 2\pi, z_e, z_p)$ since there is no dependence on this angle in the potential terms. We can thus write:

$$\Psi(\mathbf{r}_e, \mathbf{r}_p) = e^{il\theta}\Psi(\varrho, z_e, z_p). \tag{6.14}$$

After filling in this form of the wavefunction, we find that the Schrödinger equation we have to solve is given by:

$$\begin{aligned}\left\{-\frac{1}{4\varrho}\frac{\partial}{\partial\varrho}\left(\varrho\frac{\partial}{\partial\varrho}\right) + \frac{l^2}{4\rho^2} - \frac{1}{2}\frac{\partial^2}{\partial z_e^2} - \frac{1}{2}\frac{\partial^2}{\partial z_p^2}\right\}\Psi(\varrho, z_e, z_p) \\ + \left[V_S(z_e) + V_S(z_p) + W(\varrho, z_e, z_p)\right]\Psi(\varrho, z_e, z_p) = E\Psi(\varrho, z_e, z_p)\end{aligned} \tag{6.15}$$

We can set $l = 0$ since we expect that that state will correspond with the ground state. The extra potential terms in comparison with the hydrogen atom make this problem no further separable.
We could in principle attempt to solve the Schrödinger equation on a three dimensional grid but if we would select a coarse $100 \times 100 \times 100$ grid, we already end up with a square matrix of size 10^6. We can, however, reduce the problem to two two-dimensional problems by using the Hartree approach, which seems more feasible.

Second proposition: The Hartree approach. We consider again the Hamiltonian before introducing the center of mass coordinates and then use the Hartree approach, i.e. we write the wavefunction as a product of the electron and positron wavefunction:

$$\Psi(\mathbf{r}_e, \mathbf{r}_p) = \psi_e(\mathbf{r}_e)\psi_p(\mathbf{r}_p). \tag{6.16}$$

We can then apply the variational principle under the condition that the wavefunctions of both particles should remain normalized:

$$\delta\left(\langle\Psi|\hat{H}|\Psi\rangle - \varepsilon_e\left[\langle\psi_e|\psi_e\rangle - 1\right] - \varepsilon_p\left[\langle\psi_p|\psi_p\rangle - 1\right]\right) = 0. \tag{6.17}$$

Under variations of the electron wavefunction and the positron wavefunction, we can derive two one-particle equations:

$$\begin{aligned}\left[-\frac{\nabla_e^2}{2} + V_s(z_e) + V_{im,e}(z_e) + \int d\mathbf{r}_p\rho_p(\mathbf{r}_p)\left[V_C(\mathbf{r}_e, \mathbf{r}_p) + V_{ci}(\mathbf{r}_e, \mathbf{r}_p)\right]\right]\psi_e = \varepsilon_e\psi_e \\ \left[-\frac{\nabla_p^2}{2} + V_s(z_p) + V_{im,p}(z_p) + \int d\mathbf{r}_e\rho_e(\mathbf{r}_e)\left[V_C(\mathbf{r}_e, \mathbf{r}_p) + V_{ci}(\mathbf{r}_e, \mathbf{r}_p)\right]\right]\psi_p = \varepsilon_p\psi_p.\end{aligned} \tag{6.18}$$

It is now more convenient to chose the origin of coordinates arbitrarily in the plane. The Coulomb and cross-image potential then take on following form:

$$\begin{aligned} V_C(\mathbf{r}_e, \mathbf{r}_p) &= -\frac{e^2}{\sqrt{\varrho_e^2 + \varrho_p^2 - 2\varrho_e\varrho_p\cos(\theta_e - \theta_p) + (z_e - z_p)^2}} \\ V_{ci}(\mathbf{r}_e, \mathbf{r}_p) &= \frac{ee_i\left[\theta(z_e > z_1) + \theta(z_p > z_1)\right]}{2\sqrt{\varrho_e^2 + \varrho_p^2 - 2\varrho_e\varrho_p\cos(\theta_e - \theta_p) + (z_e + z_p - 2z_{im})^2}}. \end{aligned} \tag{6.19}$$

The electron and positron densities that turn up in the integrals are given by $\rho_{e,p} = |\psi_{e,p}(\mathbf{r}_{e,p})|^2$. Note that the problem of self-interaction that is normally present in the Hartree approach does not turn up here because we are dealing with two distinguishable particles. We present the details of the implementation of these integrals in appendix D.
We now describe how we can solve the one-particle equations and because both can be solved with exactly the same approach, we only go into detail for the electron equation. A first step is to make a guess for the positron wavefunction, which then delivers some potential for the electron. In practice we chose a wavefunction that is localized around the origin and intuitively, it is clear that such a choice traps the electron around the same point. In this way we immediately eliminate the center of mass motion in the plane of the surface. Furthermore, we know from the foregoing discussion that in the relative coordinates, the two-particle wavefunction has axial symmetry. We can only realize this symmetry if we assume that both one-particle wavefunctions also exhibit axial symmetry. We can thus write:

$$\psi(\mathbf{r}_e) = e^{il\theta_e}\psi(\varrho_e, z_e). \tag{6.20}$$

We can substitute this form for the wavefunction in the electron equation and in our search for the ground state of the system, we can put $l = 0$. The electron equation then takes on the form:

$$\begin{aligned} \Bigg[-\frac{1}{2\varrho_e}\frac{\partial}{\partial\varrho_e}\left(\varrho_e\frac{\partial}{\partial\varrho_e}\right) - \frac{1}{2}\frac{\partial^2}{\partial z_e^2} + V_s(z_e) + V_{im,e}(z_e) \\ + \int d\mathbf{r}_p\,\rho_p(\varrho_p, z_p)\left[V_C(\mathbf{r}_e, \mathbf{r}_p) + V_{ci}(\mathbf{r}_e, \mathbf{r}_p)\right]\Bigg]\psi_e(\varrho_e, z_e) = \varepsilon_e\psi_e(\varrho_e, z_e). \end{aligned} \tag{6.21}$$

We can solve this equation with a finite differences scheme, which is presented in appendix D. By iteratively solving the electron and positron equation, we expect the solutions to converge. The resulting positron wave function can then be used to calculate properties which are interesting for positron spectroscopy techniques.

Chapter 7

Conclusion

In this thesis, we studied Ps bound states near the surfaces of Bi_2Te_2Se and graphene from first principles. The study was motivated because the Ps bound states, if they exist, can be used in positron spectroscopy to very selectively only probe the surface properties of materials. From the overlap of the Ps wavefunction with surface, quantities measured by positron spectroscopy techniques can be calculated theoretically and this can help in the interpretation of the experimental results. Apart from the possibility of a bound state, we were interested in the effect that the edge states of topological insulators have on the bound state.

In our approach, we described Ps as a neutral particle bound to the surface by the Van der Waals interaction. For Bi_2Te_2Se we found that a bound state exists with a binding energy of $E = -150\,\text{meV}$ and we studied the influence of the edge states on the Ps bound state. The material-specific parameters that turn up in this description are the electron decay length at the surface, the work function of Ps in the material and the dielectric function of the material. The work function does not feel any effect of the edge states since it is purely a bulk property of the material. We studied the effect of the edge states on the electron decay length by excluding the spin-orbit interaction. We found that the small changes in the electron density were dominated by differences we cannot attribute to the presence of the edge states. These differences, however, have a negligible effect on the electron density decay length and thus on the Ps bound state. The effect on the dielectric response of the material was studied by considering slabs with 1 QL and 4 QLs. In the first case, the edge states lose their metallic character because of the overlap with the edge state at the opposite surface. We considered both thin films and a semi-infinite solid and in the first case, we found that the difference in electronic structure causes a difference in the binding energy of a few meV. For the semi-infinite solid we found that, by considering the surface instead of the bulk dielectric response, the effect is much larger and causes a difference in the binding energy of 22%. For suspended graphene we considered a symmetrical potential well and we found two bound states with a binding energy of $E = -383\,\text{meV}$ and $E = -133\,\text{meV}$. In a rough model for graphene on a substrate, we considered the same potential well for $z > 0$ but for $z < 0$, we took the value of the work function. In this case we found a bound state with a binding energy of $E = -253\,\text{meV}$.

In the last chapter, we presented ax new description of the Ps bound state.

In this description, we solve the Hartree-Fock equations for the electron and positron in an effective potential that describes the effect of the solid. The effective potential for the electron and positron are given by the Coulomb and exchange-correlation potential due to the electrons of the solid. Because the LDA and GGA approximations to the exchange-correlation energy functionals fail to describe the long-range interaction properly, we introduced the classical image potentials.

Appendix A

Van der Waals interaction

In this appendix, we derive the Van der Waals interaction between a neutral atom and a semi-infinite crystalline plane. Before we start with the derivation, we briefly recall the theory of linear response functions for the reader who is unfamiliar with the topic.

A.1 Linear response

We base this brief introduction on the book of Phillips [40]. Consider a Hamiltonian that we can write as:

$$\hat{H} = \hat{H}_0 + \hat{W}(t), \tag{A.1}$$

where $\hat{H}_0$ is the unperturbed Hamiltonian and $\hat{W}(t)$ is time-dependent perturbation. The time dependent expectation value of any observable quantity $\hat{O}(t)$ can be written as:

$$\langle O(t) \rangle = \mathrm{Tr}\left(\hat{\rho}(t)\hat{O}\right), \tag{A.2}$$

where we assume the normalization $\mathrm{Tr}\left(\hat{\rho}(t)\right) = 1$ and where $\hat{\rho}(t)$ denotes the time-evolution of the density matrix, which can be obtained from the Liouville equation:

$$\frac{\partial \hat{\rho}(t)}{\partial t} = -\frac{i}{\hbar}\left[\hat{H}, \hat{\rho}(t)\right] = -\frac{i}{\hbar}\left(\left[\hat{H}_0, \hat{\rho}(t)\right] + \left[W(t), \hat{\rho}(t)\right]\right). \tag{A.3}$$

This equation can formally be solved in the interaction picture, this means that operators have the form:

$$\hat{A}_I(t) = e^{i\hat{H}_0 t/\hbar}\hat{A}e^{-i\hat{H}_0 t/\hbar}. \tag{A.4}$$

If we evaluate the left hand side of the Liouville equation we find:

$$i\hbar\frac{\partial \hat{\rho}_I(t)}{\partial t} = -\hat{H}_0\hat{\rho}_I(t) + e^{i\hat{H}_0 t/\hbar}i\hbar\frac{\partial \rho(t)}{\partial t}e^{-i\hat{H}_0 t/\hbar} + e^{i\hat{H}_0 t/\hbar}\hat{\rho}(t)\hat{H}_0 e^{-i\hat{H}_0 t/\hbar}. \tag{A.5}$$

If we now use the fact that $\hat{H}_0$ commutes with the time evolution operator in the interaction picture and use the Liouville equation we had before to rewrite the second term, we arrive at:

$$\begin{aligned} i\hbar\frac{\partial\hat{\rho}_I(t)}{\partial t} &= -\left[\hat{H}_0,\hat{\rho}_I(t)\right] + e^{i\hat{H}_0 t/\hbar}\left[\hat{H}_0+\hat{W}_I(t),\hat{\rho}(t)\right]e^{-i\hat{H}_0 t/\hbar} \\ &= \left[\hat{W}_I(t),\hat{\rho}_I(t)\right], \end{aligned} \tag{A.6}$$

This equation can be solved as usual by integration both sides and then repeatedly substituting the solutions. The general solution is given by the time-ordered product:

$$\hat{\rho}_I(t) = \mathcal{T}\left\{\exp\left(\frac{1}{i\hbar}\int_{-\infty}^{t} dt'\left[\hat{W}_I(t'),\hat{\rho}_0\right]\right)\right\}, \tag{A.7}$$

where $\hat{\rho}_0 = \lim_{t\to-\infty}\hat{\rho}_I(t)$ denotes the density matrix of the unperturbed system. The first order approximation becomes:

$$\hat{\rho}_I(t) = \hat{\rho}_0 - \frac{i}{\hbar}\int_{-\infty}^{t} dt'\left[\hat{W}_I(t'),\hat{\rho}_0\right], \tag{A.8}$$

so that we can write for the expectation value of the observable:

$$\begin{aligned} \langle\hat{O}(t)\rangle &= \mathrm{Tr}\left(\hat{\rho}_I(t)\hat{O}_I(t)\right) \\ &= \langle\hat{O}_I(t)\rangle_0 - \frac{i}{\hbar}\int_{-\infty}^{t} dt'\,\mathrm{Tr}\left(\hat{O}_I(t)\left[\hat{W}_I(t'),\hat{\rho}_0\right]\right). \end{aligned} \tag{A.9}$$

Here $\langle\ldots\rangle_0$ denotes the expectation value w.r.t. the unperturbed system. The trace allows us to perform a cyclic permutation of the terms so that we obtain the result:

$$\langle O(t)\rangle = \langle\hat{O}_I(t)\rangle_0 - \frac{i}{\hbar}\int_{-\infty}^{t}\chi_{OW}(t,t')dt', \tag{A.10}$$

in which we defined the linear response function or susceptibility:

$$\chi_{OW}(t,t') = \left\langle\left[\hat{O}_I(t),\hat{W}(t')\right]\right\rangle_0. \tag{A.11}$$

If the response of the material only depends on the time difference, then we can introduce the frequency transform of the response function:

$$\chi_{OW}(w) = \int dt\, e^{i\omega t}\left\langle\left[\hat{O}_I(t),\hat{W}(0)\right]\right\rangle_0. \tag{A.12}$$

A.2 Van der Waals interaction between an atom and a surface

In this subsection we derive an expression for the Van der Waals interaction between a neutral atom and a semi-infinite surface. We give some more details in the derivation than in the paper of Zaremba and Kohn [57] and we point out what approximations we make.

In the Van der Waals interaction, we are interested in the attractive force between a neutral atom and a surface due to the instantaneous dipole. A schematic picture of the system is given in figure A.1. The first assumption that we make in the derivation is that the overlap between the wavefunction of the solid and the atom is negligible. In this way, the electrons of both subsystems can be regarded as distinguishable and the total Hamiltonian can be written as:

$$\hat{H} = \hat{H}_a + \hat{H}_s + \hat{V}_{as}, \tag{A.13}$$

where $\hat{H}_a$ and $\hat{H}_s$ are the Hamiltonians of the isolated atom and solid respectively. The interaction term $\hat{V}_{as}$ is the Hartree interaction between the two subsystems:

$$\hat{V}_{as} = \int d\mathbf{r} \int d\mathbf{r}' \frac{\hat{\rho}^s(\mathbf{r})\hat{\rho}^a(\mathbf{r}')}{|\mathbf{r} - \mathbf{r}'|}, \tag{A.14}$$

with the density operators defined as:

$$\hat{\rho}(\mathbf{r}) = n_+(\mathbf{r}) - \hat{n}(\mathbf{r}). \tag{A.15}$$

Here, $\hat{n}(\mathbf{r})$ is the electron density operator and since we will adopt the Born-Oppenheimer approximation, the charge density of the ions $n_+(\mathbf{r})$ is just a function. Note that we do not have to include the exchange interaction since we supposed that the overlap is zero. We suppose that the interaction between the two systems is weak so that we can calculate the interaction energy perturbatively.

The first order contribution is given by the expression:

$$E^{(1)} = \langle \Psi_0^a \Psi_0^s | \hat{V}_{as} | \Psi_0^a \Psi_0^s \rangle = \int d\mathbf{r} \rho_0^a(\mathbf{r}) \varphi_0^s(\mathbf{r}) \tag{A.16}$$

where $|\Psi_0^a \Psi_0^s\rangle$ is the product state constructed from the ground states of the isolated atom and surface, $\rho_0^a(\mathbf{r})$ is the corresponding ground state density of the atom and $\varphi_0^s(\mathbf{r})$ is the electrostatic potential of the surface. The latter exhibits periodicity in the plane parallel with the surface, which allows us to write it as:

$$\varphi_0^s(\mathbf{r}) = \sum_h e^{i\mathbf{Q}_h \cdot \boldsymbol{\varrho}} \varphi_0^s(z, \mathbf{Q}_h), \tag{A.17}$$

where the reciprocal vectors $\mathbf{Q}_h = (Q_{hx}, Q_{hy})$ are confined to lie in the plane of the surface. Let us consider $\varphi_0^s(z, \mathbf{Q}_h = 0)$ for a moment:

$$\varphi_0^s(z, 0) = \frac{1}{2\pi} \int_A dx dy \, \varphi_0^s(\mathbf{r}), \tag{A.18}$$

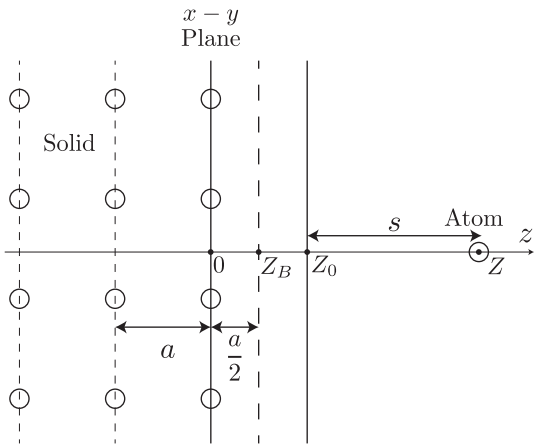

Figure A.1: A schematic picture of the atom-surface system with the coordinates that are used in the derivation.

which is thus the potential averaged over the surface of the solid. The electrical field can be calculated by taking the gradient of this potential and should thus also point in the z-direction. This electrical field, we can in turn determine from Gauss' law by drawing a rectangular box that encloses an area of the surface that corresponds with one unit cell. In the z-direction, we can draw our box such that it encloses all charge of the solid's surface but none of the atom, since we assume they are not overlapping. Because the solid is electrically neutral, there is no net electrical flux in the z-direction and in this case thus also no electrical field. We have to conclude that the term we considered, can only cause a constant shift of the energy, which we can always omit. For the $\mathbf{Q}_h \neq 0$ terms we can write:

$$\begin{aligned}\varphi_0^s(z,\mathbf{Q}_h) &= \int d\boldsymbol{\varrho} e^{-i\mathbf{Q}_h\cdot\boldsymbol{\varrho}} \int d\mathbf{r}' \frac{\rho^s(\mathbf{r}')}{|\mathbf{r}-\mathbf{r}'|} \\ &= \int d\boldsymbol{\varrho} \int d\mathbf{r}' \int \frac{d\mathbf{q}}{2\pi q} e^{i(\mathbf{q}-\mathbf{Q}_h)\cdot\boldsymbol{\varrho}} e^{-i\mathbf{q}\cdot\boldsymbol{\varrho}'} \rho^s(\mathbf{r}') e^{-q|z-z'|} \\ &= \int \frac{d\mathbf{r}'}{Q_h} \rho^s(\mathbf{r}') e^{i\mathbf{Q}_h\cdot\boldsymbol{\varrho}'} e^{-q|z-z'|},\end{aligned} \tag{A.19}$$

where we used the two-dimensional Fourier transform of the Coulomb potential (A.32). These terms decay exponentially away from the surface and thus do not contain the power law dependence we are looking for.

The second order perturbation is given by the usual expression:

$$\Delta E^{(2)} = \sum_{\alpha,\beta\neq 0} \frac{|\langle \Psi_0^a \Psi_0^s | V_{as} | \Psi_\alpha^a \Psi_\beta^s \rangle|^2}{(E_0^a - E_\alpha^a) + (E_0^s - E_\beta^s)}, \tag{A.20}$$

where the greek indices denote excited states. Now, since we made the assumption that there is no overlap between the wavefunctions of the atom and the solid, we can write the wavefunction of the atom-solid system as a product of

the two. If we want a non-zero contribution, we need some operator that is squeezed between the bra and the ket for both the solid and the atom. In other words, the only surviving term of the Coulomb interaction is the product of the electron density operators. We now try to rewrite this contribution towards a more useful form. In the first step we use the following identity:

$$\frac{1}{\tilde{\omega}_\alpha^a + \tilde{\omega}_\beta^s} = \frac{2}{\pi}\int_0^\infty du \frac{\tilde{\omega}_\alpha^a}{(\tilde{\omega}_\alpha^a)^2 + u^2}\frac{\tilde{\omega}_\beta^s}{(\tilde{\omega}_\beta^s)^2 + u^2}, \tag{A.21}$$

which can easily be checked by evaluating the right hand side by means of a complex contour integral and where we wrote $\tilde{\omega}_n = E_n - E_0$. After putting everything discussed so far together, we get:

$$\begin{aligned}\Delta E^{(2)} = &-\frac{2}{\pi}\int_0^\infty du \int d\mathbf{r}\int d\mathbf{r}'\int d\mathbf{x}\int d\mathbf{x}' \frac{1}{|\mathbf{x}-\mathbf{r}|}\frac{1}{|\mathbf{x}'-\mathbf{r}'|} \\ &\times \sum_{\alpha,\beta\neq 0} \frac{\tilde{\omega}_\alpha^a}{(\tilde{\omega}_\alpha^a)^2+u^2}\frac{\tilde{\omega}_\beta^s}{(\tilde{\omega}_\beta^s)^2+u^2}\langle\Psi_0^a|\hat{n}^a(\mathbf{x})|\Psi_\alpha^a\rangle\langle\Psi_\alpha^a|\hat{n}^a(\mathbf{x}')|\Psi_0^a\rangle \\ &\times \langle\Psi_0^s|\hat{n}^s(\mathbf{r})|\Psi_\beta^s\rangle\langle\Psi_\beta^s|\hat{n}^s(\mathbf{r}')|\Psi_0^s\rangle\end{aligned} \tag{A.22}$$

Let us focus on the sum over α with the relevant terms in the sum for a moment:

$$\begin{aligned}&\sum_{\alpha\neq 0}\frac{\tilde{\omega}_\alpha^a}{(\tilde{\omega}_\alpha^a)^2+u^2}\langle\Psi_0^a|\hat{n}^a(\mathbf{x})|\Psi_\alpha^a\rangle\langle\Psi_\alpha^a|\hat{n}^a(\mathbf{x}')|\Psi_0^a\rangle \\ &= \frac{1}{2}\lim_{\varepsilon\to 0}\sum_{\alpha\neq 0}\left[\frac{1}{iu+\tilde{\omega}_\alpha^a+i\varepsilon} - \frac{1}{iu-\tilde{\omega}_\alpha^a+i\varepsilon}\right]\langle\Psi_0^a|\hat{n}^a(\mathbf{x})|\Psi_\alpha^a\rangle\langle\Psi_\alpha^a|\hat{n}^a(\mathbf{x}')|\Psi_0^a\rangle.\end{aligned} \tag{A.23}$$

We used here that $\hat{n}^a(\mathbf{r})$ is a hermitian operator. The terms between brackets can be seen as the result of the integral:

$$\lim_{\varepsilon\to 0}\int_{-\infty}^\infty \frac{dy}{y+i\varepsilon}\left[\delta(iu+\tilde{\omega}_\alpha^a - y) - \delta(iu-\tilde{\omega}_\alpha^a - y)\right], \tag{A.24}$$

where the delta functions in turn can also be written in an integral form, so that the above expression becomes:

$$\lim_{\varepsilon\to 0}\frac{1}{2\pi}\int_{-\infty}^\infty dt\int_{-\infty}^\infty \frac{dy}{y+i\varepsilon}\left[e^{i(iu+\tilde{\omega}_\alpha^a - y)t} - e^{i(iu-\tilde{\omega}_\alpha^a - y)t}\right]. \tag{A.25}$$

If we now use the integral representation of the Heaviside step function:

$$-\frac{1}{2\pi i}\lim_{\varepsilon\to 0}\int_{-\infty}^\infty dy\frac{e^{-iyt}}{y+i\varepsilon} = \Theta(t) \tag{A.26}$$

in the previous result then we can rewrite the summation (A.23) as:

$$-\frac{i}{2}\sum_{\alpha\neq 0}\int_0^\infty dt\, e^{-ut}\left[e^{i\tilde{\omega}_\alpha^a t} - e^{-i\tilde{\omega}_\alpha^a t}\right]\langle\Psi_0^a|\hat{n}^a(\mathbf{x})|\Psi_\alpha^a\rangle\langle\Psi_\alpha^a|\hat{n}^a(\mathbf{x}')|\Psi_0^a\rangle. \tag{A.27}$$

Since the term between brackets can be written as $2i\sin(\tilde{\omega}_\alpha^a t)$, we can include the $\alpha = 0$ term in the summation because it will always give zero. We proceed by examining the term:

$$\begin{aligned}
&\sum_\alpha e^{i\tilde{\omega}_\alpha^a t}\langle\Psi_0|\hat{n}^a(\mathbf{x})|\Psi_\alpha^a\rangle\langle\Psi_\alpha^a|\hat{n}^a(\mathbf{x}')|\Psi_0^a\rangle \\
&= \sum_\alpha \langle\Psi_0|\hat{n}^a(\mathbf{x})|\Psi_\alpha^a\rangle\langle\Psi_\alpha^a|e^{i\hat{H}_0 t}\hat{n}^a(\mathbf{x}')e^{-i\hat{H}_0 t}|\Psi_0^a\rangle \\
&= \langle\Psi_0^a|\hat{n}^a(\mathbf{x},0)\hat{n}^a(\mathbf{x}',t)|\Psi_0^a\rangle.
\end{aligned} \tag{A.28}$$

Here the time dependence of the operators is like in the interaction picture. Together with the other term, equation (A.27) becomes:

$$\frac{i}{2}\int_0^\infty dt e^{-ut}\langle[\hat{n}^a(\mathbf{x},t),\hat{n}^a(\mathbf{x}',0)]\rangle_0 = \frac{1}{2}\chi_a(\mathbf{x},\mathbf{x}';iu), \tag{A.29}$$

where $\langle\dots\rangle_0$ denotes the ground state expectation value. When we look at the definition of the linear response function (A.12), then we see that $\chi_a(\mathbf{x},\mathbf{x}',iu)$ is nothing more than the frequency transform of the density-density response function evaluated at imaginary frequencies. We can make the exact same derivation for the sum over the excited states of the solid. The second order correction to the ground state energy then becomes:

$$\Delta E^{(2)} = -\int d\mathbf{r}\int d\mathbf{r}'\int d\mathbf{x}\int d\mathbf{x}'\frac{1}{|\mathbf{x}-\mathbf{r}|}\frac{1}{|\mathbf{x}'-\mathbf{r}'|}\int_0^\infty \frac{du}{2\pi}\chi_a(\mathbf{x},\mathbf{x}';iu)\chi_s(\mathbf{r},\mathbf{r}';iu). \tag{A.30}$$

This expression is still not very useful for a practical calculation and to work further, we need to introduce the two-dimensional Fourier transform of the Coulomb potential:

$$\frac{1}{|\mathbf{r}-\mathbf{x}|} = \frac{1}{8\pi^3}\int d\mathbf{q}_{\boldsymbol{\rho}}\int_{-\infty}^\infty dq_z \frac{4\pi}{q_{\boldsymbol{\rho}}^2+q_z^2}e^{i\mathbf{q}_{\boldsymbol{\rho}}\cdot(\rho_r-\rho_x)}e^{iq_z(z_r-z_x)}, \tag{A.31}$$

where $\mathbf{r} = (\boldsymbol{\rho}_r, z_r)$, $\mathbf{x} = (\boldsymbol{\rho}_x, z_x)$ and $\mathbf{q}_{\boldsymbol{\rho}} = (q_x, q_y, 0)$. The integral over q_z can be worked out with a contour integral, which makes a half circle in the upper half of the complex plane for $z_r - z_x > 0$ and in the lower half for $z_r - z_x < 0$. After obtaining this result we transition to a discrete Fourier transform by substituting $\frac{1}{4\pi^2}\int d\mathbf{q}_{\boldsymbol{\rho}} \to \frac{1}{L^2}\sum_{\mathbf{q}_{\boldsymbol{\rho}}}$, where L^2 is the surface area of the solid. The result is given by:

$$\frac{1}{|\mathbf{r}-\mathbf{x}|} = \frac{1}{L^2}\sum_{\mathbf{q}}\left(\frac{2\pi}{q}\right)e^{i\mathbf{q}\cdot(\boldsymbol{\rho}_r-\boldsymbol{\rho}_x)}e^{-q|z_r-z_x|}, \tag{A.32}$$

Note that we dropped the index $\boldsymbol{\rho}$ on the wave vectors. Before we introduce this Fourier transform in expression (A.30), we first replace the coordinates for the electron density of the atom $\mathbf{x} \to \mathbf{R} + \mathbf{x}$, where $\mathbf{R}$ denotes the position

of the nucleus, since this will be useful later on. The product of the Coulomb potentials can then be written as:

$$\begin{aligned}
&\frac{1}{|\mathbf{x}+\mathbf{R}-\mathbf{r}|}\frac{1}{|\mathbf{r}'-\mathbf{R}'-\mathbf{x}'|} \\
&= \frac{1}{L^4}\sum_{\mathbf{q},\mathbf{q}'} e^{-Z(q+q')} e^{i\mathbf{R}\cdot(\mathbf{q}-\mathbf{q}')} e^{i\mathbf{q}\cdot(\boldsymbol{\rho}_x-\boldsymbol{\rho}_r)} e^{i\mathbf{q}'\cdot(\boldsymbol{\rho}_{r'}-\boldsymbol{\rho}_{x'})} e^{-q(z_x-z_r)} e^{-q'(z_{x'}-z_{r'})} \\
&= \frac{1}{L^4}\sum_{\mathbf{q},\mathbf{q}'} e^{-Z(q+q')} e^{i\mathbf{R}\cdot(\mathbf{q}-\mathbf{q}')} e^{i\boldsymbol{\kappa}\cdot\mathbf{x}} e^{-i\boldsymbol{\kappa}^*\cdot\mathbf{x}'} e^{-i\boldsymbol{\kappa}\cdot\mathbf{r}} e^{i\boldsymbol{\kappa}^*\cdot\mathbf{r}'},
\end{aligned} \tag{A.33}$$

where in the last step we defined the complex wave vector $\boldsymbol{\kappa} = \mathbf{q} + iq\mathbf{e}_z$. Note that we dropped the absolute value in the exponent $|z_x+Z-z_r| \to (z_x+Z-z_r)$. This corresponds with neglecting the Coulomb potential felt by the electron cloud of the atom in a point $z_x + Z$ due to the electron density of the solid at the position $z_r > z_x + Z$. Since we already assumed that there is no overlap, this is no additional approximation. We assume that the surface is periodic, thus the Coulomb potential of the surface can be expanded as a Fourier series over the reciprocal lattice vectors $\mathbf{Q}_h$, i.e. we can restrict the sum over $\mathbf{q}'$ to $\mathbf{q}' = \mathbf{q} + \mathbf{Q}_h$. As a consequence, we find that :

$$e^{-ZQ_h/\sqrt{2}} \geq e^{-Z(\mathbf{q}+\mathbf{q}')}. \tag{A.34}$$

That is, we find that the $\mathbf{Q}_h \neq 0$ terms decay exponentially away from the surface. In our search for a power law dependence, we can thus retain only the $\mathbf{Q}_h = 0$ term for which $\mathbf{q} = \mathbf{q}'$. The energy correction becomes:

$$\begin{aligned}
\Delta E^{(2)} = -\int_0^\infty \frac{du}{2\pi}\frac{1}{L^4}\sum_{\mathbf{q}} \frac{4\pi^2}{q^2} e^{-2qZ} \int d\mathbf{x}\int d\mathbf{x}' e^{i\boldsymbol{\kappa}\cdot\mathbf{x}} e^{-i\boldsymbol{\kappa}^*\cdot\mathbf{x}'} \chi_a(\mathbf{x},\mathbf{x}';iu) \\
\times \int d\mathbf{r}\int d\mathbf{r}' e^{-i\boldsymbol{\kappa}\cdot\mathbf{r}} e^{i\boldsymbol{\kappa}^*\cdot\mathbf{r}'} \chi_s(\mathbf{r},\mathbf{r}';iu)
\end{aligned} \tag{A.35}$$

We see that the contribution to the energy correction falls off exponentially fast with increasing q, so if we assume that the atom is far away from the surface, i.e. Z is large, we can make a Taylor expansion around $q = 0$ in the atomic contribution. Before we make this expansion we first show:

$$\begin{aligned}
&\int d\mathbf{x}\, \chi_a(\mathbf{x},\mathbf{x}';iu) \\
&= i\int_0^\infty dt e^{-ut}\int d\mathbf{x}\langle[\hat{n}^a(\mathbf{x},t),\hat{n}^a(\mathbf{x}',t)]\rangle_0 \\
&= i\int_0^\infty dt e^{-ut}\int d\mathbf{x}(\rho_0^a(\mathbf{x},t)-\rho_0^a(\mathbf{x},t))\langle\Psi_0^a|\hat{n}^a(\mathbf{x}',0)-\hat{n}^a(\mathbf{x}',0)|\Psi_0^a\rangle = 0,
\end{aligned} \tag{A.36}$$

where the last step follows from the fact that the atom is neutral. This means that in the expansion, the first terms to survive are those which contain a product of x_i and x_i'. To work this out explicitly, we adopt spherical coordinates and

choose the z-axis along the vector $\boldsymbol{\kappa}$. Now, an atom in its ground state always exhibits spherical symmetry, which means that we can expand the response function in its spherical components as:

$$\chi_a(\mathbf{x},\mathbf{x}';iu) = \sum_{l,m} \chi_l(x,x';iu) Y_l^m(\hat{\mathbf{x}}) Y_l^{m*}(\hat{\mathbf{x}}'), \tag{A.37}$$

where Y_l^m are the spherical harmonics. We should keep in mind that the same reasoning does in general not hold if we consider a molecule instead of an atom. The exponentials in the integrals can be expanded as:

$$\begin{aligned} e^{i\boldsymbol{\kappa}\cdot\mathbf{x}} e^{-i\boldsymbol{\kappa}^*\cdot\mathbf{x}'} &= e^{i\kappa x\cos(\theta)} e^{-i\kappa^* x'\cos(\theta')} \\ &\approx 1 + i\kappa x\cos(\theta) - i\kappa^* x'\cos(\theta') + \kappa\kappa^* x x'\cos(\theta)\cos(\theta') \end{aligned} \tag{A.38}$$

The first three terms drop, as we just showed, because of the charge neutrality of the atom. If we only retain only the latter term, insert the expansion in spherical harmonics and write out the spherical harmonics explicitly, we find:

$$\begin{aligned} &\int d\mathbf{x} \int d\mathbf{x}' e^{i\boldsymbol{\kappa}\cdot\mathbf{x}} e^{-i\boldsymbol{\kappa}^*\cdot\mathbf{x}'} \chi_a(\mathbf{x},\mathbf{x}';iu) \\ &= \sum_{l,m} (-1)^{2m} \left(\frac{2l+1}{4\pi} \frac{(l-m)!}{(l+m)!} \right) \int_0^\infty dx\, x^3 \int_0^\infty dx'\, x'^3 \int_0^{2\pi} d\varphi\, e^{im\varphi} \int_0^{2\pi} d\varphi'\, e^{im\varphi'} \\ &\quad \times \kappa\kappa^* \int_0^\pi d\theta \sin(\theta)\cos(\theta) P_l^m(\cos(\theta)) \int_0^\pi d\theta' \sin(\theta')\cos(\theta') P_l^m(\cos(\theta')), \end{aligned} \tag{A.39}$$

where P_l^m are the associated Legrendre polynomials. The integral over φ yield zero except if $m = 0$ and in this case the associated Legendre polynomials reduce to the Legendre polynomials. We work out the integral over θ, where we make the substitution $y = \cos(\theta)$:

$$\int_0^\pi d\theta \sin(\theta)\cos(\theta) P_l(\cos(\theta)) = \int_{-1}^1 dy\, y P_l(y) = \frac{2}{3}, \tag{A.40}$$

where the last results follows since the Legendre polynomials form a family of orthogonal polynomials and $P_1(y) = y$, so we only have to consider the term $l = 1$. Everything together we find:

$$\begin{aligned} \int d\mathbf{x} \int d\mathbf{x}' e^{i\boldsymbol{\kappa}\cdot\mathbf{x}} e^{-i\boldsymbol{\kappa}^*\cdot\mathbf{x}'} \chi_a(\mathbf{x},\mathbf{x}';iu) &= \frac{4\pi}{3}\kappa\kappa^* \int_0^\infty dx\, x^3 \int_0^\infty dx'\, x'^3 \chi_1(x,x';iu) \\ &= 2q^2\alpha(iu). \end{aligned} \tag{A.41}$$

Here, $\alpha(iu)$ is the dynamic atomic dipole polarizability which can be defined as [6]:

$$\alpha(iu) = \frac{4\pi}{3} \int_0^\infty dx\, x^3 \int_0^\infty dx'\, x'^3 \chi_1(x,x';iu). \tag{A.42}$$

A more general result, that we will not rederive here, can be obtained by carrying on the expansion in powers of q. The result is given by:

$$\int d\mathbf{x} \int d\mathbf{x}' e^{i\boldsymbol{\kappa}\cdot\mathbf{x}} e^{-i\boldsymbol{\kappa}^*\cdot\mathbf{x}'} \chi_a(\mathbf{x},\mathbf{x}';iu) = \sum_{l=1}^{\infty} \frac{2^l \alpha_l(iu)}{l!(2l-1)!!} q^{2l} \tag{A.43}$$

where α_l is the multipole polarizability:

$$\alpha_l(iu) = \frac{4\pi}{2l+1} \int_0^\infty dx\, x^{l+2} \int_0^\infty dx' x'^{l+2} \chi_l(x,x';iu). \tag{A.44}$$

It is interesting to notice that only even power of q enter in this result. So that, since we consider only small q, we should get reasonable results by examining only the dipole polarizability. We then arrive at the result for the attractive interaction given in Zaremba's paper:

$$E^{(2)} = -\frac{2}{\pi} \int_0^\infty du\, \alpha(iu) F(Z;iu) \tag{A.45}$$

with:

$$F(Z;iu) = \frac{2\pi^2}{L^2} \sum_{\mathbf{q}} e^{-2qZ} \int dz \int dz' e^{q(z+z')} \chi_s(z,z',\mathbf{q},\mathbf{q}';iu), \tag{A.46}$$

and the two dimensional Fourier-transform of the response function:

$$\chi_s(z,z',\mathbf{q},\mathbf{q}';iu) = \frac{1}{L^2} \int d\boldsymbol{\rho} \int d\boldsymbol{\rho}' e^{-i\mathbf{q}\cdot\boldsymbol{\rho}} e^{i\mathbf{q}\cdot\boldsymbol{\rho}'} \chi_s(\mathbf{r},\mathbf{r}';iu). \tag{A.47}$$

If we knew an expression for the atomic dipole polarizability and the solids density-density response function, we could attempt to evaluate the above expressions immediately. In most cases, however, we do not have an expression for the latter so we will work towards a more useful expressions. The first thing we note is that we only need to determine the long wavelength (small q) behavior of:

$$f(q;iu) = \int dz \int dz' e^{q(z+z')} \chi_s(z,z',\mathbf{q},\mathbf{q}';iu) \tag{A.48}$$

because of the exponential $\exp(-2qZ)$ in (A.46). Let us get some more insight in the meaning of the surface response function $F(Z;iu)$. Consider an external charge distribution located at $z = Z$:

$$\rho_{ext}(\mathbf{r},t) = \delta(z-Z) e^{i\mathbf{q}\cdot\boldsymbol{\rho}} e^{ut}. \tag{A.49}$$

The electrostatic potential in the frequency domain due to this charge, for the region of interest $z < Z$, is given by:

$$\phi_{ext}(\mathbf{r},iu) = \int d\mathbf{r}' \frac{\rho_{ext}(\mathbf{r}',iu)}{|\mathbf{r}-\mathbf{r}'|} = \frac{2\pi}{q} e^{i\mathbf{q}\cdot\boldsymbol{\rho}} e^{-qZ} e^{qz}, \tag{A.50}$$

where we used the two dimensional Fourier transform (A.32). The response of the solid to this external potential is given by:

$$\begin{aligned}\delta n_S(\mathbf{r}, iu) &= \int d\mathbf{r}' \chi_S(\mathbf{r}, \mathbf{r}'; iu)\phi_{ext}(\mathbf{r}'; iu) \\ &= \int d\mathbf{r}' \sum_{\mathbf{q},h} e^{i(\mathbf{Q}_h+\mathbf{q})} e^{-i\mathbf{q}\cdot\boldsymbol{\rho}'} \chi_S(z, z', \mathbf{q}+\mathbf{Q}_h, \mathbf{q}; iu) \frac{2\pi}{q'} e^{-q'Z} e^{q'z'} e^{i\mathbf{q}'\cdot\boldsymbol{\rho}'} \\ &= \frac{2\pi}{q} e^{-qZ} e^{i\mathbf{q}\cdot\boldsymbol{\rho}} \sum_h e^{i\mathbf{Q}_h\cdot\boldsymbol{\rho}} \int dz' \chi_S(z, z', \mathbf{q}+\mathbf{Q}_h, \mathbf{q}; iu) e^{qz} \\ &= \frac{2\pi}{q} e^{-qZ} e^{i\mathbf{q}\cdot\boldsymbol{\rho}} \delta\tilde{n}_{\mathbf{Q}_h}(z, \mathbf{q}; iu)\end{aligned} \tag{A.51}$$

where in the second step we used the inverse Fourier transform of (A.47). In the last line the first three terms are identical to the component of the external potential parallel to the surface of the solid. The z-dependence of the induced charge in described $\delta\tilde{n}_{\mathbf{Q}_h}(z, \mathbf{q}; iu)$. The average over the surface of this last term is obtained by setting $\mathbf{Q}_h = 0$ and is given by:

$$\delta\tilde{n}_0(z, \mathbf{q}; iu) = \int dz' \chi_S(z, z', \mathbf{q}, \mathbf{q}; iu) e^{qz}. \tag{A.52}$$

In this way, we can write the surface response function as:

$$F(Z; iu) = \frac{2\pi^2}{L^2} \sum_{\mathbf{q}} e^{-2qZ} \frac{q}{2\pi} \int dz\, e^{qz}\, \delta\tilde{n}_0(z, q; iu) = \frac{2\pi^2}{L^2} \sum_{\mathbf{q}} e^{-2qZ} f(q; iu). \tag{A.53}$$

Physically this means that if the atom is far away from the surface, the induced charge fluctuations in the solid due to the instantaneous dipole of the atom are spread out across the surface. Zaremba and Kohn point out in their paper that $\delta\tilde{n}_0(z, q; iu)$ oscillates around a zero mean in the high frequency limit. A consequence is that an immediate expansion of this quantity in powers of q is not possible. Instead, they eliminated the periodic part by taking the average:

$$\delta\bar{n}(z, q; iu) = \frac{1}{a} \int_{z-a/2}^{z+a/2} dz' \delta\tilde{n}_0(z', q' iu) \tag{A.54}$$

Furthermore, we note that for the small q behavior of $f(q; iu)$ in (A.53), $\delta\tilde{n}_0(z, q; iu)$ and $\delta\bar{n}_0(z, q; iu)$ are interchangeable:

$$\begin{aligned}&\int dz\, e^{qz} \delta\bar{n}_0(z, q; iu) = \frac{1}{a} \int dz \int_{z-a/2}^{z+a/2} dz'\, e^{qz} \delta\tilde{n}_0(z', q; iu) \\ &= \frac{1}{a} \int dz'\, \delta\tilde{n}_0(z', q; iu) \int_{z'-a/2}^{z'+a/2} dz\, e^{qz} = \int dz'\, e^{qz'} \delta\tilde{n}_0(z', q; iu) + O(q^2).\end{aligned} \tag{A.55}$$

If we make this replacement in $f(q;iu)$ and introduce the following expansion:

$$\delta\bar{n}(z,q;iu) = \delta\bar{n}_0(z;iu) + q\delta\bar{n}_1(z;iu) + O(q^2), \tag{A.56}$$

then we find:

$$\begin{aligned} f(q;iu) &= \frac{q}{2\pi}\int dz\left\{\delta\bar{n}_0(z;iu) + q\left[z\delta\bar{n}_0(z;iu) + \delta\bar{n}_1(z;iu)\right] + O(q^2)\right\} \\ &= \frac{q}{2\pi}\int dz\,\delta\bar{n}_0(z;iu)\left[1 + 2q\bar{z}(iu) + O(q^2)\right], \end{aligned} \tag{A.57}$$

where:

$$\bar{z}(iu) = \frac{\int dz\, z\,\delta\bar{n}_0(z;iu)}{\int dz\,\delta\bar{n}_0(z;iu)} + \frac{1}{2}\frac{\int dz\left[\delta\bar{n}_1(z;iu) - z\,\delta\bar{n}_0(z;iu)\right]}{\int dz\,\delta\bar{n}_0(z;iu)}. \tag{A.58}$$

In the above expressions, $\int dz\,\delta\bar{n}_0(z;iu)$ represents the total surface screening charge induced by the external potential. The first term of $\bar{z}(iu)$ is then the centroid of this induced charge and we can expect that it is highly localized near the surface of the solid, The second term has no simple physical interpretation and Zaremba and Kohn showed that this term disappears in the zero and high frequency limit but it is not guaranteed to vanish for intermediate frequencies. If we want to evaluate the formal expression we obtained so far, we need to determine $\delta\bar{n}_0(z;iu)$ and we do this by considering the continuity equation:

$$\frac{\partial}{\partial t}n(\mathbf{r},t) + \nabla\cdot\mathbf{j}(\mathbf{r},t) = 0. \tag{A.59}$$

We know that the induced charge should have the same time-dependence as the external charge (A.49) and we can also assume the same form for the current density. Since we want to know $\delta\bar{n}_0(z;iu)$, we average over the surface and afterwards apply the same averaging as in (A.54). This allows us to rewrite the continuity equation to:

$$u\,\delta\bar{n}_0(z;iu) + \frac{\partial}{\partial z}\bar{j}_z(z;iu) = 0 \tag{A.60}$$

If we formally integrate this equation we get:

$$\bar{j}_z(-\infty;iu) = u\int_{-\infty}^{\infty} dz\,\delta\bar{n}_0(z;iu) \tag{A.61}$$

This current density deep inside the solid, we can also obtain by using Ohm's law. The electrical field $\mathbf{E} = -e^{ut}E_0\,\mathbf{e}_z$ is determined by the external charge (A.49) screened by the induced surface charge. By integrating Gauss' law, we obtain:

$$E_0 = 2\pi\left(1 - \int_{-\infty}^{\infty} dz\,\delta\bar{n}_0(z;iu)\right) \tag{A.62}$$

The current density is then given by:

$$\bar{j}_z(-\infty;iu) = \sigma(iu)E_0. \tag{A.63}$$

If we combine the last three results, we get:

$$\int_{-\infty}^{\infty} dz\, \delta\bar{n}_0(z;iu) = \frac{2\pi\sigma(iu)/u}{1+2\pi\sigma(iu)/u} = \frac{\epsilon(iu)-1}{\epsilon(iu)+1}, \tag{A.64}$$

where we used the relation between the conductivity and the dielectric function $\epsilon(iu) = 1 + 4\pi\sigma(iu)/u$. If we substitute this result in (A.57), we find:

$$f(q;iu) = \frac{q}{2\pi}\left[1 + 2q\bar{z}(iu) + O(q^2)\right]\left(\frac{\epsilon(iu)-1}{\epsilon(iu)+1}\right) \tag{A.65}$$

This form allows for an evaluation of the surface response function (A.53), where we transition from the discrete sum to an integral:

$$\begin{aligned} F(Z;iu) &= \frac{1}{2}\left(\frac{\epsilon(iu)-1}{\epsilon(iu)+1}\right)\int_0^{\infty} dq\, q^2\left[1 + 2q\bar{z}(iu) + O(q^2)\right]e^{-2qZ} \\ &= \frac{1}{2}\left(\frac{\epsilon(iu)-1}{\epsilon(iu)+1}\right)\left[\frac{1}{4Z^3} + \frac{3}{4Z^4} + O(Z^{-5})\right] \end{aligned} \tag{A.66}$$

So at long last we find the Van der Waals attraction:

$$E^{(2)} = -\frac{C}{Z^3}\left[1 + 3\frac{Z_0}{Z} + O(Z^{-2})\right], \tag{A.67}$$

where we introduced the Van der Waals constant:

$$C = \frac{1}{4\pi}\int_0^{\infty} du\alpha(iu)\left(\frac{\epsilon(iu)-1}{\epsilon(iu)+1}\right) \tag{A.68}$$

and the Van der Waals reference plane:

$$Z_0 = \frac{1}{4\pi C}\int_0^{\infty} du\alpha(iu)\left(\frac{\epsilon(iu)-1}{\epsilon(iu)+1}\right)\bar{z}(iu). \tag{A.69}$$

The expression for the Van der Waals attraction (A.67) can be rewritten to a more convenient form by measuring distances w.r.t. the Van der Waals reference plane $Z \to Z - Z_0$. The result of $F(Z - Z_0; iu)$ is then given by:

$$E^{(2)} = -\frac{C}{(Z-Z_0)^3} + O(Z^{-5}). \tag{A.70}$$

Appendix B

Further information about the LAPW method

B.1 Choice of sphere radii

Let us discuss the importance of keeping the plane wave cutoff low. When setting up the secular equation, its size is determined by the amount of plane waves, which scales as the cube of the the plane wave cutoff. The time required to solve the secular equation in turn scales as the cube of its size, so in the end we find that the required calculation time scales as the ninth power of the plane wave cutoff. It is thus imperative for any practical calculation to keep it as low as possible. An important parameter that influences the cutoff is the size of the spheres around the nuclei. Indeed, they should be chosen in such a way that they minimize the computation time and *not* based on their physical 'size'.

To illustrate this, consider the case of NiAl, where the radii in their chemical sense are given by $R_{\mathrm{Al}} = 2.8\,\mathrm{bohr}$ and $R_{\mathrm{Ni}} = 1.9\,\mathrm{bohr}$. Now since the plane waves are extended throughout the interstitial region, one should pick the highest cutoff needed for the different elements in the material. Well converged plane wave cutoffs are given by $R_{\mathrm{Al}}G_{\mathrm{max}} = 6$ and $R_{\mathrm{Ni}}G_{\mathrm{max}} = 9$. With the choice of radii in the chemical sense we find that the cutoff is determined by Ni and is equal to $G_{\mathrm{max}} = 4.74$. If we would, however, swap the radii and choose $R_{\mathrm{Al}} = 1.9$ and $R_{\mathrm{Ni}} = 2.8$, the maximal cutoff is determined again by Ni but is this time equal to $G_{\mathrm{max}} = 3.21$. The difference in computation time between these two choices is a factor $(4.74/3.21)^9 = 33$.

B.2 Core electrons and valence electrons

The LAPW method is an all electron approach although this does not mean that no distinction is made between core electrons and valence electrons. Indeed, for core electrons it is imperative to solve the Dirac equation since spin-orbit and other relativistic corrections are very important, certainly for heavier elements, while for valence electrons this effect can often be treated as a perturbation, if necessary. On the other hand one can assume that core electrons have spherical

symmetric wavefunctions and stay confined inside the spheres, such that it is unnecessary to expand them in the LAPW basis, i.e. a numerical basis of spherical solutions to the Dirac equation inside the spheres suffices. It is worth pointing out that the last approximation means that no plane waves are necessary for the core electrons and that, since the core states are considered to vanish on the sphere boundary, valence states are automatically orthogonal to them, as pointed out earlier. Herein lies an important distinction with pseudopotential codes: The true ground state electron density is sought in a LAPW calculation. This means that the electron density is in principle correct over the whole crystal instead of only in the interstitial part as with pseudopotential codes.
So, concretely: Core electron states are calculated self-consistently and fully relativistically in the crystal potential. They are however approximated to be confined in the spheres, that is, their wavefunction is considered to be zero outside the spheres, and to be spherical, which means that the potential in the Dirac equation is replaced by its spherical part. Valence electron states are calculated self-consistently in the crystal potential with the Schrödinger equation (unless relativistic corrections are also important for valence electrons, see the next paragraph).

B.3 Relativistic corrections.

Before we take a look at how relativistic corrections can be taken into account, we find it instructive to first derive the radial Dirac equation, as it is something most physicists at the master degree are not familiar with. The material presented here is based on the book of P. Strange [49].

The time-independent Dirac equation for a spherical potential $V(\mathbf{r}) = V(r)$ is given by:

$$(c\boldsymbol{\alpha} \cdot \hat{\mathbf{p}} + \beta mc^2 + V(r))\psi = W\psi, \tag{B.1}$$

where β and the components of $\boldsymbol{\alpha}$ are given by:

$$\beta = \begin{pmatrix} I_2 & 0 \\ 0 & I_2 \end{pmatrix} \quad \alpha_x = \begin{pmatrix} 0 & \sigma_x \\ \sigma_x & 0 \end{pmatrix} \quad \alpha_y = \begin{pmatrix} 0 & \sigma_y \\ \sigma_y & 0 \end{pmatrix} \quad \alpha_z = \begin{pmatrix} 0 & \sigma_z \\ \sigma_z & 0 \end{pmatrix}, \tag{B.2}$$

in which the σ_i are the Pauli matrices. We now rewrite the kinetic term of the Dirac equation and for this we start with following vector identity:

$$\mathbf{A} \times (\mathbf{B} \times \mathbf{C}) = \mathbf{B}(\mathbf{A} \cdot \mathbf{C}) - \mathbf{C}(\mathbf{A} \cdot \mathbf{B}), \tag{B.3}$$

with $\mathbf{A} = \mathbf{B} = \hat{\mathbf{r}}$, the unit radial vector, and $\mathbf{C} = \nabla$ we find that:

$$\nabla = \hat{\mathbf{r}}(\hat{\mathbf{r}} \cdot \nabla) - \hat{\mathbf{r}} \times (\hat{\mathbf{r}} \times \nabla). \tag{B.4}$$

Since we are dealing with a spherical potential, the wavefunction should also be spherical, thus $\partial/\partial\theta$ and $\partial/\partial\phi$ disappear. For the second term we use the angular momentum operator $\hat{\mathbf{L}} = \hat{\mathbf{x}} \times \hat{\mathbf{p}} = -i\hbar\mathbf{r} \times \nabla$. Here $\hat{\mathbf{x}}$ is the position

operator, and $\mathbf{r}$ is the positional vector of the electron. We can then rewrite the above equation as:

$$\nabla = \hat{\mathbf{r}}\frac{\partial}{\partial r} - \frac{i}{\hbar}\frac{\hat{\mathbf{r}}}{|\mathbf{r}|} \times \hat{\mathbf{L}}, \tag{B.5}$$

so that the kinetic operator becomes:

$$\boldsymbol{\alpha} \cdot \hat{\mathbf{p}} = -i\hbar\boldsymbol{\alpha} \cdot \nabla = -i\hbar\boldsymbol{\alpha} \cdot \hat{\mathbf{r}}\frac{\partial}{\partial r} - \frac{1}{|\mathbf{r}|}\boldsymbol{\alpha} \cdot \hat{\mathbf{r}} \times \hat{\mathbf{L}}. \tag{B.6}$$

We still wish to rewrite this further and for that we use the following vector identity:

$$\boldsymbol{\alpha} \cdot \mathbf{A}\boldsymbol{\alpha} \cdot \mathbf{B} = \mathbf{A} \cdot \mathbf{B} + i\boldsymbol{\sigma} \cdot \mathbf{A} \times \mathbf{B}, \tag{B.7}$$

in which $\mathbf{A}$ and $\mathbf{B}$ are arbitrary vectors and:

$$\boldsymbol{\sigma}_i = \begin{pmatrix} \sigma_i & 0 \\ 0 & \sigma_i \end{pmatrix}. \tag{B.8}$$

Now since $\mathbf{r}$ and $\hat{\mathbf{L}}$ are perpendicular to each other this gives:

$$\boldsymbol{\alpha} \cdot \hat{\mathbf{r}}\boldsymbol{\alpha} \cdot \hat{\mathbf{L}} = i\boldsymbol{\sigma} \cdot \hat{\mathbf{r}} \times \hat{\mathbf{L}}. \tag{B.9}$$

Next we will use the γ_5 matrix which is defined as:

$$\gamma_5 = \begin{pmatrix} 0 & -I_2 \\ -I_2 & 0 \end{pmatrix} \tag{B.10}$$

and has the property that:

$$\gamma_5\boldsymbol{\alpha} = -\boldsymbol{\sigma} \qquad \gamma_5\boldsymbol{\sigma} = -\boldsymbol{\alpha}, \tag{B.11}$$

so that (B.9) becomes, after post multiplying with γ_5:

$$i\boldsymbol{\alpha} \cdot \hat{\mathbf{r}}\boldsymbol{\sigma} \cdot \hat{\mathbf{L}} = -\boldsymbol{\alpha} \cdot \hat{\mathbf{r}} \times \hat{\mathbf{L}}. \tag{B.12}$$

The kinetic operator now becomes:

$$\boldsymbol{\alpha} \cdot \hat{\mathbf{p}} = -i\hbar\boldsymbol{\alpha} \cdot \hat{\mathbf{r}}\frac{\partial}{\partial r} + \frac{i}{|\mathbf{r}|}\boldsymbol{\alpha} \cdot \hat{\mathbf{r}}\boldsymbol{\sigma} \cdot \hat{\mathbf{L}}. \tag{B.13}$$

Apart from the usual orbital angular momentum operator $\hat{\mathbf{L}}$, the spin angular momentum operator $\hat{\mathbf{S}}$ and the total angular momentum operator $\hat{\mathbf{J}}$, in relativistic quantum mechanics there is another interesting operator $\hat{K}$, which is also related to angular momentum. It is defined as:

$$\hat{K} = \beta(\boldsymbol{\sigma} \cdot \hat{\mathbf{L}} + \hbar). \tag{B.14}$$

Notice that because of its form, it is clear that it has to do with spin-orbit coupling. The operator is related to the total angular momentum as:

$$\hat{K}^2 = \hat{\mathbf{J}}^2 + \frac{\hbar^2}{4} \tag{B.15}$$

and it has eigenvalues:

$$\hat{K}\psi = \pm\left(j+\frac{1}{2}\right)\hbar\psi = -\kappa\hbar\psi, \tag{B.16}$$

what can easily be verified by using relation (B.15). We use $\kappa \in \mathbb{Z}_0$ as a quantum number to label the solutions to the radial equation further on and refer to it as the relativistic quantum number. Since we are dealing with spin 1/2 particles, it can be shown that κ has following relations with the non-relativistic quantum numbers j and l:

$$\begin{aligned} \kappa = -l-1 = -(j+1/2) \quad \text{if} \quad j = l+1/2 \\ \kappa = l = (j+1/2) \quad \text{if} \quad j = l-1/2. \end{aligned} \tag{B.17}$$

It is also interesting to mention that the following commutators hold:

$$[J_i, \hat{H}] = [\hat{\mathbf{J}}^2, \hat{H}] = [\hat{K}, \hat{H}] = [\hat{K}, \hat{\mathbf{J}}^2] = [\hat{K}, \hat{J}_z] = 0. \tag{B.18}$$

This means that $\hat{\mathbf{J}}^2, \hat{J}_z$ and $\hat{K}$ represent quantities that are constants of motion in relativistic quantum mechanics and that eigenfunctions of the relativistic Hamiltonian are also eigenfunctions of the operators $\hat{\mathbf{J}}^2, \hat{J}_z$ and $\hat{K}$. Anyways, using (B.14), we can rewrite the kinetic operator in the final form we want to have it:

$$\boldsymbol{\alpha}\cdot\hat{\mathbf{p}} = -i\hbar\boldsymbol{\alpha}\cdot\hat{\mathbf{r}}\frac{\partial}{\partial r} + \frac{i}{|\mathbf{r}|}\boldsymbol{\alpha}\cdot\hat{\mathbf{r}}(\beta\hat{K}-\hbar). \tag{B.19}$$

To shorten notation a little, we write $\sigma_r = \boldsymbol{\sigma}\cdot\hat{\mathbf{r}}$. If we substitute the kinetic operator in the Dirac equation we arrive at:

$$\left[ic\gamma_5\sigma_r\left(\hbar\frac{\partial}{\partial r} + \frac{\hbar}{r} - \frac{\beta\hat{K}}{r}\right) + \beta mc^2 + V(r)\right]\psi(r) = W\psi(r). \tag{B.20}$$

The solutions to this equation can be written as:

$$\psi_\kappa^{m_j}(\mathbf{r}) = \begin{pmatrix} g_\kappa(r)\chi_\kappa^{m_j}(\hat{\mathbf{r}}) \\ if_\kappa(r)\chi_{-\kappa}^{m_j}(\hat{\mathbf{r}}) \end{pmatrix}. \tag{B.21}$$

Usually g_κ is referred to as the large component and f_κ as the small component. The $\chi_\kappa^{m_j}$ are the spin-angular functions which are related to the more familiar spherical harmonics and Pauli spinors by[1]:

$$\begin{aligned} &\text{for} \quad j = l+1/2: \\ &\chi_\kappa^{m_j}(\hat{\mathbf{r}}) = \sqrt{\frac{l+1/2+m}{2l+1}}Y_l^{m_j-1/2}\chi^{1/2} + \sqrt{\frac{l+1/2-m}{2l+1}}Y_l^{m_j+1/2}\chi^{-1/2} \\ &\text{for} \quad j = l-1/2: \\ &\chi_\kappa^{m_j}(\hat{\mathbf{r}}) = \sqrt{\frac{l+1/2-m}{2l+1}}Y_l^{m_j-1/2}\chi^{1/2} - \sqrt{\frac{l+1/2+m}{2l+1}}Y_l^{m_j+1/2}\chi^{-1/2}. \end{aligned} \tag{B.22}$$

[1] I took the expressions given in the book of M. Martin [28] p. 194

If we substitute the solution in the radial Dirac equation and use the not so trivial relation[2] $\sigma_r \chi_\kappa^{m_j}(\hat{\mathbf{r}}) = -\chi_{-\kappa}^{m_j}(\hat{\mathbf{r}})$, we find:

$$\begin{aligned} -c\hbar\left(\frac{\partial}{\partial r}+\frac{1}{r}+\frac{\kappa}{r}\right) g_\kappa(r)\chi_{-\kappa}^{m_j} + (W - V(r) + mc^2) f_\kappa(r)\chi_{-\kappa}^{m_j} = 0 \\ c\hbar\left(\frac{\partial}{\partial r}+\frac{1}{r}-\frac{\kappa}{r}\right) f_\kappa(r)\chi_{\kappa}^{m_j} + (W - V(r) - mc^2) g_\kappa(r)\chi_{\kappa}^{m_j} = 0. \end{aligned} \tag{B.23}$$

Thus the spin-angular functions can be omitted and we are left with two coupled equations for $f_\kappa(r)$ and $g_\kappa(r)$:

$$\begin{aligned} \frac{\partial f_\kappa}{\partial r} &= \frac{1}{c}(V - E) g_\kappa + \frac{\kappa - 1}{r} f_\kappa \\ \frac{\partial g_\kappa}{\partial r} &= -\frac{\kappa + 1}{r} g_\kappa + 2Mc f_\kappa, \end{aligned} \tag{B.24}$$

where we defined $E = W - mc^2$ (the energy of the electron with the mass contribution taken out), put $\hbar = 1$ and used the radially varying mass, which is also called the zrelativistic mass':

$$M = m + \frac{1}{2c^2}(E - V). \tag{B.25}$$

A strategy to solving these two coupled equations is to first rewrite the second equation towards an expression for f_κ and then substituting this expression into the first equation. The result is given by:

$$-\frac{1}{2M}\left[g_\kappa'' + \frac{2}{r}g_\kappa' - \frac{l(l+1)}{r^2} g_\kappa\right] + V g_\kappa - \frac{V' g_\kappa'}{4M^2c^2} - \frac{\kappa + 1}{r}\frac{V' g_\kappa}{4M^2c^2} = E g_\kappa, \tag{B.26}$$

where primes denote radial derivatives and we used that $\kappa(\kappa + 1) = l(l + 1)$. Apart from the two extra terms in the left hand side and that the radial varying mass enters the kinetic energy, this equation is identical to the radial Schrödinger equation. The last term in the left hand side is the spin-orbit term, as it is the only one that still depends on the spin of the particle through κ.

Instead of directly solving (B.26), another approach, proposed by D.D. Koelling and B.N. Harmon [24], is usually taken to deal with relativistic effects for the valence electrons and this for computational reasons. Indeed, if the spin orbit term is taken into account, one has to keep track of the spin, which doubles the size of the secular equation. However, in this approach, spin-orbit coupling can be taken into account afterwards in a second variational step, which is much faster to calculate. Let us first motivate how we can get rid of the spin-orbit term. Imagine that you want to know the average of the solution for the spin-up and the spin-down case. This means that you want to average over $j_1 = l + 1/2$ and $j_2 = l - 1/2$ so that $j_1 + j_2 = 2l$, which is spin independent. Using the relations for the relativistic quantum number (B.17) we find:

$$\kappa_1 + \kappa_2 = l - (l + 1) = -1, \tag{B.27}$$

[2] I will not prove it here, see [49] p. 59 for details.

so that, when adding the two equations for these different κ values, the last term in (B.26) drops out in this case and spin-orbit coupling does not play a role anymore.

We now derive the equations proposed by D.D. Koelling and B.N. Harmon, which is also interesting because it shows us that we can label the wavefunctions with the non-relativistic quantum numbers. We start with defining a new function:

$$\phi_\kappa = \frac{1}{2Mc} g'_\kappa. \tag{B.28}$$

After substitution of this function and its derivative into (B.26) and after dropping the spin-orbit term we get:

$$\phi'_\kappa = -\frac{2}{r}\phi_\kappa + \left[\frac{l(l+1)}{2Mcr^2} + \frac{1}{c}(V-E)\right] g_\kappa. \tag{B.29}$$

After substitution of the definition of ϕ_κ in the second equation of (B.24), we find a relation for f_κ:

$$f_\kappa = \phi_\kappa + \frac{\kappa+1}{2Mcr} g_\kappa, \tag{B.30}$$

which can be substituted in the solution to the radial Dirac equations (B.21):

$$\psi_\kappa^{m_j} \approx \begin{pmatrix} g_\kappa \chi_\kappa^{m_j} \\ i\left[\phi_\kappa + \dfrac{\kappa+1}{2Mcr} g_\kappa\right] \chi_{-\kappa}^{m_j} \end{pmatrix}. \tag{B.31}$$

The second component can be further rewritten:

$$\begin{aligned} i\left[\phi_\kappa + \frac{\kappa+1}{2Mcr} g_\kappa\right] \chi_{-\kappa}^{m_j} &= i\left[\frac{g'_\kappa}{2MC} + \frac{\hat{K}+1}{r} g_\kappa\right] \sigma_r \chi_\kappa^{m_j} \\ &= \frac{i\sigma_r}{2Mc}\left[-g'_\kappa + \frac{\hat{K}-1}{r} g_\kappa\right] \chi_\kappa^{m_j} \\ &= \frac{i\sigma_r}{2Mc}\left[-g'_\kappa + \frac{g_\kappa}{r}\boldsymbol{\sigma}\cdot\hat{\mathbf{L}}\right] \chi_\kappa^{m_j}. \end{aligned} \tag{B.32}$$

In the second step we used that $\hat{K}$ anti-commutes with σ_r[3] and in the last step we used the definition (B.14) of the operator $\hat{K}$. We can now transition to solutions which are labelled by the non-relativistic quantum number lm_lm_s by taking a weighted sum of the spin-up and spin-down states with the same l-value, that is $\kappa = l$ and $\kappa = -(l+1)$:

$$\sqrt{\frac{l+1/2+m}{2l+1}} \chi_l^{m_j} + \sqrt{\frac{l+1/2-m}{2l+1}} \chi_{-l-1}^{m_j} = Y_l^{m_j-1/2} \chi^{1/2} \tag{B.33}$$

or:

$$\sqrt{\frac{l+1/2-m}{2l+1}} \chi_l^{m_j} - \sqrt{\frac{l+1/2+m}{2l+1}} \chi_{-l-1}^{m_j} = Y_l^{m_j+1/2} \chi^{-1/2}, \tag{B.34}$$

[3] See the book of P. Strange [49] p.59

as can easily be verified by using the relations in (B.22). The functions g and g' are determined by (B.28) and (B.29) but since they do not depend on the spin of the particle, we can just as well use l instead of κ. We find for the approximate solutions:

$$\psi_{lm_lm_s} = \begin{pmatrix} g_l Y_l^{m_l} \chi^{m_s} \\ \dfrac{i\sigma_r}{2Mc}\left[-g_l' + \dfrac{g_l}{r}\boldsymbol{\sigma}\cdot\hat{\mathbf{L}}\right] Y_l^{m_l}\chi^{m_s} \end{pmatrix}, \tag{B.35}$$

so we find that the large component is in a pure spin-up or spin-down state while for the small component this is not the case. The equations that are usually implemented are obtained by defining $P_l = rg_l$ and $Q_l = rcg_l$ and then rewriting (B.28) and (B.29) towards:

$$\begin{aligned} P_l' &= 2MQ_l + \frac{P_l}{r} \\ Q_l' &= -\frac{Q_l}{r} + \left[\frac{l(l+1)}{2Mr^2} + (V - E_l)\right] P_l. \end{aligned} \tag{B.36}$$

To construct the wavefunctions inside the spheres we still need the energy derivatives of these equations, which are given by:

$$\begin{aligned} \dot{P}_l' &= 2(\dot{M}Q_l + M\dot{Q}_l)\frac{\dot{P}_l}{r} \\ \dot{Q}_l' &= -\frac{\dot{Q}_l}{r} + \left[\frac{l(l+1)}{2Mr^2} + (V - E_l)\right]\dot{P}_l - \left[\frac{l(l+1)\dot{M}}{2M^2r^2} + 1\right] P_l. \end{aligned} \tag{B.37}$$

In the LAPW method the wavefunction still needs to be matched at the sphere boundary and then the question rises how to do this. After all, in the interstitial part the Schrödinger equation is solved and there is nothing like the small and large part of the wavefunction. The approach that is usually taken is to neglect the contribution of the small component at the sphere boundary and to match the plane waves only to the large component of the wavefunction. Since relativistic corrections are only important near the core, this is usually a good approximation.

We mentioned before that spin-orbit corrections can be taken into account by means of a second variational step. This means that we first solve the above set of equations and find the appropriate eigenfunctions as if there is no spin-orbit coupling at all. Then, with the functions found in this first variational step, one builds a new basis which can be used to set up a Hamiltonian that includes the spin-orbit term. A first thing to realize is that this basis can be much smaller than in the first step since the amount of bands in the system is much lower than the amount of basis functions used in the LAPW basis and only the bands of interest can be included. Secondly, since the spin-orbit term is mostly only important near the nucleus, it usually does not have to be included for the interstitial region. Furthermore, inside the sphere a spherical approximation of the basis functions can be used, again because the spin-orbit term is important near the nucleus and there spherical approximation is best. So in the end we actually only have to calculate the effect of the spin-orbit coupling on the different radial functions $u_l(r)$ and $\dot{u}_l(r)$. The total correction

is then given by a linear combination of these, determined by the expansion coefficients A_{lm} and B_{lm}:

$$\begin{aligned}\langle\phi^{\sigma}_{\mathbf{G}}|\hat{H}^{SO}|\phi^{\sigma'}_{\mathbf{G}'}\rangle = \sum_{lm}\sum_{l'm'}\Big[&A^{*}_{lm}(\mathbf{G})A_{l'm'}(\mathbf{G}')\langle u^{\sigma}_{lm}|\hat{H}^{SO}|u^{\sigma'}_{l'm'}\rangle \\ &+ B^{*}_{lm}(\mathbf{G})A_{l'm'}(\mathbf{G}')\langle \dot{u}^{\sigma}_{lm}|\hat{H}^{SO}|u^{\sigma'}_{l'm'}\rangle \\ &+ A^{*}_{lm}(\mathbf{G})B_{l'm'}(\mathbf{G}')\langle u^{\sigma}_{lm}|\hat{H}^{SO}|\dot{u}^{\sigma'}_{l'm'}\rangle \\ &+ B^{*}_{lm}(\mathbf{G})B_{l'm'}(\mathbf{G}')\langle \dot{u}^{\sigma}_{lm}|\hat{H}^{SO}|\dot{u}^{\sigma'}_{l'm'}\rangle\Big] .\end{aligned} \tag{B.38}$$

The final band energies are then given by the sum of the band energies from the first variation step and these corrections, since the function we use here are orthogonal, i.e. we do not have to calculate the overlap. Finally, because of the form of the spin-orbit term, only terms for which $l = l'$ and $|m - m'| \leq 1$ have to be taken into account. This whole recipe is of course approximate but it works as long as spin-orbit interactions are relatively small.

B.4 Full potential LAPW (FLAPW)

We mentioned in the previous section that using a non-spherical symmetric potential inside the spheres is a little harder than it may seem at first sight. The problem arises when the full crystal potential is used to solve the Poisson equation. Outside the spheres, there is not a big problem since the charge density is expanded in stars (a combination of plane waves which exhibit the spacegroup symmetry) and the equation is diagonal in Fourier space. Inside the spheres, however, we have a rapidly oscillating charge density expanded in lattice harmonics (a combination of spherical harmonics that exhibit the symmetry of the site of the particular atom in the unit cell). Solving the Poisson equation in reciprocal space is prohibitive because of the amount of plane waves that would be required to expand the density near the nucleus. In fact, since we have a delta-function like contribution from the nucleus, such an expansion would be non-convergent. On the other hand, solving the Poisson equation in real space would require some boundary condition that we do not know.
To solve this problem, one can observe that the Coulomb potential outside the spheres only depends on the charge outside the spheres and the multipoles inside. This allows one to replace the true charge density inside the spheres by some other function as long as the multipoles inside stay the same. Thus the Coulomb potential is sought as follows: (1) Extend the charge density expanded in stars to the whole unit cell instead of just in the interstitial part. (2) Calculate the multipoles of the star expansion inside the spheres as well as multipoles of the true charge density. (3) Calculate the difference in multipoles between the true charge density and the star expansion. Then compensate the difference by adding some arbitrary functions, which are localized inside the spheres and can be expanded with as few plane waves as possible, to the star expansion. This is called the pseudo charge density. (4) Solve the Poisson equation in reciprocal space. (5) Find the charge density in real space on the sphere boundary. (6) Solve the Poisson equation inside the sphere in real space with the boundary condition found in the previous step. This can be done with a Green's function approach.

It should now also be clear why there is no problem when considering a spherical symmetric potential inside the spheres. The solution in the interstitial does not depend entirely on the charge distribution inside and the star expansion can immediately be used without the construction of a pseudo charge density. Since the potential in the spheres is approximated to be spherical, the charge distribution that enters the Poisson equation should also be spherical symmetric. This means that we can set $l = 0$ and the equation to be solved becomes:

$$\frac{1}{r^2}\frac{d}{dr}\left(r^2\frac{dV(r)}{dr}\right) = 4\pi\rho(r), \tag{B.39}$$

where $\rho(r)$ is the spherically averaged charge distribution. The above equation is easy to solve, e.g. by integrating the equation twice. The final solution is determined by matching the value and the first derivative of the potential to the solution of the interstitial part on the sphere boundary.

B.5 Local orbitals

Sometimes it is not possible to calculate all electron states accurately with one choice of E_l. This can happen in two cases. The first one occurs when conduction states are to be calculated which have a band energy far above the energy parameter. The second case if there are so-called semi-core states present in the system. These are electron states which have an energy that is far below the valence states but are spatially extended. The latter means that we cannot treat them as core electrons, since the requirement for those is that their wavefunction vanishes (to good approximation at least) in the interstitial region, and we have to treat them as valence states.
The most intuitive reaction is maybe to divide the states in more than one window, each with an appropriate choice for E_l. There are however two downsides to this approach. The first is that creating an extra window increases the computation time significantly since two separate LAPW calculations have to be made (with the only exception that the potential is the same in both cases). Then afterwards the resulting charge densities from these two calculations have to be combined. The second and most important downside is that orthogonality between the states in the separate windows in not guaranteed.
A better approach was proposed by Singh [46], who introduced the local orbital extension for the LAPW method. The idea is to add extra variational freedom to the functions inside the spheres. As discussed before, adding the second derivative $\ddot{u}_l(r)$ would reduce the errors in the band energies to $(\epsilon - E_l)^6$ but would require matching the second derivative of the wavefunction on the sphere boundary, which is prohibitive because of the high plane wave cutoff. Instead, Singh exploited the fact that the LAPW functions are automatically orthogonal to any core state, which allows one to add an arbitrary function to the basis which is strictly confined inside the spheres. Now, since the $u_l(r)$ and $\dot{u}_l(r)$ are particularly suited to approximate wavefunctions inside the spheres, it makes sense to use those. Lastly, the quality of an electron state is determined by the difference between the band energy and the energy parameter E_l used to calculate $u_l(r)$. A clever combination of these properties leads to a representation of

the wavefunctions in the following basis:

$$\psi(\mathbf{r}) = \begin{cases} \Omega^{-1/2} \sum_{\mathbf{G}} c_{\mathbf{G}} e^{i(\mathbf{G}+\mathbf{k})\cdot\mathbf{r}} & \mathbf{r} \in I \\ \sum_{l,m} \left[A_{lm} u_l(r) + B_{lm} \dot{u}_l(r)\right] Y_l^m(\hat{\mathbf{r}}) & \\ \quad + \sum_{l,m} c_{lm} \left[A'_{lm} u_l(r) + B'_{lm} \dot{u}_l(r) + u_l^{(2)}(r)\right] Y_l^m(\hat{\mathbf{r}}) & \mathbf{r} \in S \end{cases}, \quad \text{(B.40)}$$

where the A'_{lm} and B'_{lm} are used to match the extra term and its derivative to zero at the sphere boundary, so that it is strictly localized inside the sphere. The $u_l^{(2)}(r)$ is determined, just like $u_l(r)$, by solving the radial Schrödinger equation but with another choice for the energy parameter E_l. The variational coefficients c_{lm} can be set to zero for all states but those l that have a semi-core state associated with them, and, because of the localized nature of the extra orbitals, only for those atoms that exhibit the semi-core state.

B.6 List of the different parameters used in Elk

This paragraph gives a brief description of the different parameters that we used in DFT calculations with Elk. The parameters are listed alphabetically.

epsengy: Absolute change in the total energy of the system under which the energy is considered as convergence. If the RMS change in the Kohn-Sham potential is also smaller than the set value, the self-consistent loop breaks off.

epspot: RMS change for the Kohn-Sham potential under which the potential is considered to be converged in the self-consistent loop. This condition as well as the absolute change in the energy has to be met before the self-consistent loop stops.

gmaxvr: Sets the maximal length of $|\mathbf{G}|$ for expanding the electron density and potential in the interstitial region.

kgrid: Determines the equidistant grid of points in reciprocal space at which the Kohn-Sham equations are solved.

lmaxapw: Set the angular momentum cutoff $l_{\max}$ for expanding the one-electron wavefunctions inside the spheres.

lmaxmat: Sets the angular momentum cutoff for the construction of non-spherical contributions to the Hamiltonian and overlap of the system inside the spheres. Raising this parameter can significantly increase computation times and thus is usually set lower than other angular cutoff parameters in the calculation (as much as the convergence criterium permits at least).

lmaxvr: Sets the angular momentum cutoff $l_{\max}$ for the functions inside the spheres for expanding the electron density and potential.

lorbcnd: Either true or false. If set to true, Elk automatically adds local orbitals to the high lying conduction states. This is required for an accurate determination of their band energies.

nempty: Determines the number of empty states per atom and per spin. (If this parameter would be set to zero, there would be as many states calculated as there are valence electrons in the system.)

rgkmax: Sets the energy cutoff for the plane waves for approximating the wavefunctions by defining the maximum length of the $\mathbf{G}+\mathbf{k}$ vectors through:

$$\max\{|\mathbf{G}+\mathbf{k}|\} = \frac{\text{rgkmax}}{R_S}, \tag{B.41}$$

where R_S is the average of the sphere radii of the different atoms in the system. The energy cutoff, in Hartree, of the plane waves is then given by:

$$E_{\max}^{PW} = \frac{(\max\{|\mathbf{G}+\mathbf{k}|\})^2}{2}. \tag{B.42}$$

Care has to be taken when raising this parameter because Heaviside functions are used in the construction of the Hamiltonian and overlap matrices for the interstitial part. A consequence of this is that spurious energy contributions from Gibbs oscillations can show up and cause the self-consistent loop to break down due to divergence of the electron density.

stype: Used to define what kind of function should be used to determine the occupancy of the electron states.

swidth: Determines the temperature used for the smearing function as well as the inverse lifetime of particle excitations when calculating response functions.

Appendix C

Potential of a charge near a dielectric

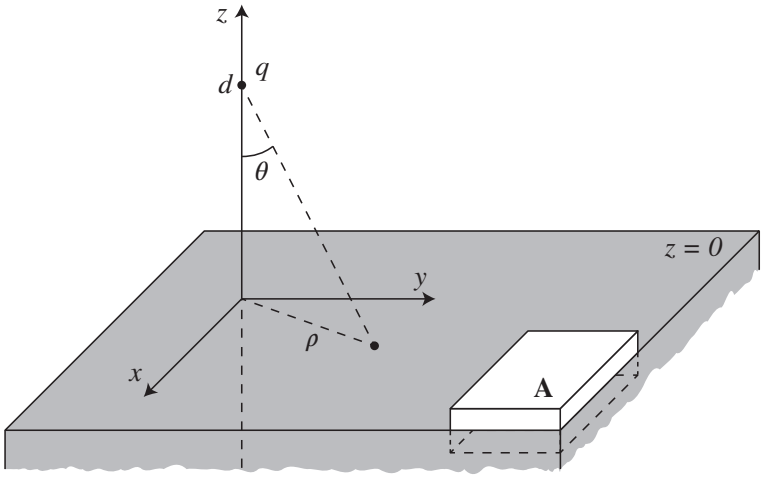

Figure C.1: A schematic picture of the system under consideration in this appendix. The left figure shows the charge q, which is situated at a distance d above the infinite surface of a dielectric. In the right hand side of the figure, the surface that we use with Gauss' law to determine the electric field due to the surface charge σ_i is drawn.

In this chapter we derive the potential for a point charge q at a distance d from the surface of a dielectric material, as shown in figure C.1. We suppose that we are dealing with a linear dielectric, i.e. the polarization can be written as:

$$\mathbf{P} = \epsilon_0 \chi_e \mathbf{E}, \tag{C.1}$$

where ϵ_0 is the permitivity of the vacuum and χ_e is the electric susceptibility. Note that we adopt SI units in this appendix. The quantity we want to know

is the potential caused by the charge, which is given by the Poisson equation:

$$\nabla^2 V(\mathbf{r}) = \frac{\rho(\mathbf{r})}{\epsilon_0}, \tag{C.2}$$

where $\rho(\mathbf{r})$ is the charge density of the system. The charge density is not solely given by the point charge because the point charge will induce a charge in the dielectric. Our first task is thus to find the induced charge. The induced charge can be divided in a surface charge and a bulk charge. The latter is zero because it is proportional to the free charge density embedded in the material:

$$\rho_i = -\nabla \cdot \mathbf{P} = -\nabla \cdot \left(\epsilon_0 \frac{\chi_e}{\epsilon}\mathbf{D}\right) = -\left(\frac{\chi_e}{1+\chi_e}\right)\rho_f, \tag{C.3}$$

where $\epsilon = \epsilon_0(1+\chi_e)$ is the permittivity of the material and $\mathbf{D} = \epsilon\mathbf{E}$ is the displacement vector. In the last step we used Gauss' law for polarizable media $\nabla\cdot\mathbf{D} = \rho_f$, where ρ_f denotes the free charge in the medium. The surface charge is given by:

$$\sigma_i = \mathbf{P}\cdot\hat{\mathbf{n}} = P_z = \epsilon_0\chi_e E_z \tag{C.4}$$

Here, E_z is the z-component of the electrical field at $z = 0$. The electrical field has a contribution from the free charge above the surface, which is easily found from Coulomb's law:

$$-\frac{1}{4\pi\epsilon_0}\frac{q}{\rho^2+d^2}\cos\theta = -\frac{1}{4\pi\epsilon_0}\frac{qd}{(\rho^2+d^2)^{3/2}}. \tag{C.5}$$

The second contribution comes from the surface charge, which can be found from Gauss' law by drawing a rectangular box around the surface, as indicated in the figure.

$$\oint_A \mathbf{E}\cdot d\mathbf{A} = \frac{1}{\epsilon_0}\int \rho\, dV \quad \Rightarrow \quad 2AE_z = -\frac{\sigma_i}{\epsilon_0} \tag{C.6}$$

We have a minus sign because we are looking just inside the dielectric at $z = 0$. Taken together, (C.4),(C.5) and (C.6) yield an equation from which we can determine the induced surface charge:

$$\begin{aligned} \sigma_i &= \epsilon_0\chi_e\left(-\frac{1}{4\pi\epsilon_0}\frac{qd}{(\rho^2+d^2)^{3/2}} - \frac{\sigma_i}{2\epsilon_0}\right) \\ \Rightarrow \sigma_i &= -\frac{1}{2\pi}\left(\frac{\chi_e}{\chi_e+2}\right)\frac{qd}{(\rho^2+d^2)^{3/2}}. \end{aligned} \tag{C.7}$$

The total induced charge is thus given by:

$$q_i = -\left(\frac{\chi_e}{\chi_e+2}\right)q. \tag{C.8}$$

We adopt the method of the image charges to find the potential. The method relies on a collorary of one of the uniqueness theorems to the solutions of the Laplace equation. It tells us that, quoting from Griffiths book [16]: 'The potential in a volume V is uniquely determined if (a) the charge density throughout

the region, and (b) the value of V on all boundaries are specified'. This means that if we can find a solution that satisfies all the boundary conditions and gives us the correct charge density, it is the *only* solution to the Poisson equation we can find. The method of the image charges places some fictitious charges somewhere outside the region where the solution is sought and in such a way that the boundary conditions are satisfied. How exactly that the image charges have to be placed, is usually a matter of a making a well reasoned guess. There are, however, two rules of the thumb: (1) You can never place an image charge inside the region where you are looking for the potential and (2) the image charges have to add up to the correct total charge in each region. The boundary conditions are given by:

$$E^{\parallel}_{\text{vac}} - E^{\parallel}_{\text{diellectric}} = \frac{\sigma}{\epsilon_0} \quad \text{and} \quad E^{t}_{\text{vac}} - E^{t}_{\text{diellectric}} = 0, \tag{C.9}$$

where $E^{\parallel}$ denotes the component of the electric field along the normal of the plane, E^t the component of the electrical field tangent to the plane and σ the surface charge. The potential also has to disappear far away from the point charge:

$$V \to 0 \quad \text{if} \quad \rho^2 + z^2 \gg d^2 \tag{C.10}$$

Following the rules mentioned above, we make the guess that for $z > 0$, we have to place an image charge at $-d$ with a charge equal to q_i:

$$V = \frac{1}{4\pi\epsilon_0}\left(\frac{q}{\sqrt{\rho^2 + (z-d)^2}} + \frac{q_i}{\sqrt{\rho^2 + (z+d)^2}}\right), \tag{C.11}$$

which corresponds with placing an image charge at $z = -d$ with a charge equal to the induced charge. For $z < 0$ we pose:

$$V = \frac{1}{4\pi\epsilon_0}\left(\frac{q + q_i}{\sqrt{\rho^2 + (z-d)^2}}\right). \tag{C.12}$$

The electric field is given by $-\nabla V$, so that we find:

$$-\left(\left.\frac{\partial V}{\partial z}\right|_{z=0^+} - \left.\frac{\partial V}{\partial z}\right|_{z=0^-}\right) = -\frac{1}{2\pi}\left(\frac{\chi_e}{\chi_e + 2}\right)\frac{qd}{(\rho^2 + d^2)^{3/2}}, \tag{C.13}$$

which is exactly the induced surface charge so that the first boundary condition of (C.9) is satisfied. It is easy to check that the rest of the boundary conditions are also satisfied. This means that the potential we proposed, is the solution to the Poisson equation for our problem.

Appendix D

Details 2 particles approach

D.1 Energy Functional Positron

In the two particle description, the effect of the solid is modeled by the Coulomb potential and the exchange and correlation potential of the solid. The Coulomb potential as well as the electron exchange and correlation potential, we can calculate with the DFT package Elk. For the positron, no routines are implemented in the code to calculate the correlation potential. Instead, we take the electron density as calculated by Elk and from this we can determine the correlation potential for the positron. We chose to use the recent LDA functional parametetrized by Drummond [14]. This functional is obtained from a quantum Monte Carlo study of the homogeneous electron gas with and without a single immersed positron. This quantity is the relaxation energy and is equal to the electron-positron correlation energy. The functional is given in terms of the local *electron* density by the form:

$$V_{XC}(\mathbf{r}_p) = \Delta\Omega(r_s) = \frac{A_{-1}r_s^{-1} + A_0 + A_1 r_s + A_2 B_2 r_s^2}{1 + B_1 r_s + B_2 r_s^2}, \tag{D.1}$$

where $r_s = 3/(4\pi n)$ is the electron density parameter and n the electron density. The parameters are given by $A_{-1} = -0.260\,361$, $A_0 = -0.261\,762$, $A_1 = 0.003\,755\,34$, $A_2 = -0.262\,005$, $B_1 = 0.113\,718$ and $B_2 = 0.027\,091\,2$. The functional tends to the correct low density limits but not the correct high density limit. The latter, though, is not relevant for the problem we are dealing with.

D.2 Hartree and cross-image potential

The potential due to the presence of the other particle in our two particle approach is determined by the Hartree potential and the cross-image potential. We show here how we can evaluate these integrals. We only consider the Hartree potential, since the cross-image potential is easily obtained from this result by replacing $z - z'$ by $z + z' - 2z_1$:

$$\int_0^\infty d\varrho'\, \varrho' \int_{-\infty}^{\infty} dz' \int_0^{2\pi} d\theta' \frac{\rho(\varrho', z')}{\sqrt{\varrho'^2 + \varrho^2 - 2\varrho'\varrho\cos(\theta' - \theta) + (z' - z)^2}} \tag{D.2}$$

Since we expect no dependence on the angle, we can put $\theta = 0$. The integral can be rewritten to:

$$\int_0^\infty d\varrho'\,\varrho' \int_{-\infty}^{\infty} dz' \frac{\rho(\varrho', z')}{\sqrt{(\varrho'+\varrho)^2 + (z'-z)^2}} \int_0^{2\pi} \frac{d\theta'}{\sqrt{1 - \dfrac{2\varrho'\varrho\,(1+\cos(\theta'))}{(\varrho'+\varrho)^2 + (z'-z)^2}}} \tag{D.3}$$

The integral over the angle can be worked out analytically. If we consecutively put $\theta'' = \theta - \pi$, $\cos(\theta'' + \pi) = -\cos(\theta'')$, $1 - \cos(\theta'') = 2\sin(\theta''/2)$, $\theta''' = \theta''/2$, then the integral becomes:

$$4\int_0^{\pi/2} \frac{d\theta'''}{\sqrt{1 - \dfrac{4\varrho'\varrho}{(\varrho'+\varrho)^2 + (z'-z)^2}\sin^2(\theta''')}} = 4K\left(\frac{4\varrho'\varrho}{(\varrho'+\varrho)^2 + (z'-z)^2}\right), \tag{D.4}$$

where $K(m)$ is the complete elliptic integral of the first kind[1]. If we would use the trapezoid rule to evaluate the resulting integral, we would get a logarithmic divergence near the origin. Instead, we use the polynomial approximation to the elliptic integral found in [1]:

$$\begin{aligned} K(m) &= \left(a_0 + a_1 m_1 + a_2 m_1^2 + a_3 m_1^3 + a_4 m_1^4\right) \\ &\quad + \left(b_0 + b_1 m_1 + b_2 m_1^2 + b_3 m_1^3 + b_4 m_1^4\right) \ln\left(\frac{1}{m_1}\right) \\ &= A(m_1) - B(m_1)\ln(m_1), \end{aligned} \tag{D.5}$$

where $m_1 = 1 - m$ and:

$$\begin{aligned} a_0 &= 1.386\,294\,361\,12, & b_0 &= 0.5, \\ a_1 &= 0.096\,663\,442\,59, & b_1 &= 0.124\,985\,935\,97, \\ a_2 &= 0.035\,900\,923\,83, & b_2 &= 0.068\,802\,485\,76, \\ a_3 &= 0.037\,425\,637\,13, & b_3 &= 0.033\,283\,553\,46, \\ a_4 &= 0.014\,511\,962\,12, & b_4 &= 0.004\,417\,870\,12. \end{aligned}$$

The Hartree potential becomes:

$$\begin{aligned} 4\int_{-\infty}^{\infty} dz' \int_0^\infty d\varrho' \frac{\varrho'\rho(\varrho', z')}{\sqrt{(\varrho'+\varrho)^2 + (z'-z)^2}} \Bigg\{ A\left(\frac{(\varrho'-\varrho)^2 + (z'-z)^2}{(\varrho'+\varrho)^2 + (z'-z)^2}\right) \\ -B\left(\frac{(\varrho'-\varrho)^2 + (z'-z)^2}{(\varrho'+\varrho)^2 + (z'-z)^2}\right) \ln\left(\frac{(\varrho'-\varrho)^2 + (z'-z)^2}{(\varrho'+\varrho)^2 + (z'-z)^2}\right) \Bigg\}. \end{aligned} \tag{D.6}$$

We can evaluate the term with A with the trapezoid rule but for the the term with B and the logarithm we will see the logarithmic divergence near the origin. Instead, we will use the 'logarithmically weighted method' to evaluate the integral over ϱ' [21]. We can write this integral as:

$$\sum_{i=1}^{N} \int_0^{h_{i+1}-h_i} d\varrho' F(\varrho' + h_i) \ln\left(\frac{(\varrho' - (\varrho - h_i))^2 + (z'-z)^2}{(\varrho' + (\varrho + h_i))^2 + (z'-z)^2}\right), \tag{D.7}$$

[1] We used the convention where $K(m) = \int_0^{\pi/2} d\theta (1 - m\sin^2(\theta))^{-1/2}$ as in the 1970 version of Abramowitz. The new NIST Handbook of Mathematical Functions puts $k^2 = m$.

where h_i denotes the radial coordinate of the grid points. We approximate F by the linear interpolation between the endpoints of each of these integrals:

$$F(\varrho' + h_i) = F_i + \frac{F_{i+1} - F_i}{h_{i+1} - h_i}\varrho' \tag{D.8}$$

since this allows us to rewrite the integral to:

$$\sum_{i=1}^{N} \left[F_i C_i(\varrho, z, z') + \frac{F_{i+1} - F_i}{h_{i+1} - h_i} D_i(\varrho, z, z') \right], \tag{D.9}$$

where N is the amount of gridpoints on which we know F. The C_i and D_i can be evaluated analytically:

$$C_i(\varrho, z, z') = \int_0^{h_{i+1}-h_i} d\varrho' \ln\left(\frac{(\varrho' - (\varrho - h_i))^2 + (z' - z)^2}{(\varrho' + (\varrho + h_i))^2 + (z' - z)^2} \right). \tag{D.10}$$

If we write the devision in the logarithm as a difference of logarithms and subsequently substitute $y_1 = \varrho' - (\varrho - h_i)$ and $y_2 = \varrho' + (\varrho + h_i)$, then we get integrals of the form:

$$\int dy \ln(y^2 + a^2) = y \ln(y^2 + a^2) - 2y + 2a \operatorname{atan}\left(\frac{y}{a}\right). \tag{D.11}$$

To keep notation in check and for convenience of implementation, we introduce the following notations:

$$\varrho_i^{\pm} = h_i \pm \varrho, \quad z^{\pm} = z' \pm z, \quad P(a, b) = \ln(a^2 + b^2). \tag{D.12}$$

The result then becomes:

$$\begin{aligned} C_i(\varrho, z, z') = {} & \varrho_{i+1}^- P(\varrho_{i+1}^-, z^-) - \varrho_i^- P(\varrho_i^-, z^-) - \varrho_{i+1}^+ P(\varrho_{i+1}^+, z^-) + \varrho_i^+ P(\varrho_i^+, z^-) \\ & + 2z^- \left[\operatorname{atan}\left(\frac{\varrho_{i+1}^-}{z^-}\right) - \operatorname{atan}\left(\frac{\varrho_i^-}{z^-}\right) - \operatorname{atan}\left(\frac{\varrho_{i+1}^+}{z^-}\right) + \operatorname{atan}\left(\frac{\varrho_i^+}{z^-}\right) \right]. \end{aligned} \tag{D.13}$$

For D_i we can use the same substitutions as before and this gives integrals of the form of (D.11) as well as:

$$\int dy\, y \ln(y^2 + a^2) = \frac{1}{2}\left[(y^2 + a^2)\ln(y^2 + a^2) - y^2 \right]. \tag{D.14}$$

The result is given by:

$$\begin{aligned} D_i(\varrho, z, z') = {} & \frac{1}{2}\left\{ \left[(\varrho_{i+1}^-)^2 + (z^-)^2\right] P(\varrho_{i+1}^-, z^-) - \left[(\varrho_i^-)^2 + (z^-)^2\right] P(\varrho_i^-, z^-) \right. \\ & - \left[(\varrho_{i+1}^+)^2 + (z^-)^2\right] P(\varrho_{i+1}^+, z^-) + \left. \left[(\varrho_i^+)^2 + (z^-)^2\right] P(\varrho_i^+, z^-) \right\} - 2\varrho(h_{i+1} - h_i) \\ & - \varrho_i^- \left\{ \varrho_{i+1}^- P(\varrho_{i+1}^-, z^-) - \varrho_i^- P(\varrho_i^-, z^-) + 2z^- \left[\operatorname{atan}\left(\frac{\varrho_{i+1}^-}{z^-}\right) - \operatorname{atan}\left(\frac{\varrho_i^-}{z^-}\right) \right] \right\} \\ & + \varrho_i^+ \left\{ \varrho_{i+1}^+ P(\varrho_{i+1}^+, z^-) - \varrho_i^+ P(\varrho_i^+, z^-) + 2z^- \left[\operatorname{atan}\left(\frac{\varrho_{i+1}^+}{z^-}\right) - \operatorname{atan}\left(\frac{\varrho_i^+}{z^-}\right) \right] \right\}. \end{aligned} \tag{D.15}$$

Time to recapitulate. We are interested in the Hartree potential which is determined by the integral (D.2). By carrying out the integral over the angle analytically and by introducing the polynomial approximation to the complete elliptic integral of the first kind, we obtain (D.6). The term with A can be evaluated numerically with the trapezoid rule but for the integrals over term with B and the logarithm this does not give good results. Instead, we carry out the integral over the radial coordinate with the logarithmically weighted method (D.9), in which C_i and D_i are given by (D.13) and (D.15) respectively. The resulting integral over z' can then be carried out with the trapezoid rule.

D.3 Finite differences scheme

We wish to solve the two-dimensional one particle equations on a inhomogeneous grid since this allows us to keep the amount of grid points necessary reasonable. Indeed, we expect that the wavefunction will vary strongly near the minimum of the potential and that it will slowly decay to zero for large ϱ and z. We start by integrating the Schrödinger equation:

$$\int_{\varrho_{i-\frac{1}{2}}}^{\varrho_{i+\frac{1}{2}}} d\varrho\, \varrho \int_{z_{j-\frac{1}{2}}}^{z_{j+\frac{1}{2}}} \left\{ -\frac{1}{2\varrho}\frac{\partial}{\partial\varrho}\left(\varrho\frac{\partial}{\partial\varrho}\right) - \frac{1}{2}\frac{\partial^2}{\partial z^2} + V(\varrho,z) \right\} \psi = \int_{\varrho_{i-\frac{1}{2}}}^{\varrho_{i+\frac{1}{2}}} d\varrho\, \varrho \int_{z_{j-\frac{1}{2}}}^{z_{j+\frac{1}{2}}} \varepsilon\, \psi \tag{D.16}$$

We can work out these integrals approximately by assuming that the wavefunction and the potential are constant over these intervals and equal to the value of the midpoint. The first term in the left hand side gives:

$$\begin{aligned} &-\frac{1}{2}(z_{j+\frac{1}{2}} - z_{j-\frac{1}{2}}) \int_{\varrho_{i-\frac{1}{2}}}^{\varrho_{i+\frac{1}{2}}} d\varrho \left(\frac{\partial\psi^j}{\partial\varrho} + \varrho\frac{\partial^2\psi^j}{\partial\varrho^2} \right) \\ &= -\frac{1}{2}(z_{j+\frac{1}{2}} - z_{j-\frac{1}{2}}) \left(\varrho_{i+\frac{1}{2}} \frac{\psi^j_{i+1} - \psi^j_i}{\varrho_{i+1} - \varrho_i} - \varrho_{i-\frac{1}{2}} \frac{\psi^j_i - \psi^j_{i-1}}{\varrho_i - \varrho_{i-1}} \right), \end{aligned} \tag{D.17}$$

where we used partial integration on the second term and used the midpoint rule to approximate the resulting first derivative. We apply the same two steps on the second derivative w.r.t. the z-direction to obtain:

$$-\frac{1}{4}(\varrho^2_{i+\frac{1}{2}} - \varrho^2_{i-\frac{1}{2}}) \left(\frac{\psi^{j+1}_i - \psi^j_i}{z_{j+1} - z_j} - \frac{\psi^j_i - \psi^{j-1}_i}{z_j - z_{j-1}} \right). \tag{D.18}$$

The potential term gives:

$$\frac{1}{2}(\varrho^2_{i+\frac{1}{2}} - \varrho^2_{i-\frac{1}{2}})(z_{j+\frac{1}{2}} - z_{j-\frac{1}{2}}) V^j_i \psi^j_i. \tag{D.19}$$

The right hand side is obtained by replacing V^j_i by ε in this expression. To obtain a scheme in which the resulting matrix is Hermitian, we define the step sizes [21]:

$$h_i = \sqrt{\frac{\varrho^2_{i+\frac{1}{2}} - \varrho^2_{i-\frac{1}{2}}}{2}}, \quad \text{and} \quad h^j = \sqrt{z_{j+\frac{1}{2}} - z_{j-\frac{1}{2}}}. \tag{D.20}$$

If we divide both sides of the equation by $h_i h^j$, we obtain:

$$
\begin{aligned}
&-\frac{1}{2}\left(\varrho_{i+\frac{1}{2}}\frac{h_{i+1}h^j\psi_{i+1}^j}{h_{i+1}h_i(\varrho_{i+1}-\varrho_i)}-\varrho_{i+\frac{1}{2}}\frac{h_ih^j\psi_i^j}{(h_i)^2(\varrho_{i+1}-\varrho_i)}-\varrho_{i-\frac{1}{2}}\frac{h_ih^j\psi_i^j}{(h_i)^2(\varrho_i-\varrho_{i-1})}\right.\\
&\left.+\varrho_{i-\frac{1}{2}}\frac{h_{i-1}h^j\psi_{i-1}^j}{h_ih_{i-1}(\varrho_i-\varrho_{i-1})}\right)-\frac{1}{2}\left(\frac{h_ih^{j+1}\psi_i^{j+1}}{h^{j+1}h^j(z_{j+1}-z_j)}-\frac{h_ih^j\psi_i^j}{(h^j)^2(z_{j+1}-z_j)}\right.\\
&\left.-\frac{h_ih^j\psi_i^j}{(h^j)^2(z_j-z_{j-1})}+\frac{h_ih^{j-1}\psi_i^{j-1}}{h^jh^{j-1}(z_j-z_{j-1})}\right)+V_i^jh_ih^j\psi_i^j=\varepsilon h_ih^j\psi_i^j.
\end{aligned}
\tag{D.21}
$$

We made sure that the h come in combinations with the same indices as the ψ, such that we can search for the auxiliary function $\phi_i^j = h_i h^j \psi_i^j$ by solving the resulting matrix equation. To make implementation less confusing, we multiply the indices by two so we get rid of the half-index notations. We then provide a potential defined on the even numbered indices and obtain the auxiliary function on the even indices by solving the matrix equation. On the main diagonal we have:

$$
\begin{aligned}
&\frac{1}{2}\left(\varrho_{2i+1}\frac{\phi_{2i}^{2j}}{(h_{2i})^2(\varrho_{2i+2}-\varrho_{2i})}+\varrho_{2i-1}\frac{\phi_{2i}^{2j}}{(h_{2i})^2(\varrho_{2i}-\varrho_{2i-2})}\right)\\
&+\frac{1}{2}\left(\frac{\phi_{2i}^{2j}}{(h^{2j})^2(z_{2j+2}-z_{2j})}+\frac{\phi_{2i}^{2j}}{(h^{2j})^2(z_{2j}-z_{2j-2})}\right)+V_{2i}^{2j}\phi_{2i}^{2j}
\end{aligned}
\tag{D.22}
$$

On the off-diagonal for ϱ we have:

$$
-\frac{\varrho_{2i+1}}{2}\frac{\phi_{2i+2}^{2j}}{h_{2i+2}h_{2i}(\varrho_{2i+2}-\varrho_{2i})}\quad\text{and}\quad-\frac{\varrho_{2i-1}}{2}\frac{\phi_{2i-2}^{2j}}{h_{2i}h_{2i-2}(\varrho_{2i}-\varrho_{2i-2})}
\tag{D.23}
$$

and on the off-diagonal for z:

$$
-\frac{1}{2}\frac{\phi_{2i}^{2j+2}}{h^{2j+2}h^{2j}(z_{2j+2}-z_{2j})}\quad\text{and}\quad-\frac{1}{2}\frac{\phi_{2i}^{2j-2}}{h^{2j}h^{2j-2}(z_{2j}-z_{2j-2})}.
\tag{D.24}
$$

That the resulting matrix equation is hermitian can be checked by putting $j = l$ in the left expression and $j = l+1$ in the right expression, which obviously give the same result.

Bibliography

[1] M. Abramowitz and I. A. Stegun. *Handbook of mathematical functions*. Dover Publications, 1970.

[2] Ana Akrap, Michaël Tran, Alberto Ubaldini, Jérémie Teyssier, Enrico Giannini, Dirk van der Marel, Philippe Lerch, and Christopher C. Homes. Optical properties of Bi_2Te_2Se at ambient and high pressures. *Physical Review B*, 86(23):235207, December 2012.

[3] O. Krogh Andersen. Linear methods in band theory. *Physical Review B*, 12(8):3060–3083, 1975.

[4] T. Bates and A. H. Weiss. Positronium formation at the Surface of a Topological Insulator, 2014.

[5] O. V. Boev, M. J. Puska, and R. M. Nieminen. Electron and positron energy levels in solids. *Physical Review B*, 36(15):7786–7794, 1987.

[6] L. W. Bruch, W. C. Milton, and E. Zaremba. *Physical Adsorption: Forces and Phenomena*. Oxford University Press, 1997.

[7] A. H. Castro Neto, N. M. R. Peres, K. S. Novoselov, and A. K. Geim. The electronic properties of graphene. *Reviews of Modern Physics*, 81:109–162, January 2009.

[8] Jiwon Chang, Leonard F. Register, Sanjay K. Banerjee, and Bhagawan Sahu. Density functional study of ternary topological insulator thin films. *Physical Review B*, 83(23):235108, June 2011.

[9] Yi-Chen Cheng, Hsin-Yi Huang, and Chih-Kai Yang. The Surface Dielectric Function and Its Sum Rule for a Semi-Infinite Electron System. *Chinese Journal of Physics*, 33(2):169–180, 1995.

[10] Gradient correction for positron states in Solids. Gradient correction for positron states. *Physical Review B*, 51(11):7341–7344, 1995.

[11] A. Cuthbert. Positronium binding to metal surfaces. *Journal of Physics C: Solid State Physics*, 18:4561–4579, 1985.

[12] Xian-Qi Dai, Bao Zhao, Jian-Hua Zhao, Yan-Hui Li, Ya-Nan Tang, and Ning Li. Robust surface state of intrinsic topological insulator Bi_2Te_2Se thin films: a first-principles study. *Journal of physics: Condensed matter*, 24(035502), January 2012.

[13] A. Dalgarno and G. A. Victor. Long range three-body forces between helium and hydrogen atoms. *Molecular Physics*, 10:333–337, 1966.

[14] N D Drummond, P López Ríos, R J Needs, and C J Pickard. Quantum Monte Carlo study of a positron in an electron gas. *Physical review letters*, 107(20):207402, November 2011.

[15] Stephan W H Eijt, Anton Van Veen, Henk Schut, Peter E Mijnarends, A R T B Denison, Bernardo Barbiellini, and Arun Bansil. Study of colloidal quantum-dot surfaces using an innovative thin-film positron 2D-ACAR method. *Nature Materials*, 5(January):23–26, 2006.

[16] David J. Griffiths. *Introduction to Electrodynamics*. Prentice Hall, 1999.

[17] Theo Hanh, editor. *International tables for crystallography*. 2nd. edition, 1989.

[18] M. Z. Hasan and C. L. Kane. Colloquium: Topological insulators. *Reviews of Modern Physics*, 82:3045–3067, November 2010.

[19] P. Hohenberg and W. Kohn. Inhomogeneous Electron Gas. *Physical Review*, 136:864–871, 1964.

[20] Jl Hughes and Je Sipe. Calculation of second-order optical response in semiconductors. *Physical review. B, Condensed matter*, 53(16):10751–10763, April 1996.

[21] Karen Janssens. *Self-assembled quantum dots*. PhD thesis, University of Antwerp, 2003.

[22] Y. Jean, Renwu Zhang, H. Cao, Jen-Pwu Yuan, Chia-Ming Huang, B. Nielsen, and P. Asoka-Kumar. Glass transition of polystyrene near the surface studied by slow-positron-annihilation spectroscopy. *Physical Review B*, 56(14):R8459–R8462, October 1997.

[23] C. L. Kane and E. J. Mele. Quantum Spin Hall Effect in Graphene. *Physical Review Letters*, 95(22):226801, November 2005.

[24] D D Koelling and B N Harmon. A technique for relativistic spin-polarised calculations. *Journal of Physics C: Solid State Physics*, 10(16):3107–3114, 2001.

[25] W. Kohn and L. J. Sham. Self-Consistent Equations Including Exchange and Correlation Effects. *Physical Review*, 140:1133–1138, 1965.

[26] Ortwin Leenaerts. *An ab initio study of the adsorption of atoms and molecules on graphene*. PhD thesis, Universiteit Antwerpen, 2010.

[27] Z.W. Liu, H.J. Zhang, and Z.Q. Chen. Monolayer dispersion of CoO on Al2O3 probed by positronium atom. *Applied Surface Science*, 293:326–331, February 2014.

[28] Richard M. Martin. *Electronic Structure: Basic Theory and Practical Methods*. Cambridge University Press, 2004.

[29] R. Mehrem. The plane wave expansion, infinite integrals and identities involving spherical Bessel functions. *Applied Mathematics and Computation*, 217:5360–5365, February 2011.

[30] Brij Mohan, Ashok Kumar, and P.K. Ahluwalia. A first principle study of interband transitions and electron energy loss in mono and bilayer graphene: Effect of external electric field. *Physica E: Low-dimensional Systems and Nanostructures*, 44(7-8):1670–1674, April 2012.

[31] S. Nakajima. The crystal structure of $Bi_2Te_{3-x}Se_x$. *Journal of Chemical Solids*, 24:479–485, 1963.

[32] M. Neupane, S. Basak, N. Alidoust, S. Y. Xu, C. Liu, I. Belopolski, G. Bian, J. Xiong, H. Ji, S. Jia, S-K. Mo, M. Bissen, M. Severson, H. Lin, N. P. Ong, T. Durakiewicz, R. J. Cava, A. Bansil, and M. Z. Hasan. Oscillatory surface dichroism of an insulating topological insulator Bi_2Te_2Se. *Physical Review B*, 88(165129), October 2013.

[33] P.O. Nilsson. Optical Properties of Metal and Alloys. In H. Ehrenreich, F. Seitz, and D. Turnbull, editors, *Solid State Physics vol. 29*, page 139. 1974.

[34] P. Nordlander and J. Harris. The interaction of helium with smooth metal surfaces. *Journal of Physics C: Solid State Physics*, 17:1141–1152, 1984.

[35] B. Partoens and F. Peeters. From graphene to graphite: Electronic structure around the K point. *Physical Review B*, 74(7):075404, August 2006.

[36] S. H. Patil, K. T. Tang, and J. P. Toennies. Damping functions for the pairwise sum model of the atomsurface potential. *Journal of Chemical Physics*, 116(18):8118–8123, 2002.

[37] Jb Pendry, Aj Holden, Wj Stewart, and I Youngs. Extremely low frequency plasmons in metallic mesostructures. *Physical review letters*, 76(25):4773–4776, June 1996.

[38] J. P. Perdew, K. Burke, and M. Ernzerhof. Generalized gradient approximation made simple. *Physical Review Letters*, 77:3865–3868, 1996.

[39] J. P. Perdew and Alex Zunger. Self-interaction correction to density-functional approximations for many-electron systems. *Physical Review B*, 23(10):5048–5079, 1981.

[40] Philip Phillips. *Advanced Solid State Physics*. Cambridge University Press, 2nd edition, 2012.

[41] Helmut Rathgen and Mikhail I Katsnelson. Symmetry Assumptions , Kramers Kronig Transformation and Analytical Continuation in Ab Symmetry Assumptions , Kramers Kronig Transformation and Analytical Continuation in Ab Initio Calculations of Optical Conductivities. *Physica Scripta*, T109:170–174, 2004.

[42] Zhi Ren, a. a. Taskin, Satoshi Sasaki, Kouji Segawa, and Yoichi Ando. Large bulk resistivity and surface quantum oscillations in the topological insulator Bi_2Te_2Se. *Physical Review B*, 82(241306), December 2010.

[43] R Saniz, B Barbiellini, P M Platzman, and a J Freeman. Physisorption of positronium on quartz surfaces. *Physical review letters*, 99(096101), August 2007.

[44] Wahyu Setyawan and Stefano Curtarolo. High-throughput electronic band structure calculations: Challenges and tools. *Computational Materials Science*, 49(2):299–312, April 2010.

[45] K. Shastry, P. V. Joglekar, Z. H. Lim, B. Barbiellini, and A. H. Weiss. Evidence for a positron bound state on the surface of a topological insulator, 2014.

[46] David Singh. Ground-state properties of lanthanum: Treatment of extended-core states. *Physical Review B*, 43(8):6388–6392, 1991.

[47] David J. Singh and L. Nordström. *Planewaves, Pseudopotentials and The LAPW Method*. Springer Science, 2006.

[48] An Slachmuylders. *A theoretical study of excitons and impurities in free-standing nanowires*. PhD thesis, University of Antwerp, 2008.

[49] Paul Strange. *Relativistic Quantum Mechanics*. Cambridge University Press, 1998.

[50] Radosaw Szmytkowski. Dynamic polarizability of the relativistic hydrogen-like atom: Application of the Sturmian expansion of the Dirac-Coulomb Green function. *Physical Review A*, 65(1):012503, December 2001.

[51] D. J. Thouless, M. Kohmoto, M. P. Nightingale, and M. den Nijs. Quantized Hall Conductance in a Two-Dimensional Periodic Potential. *Physical review letters*, 49(6):405–408, 1982.

[52] Filip Tuomisto and Ilja Makkonen. Defect identification in semiconductors with positron annihilation: Experiment and theory. *Reviews of Modern Physics*, 85(4):1583–1631, 2013.

[53] M. van Schilfgaarde and M. I. Katsnelson. First-principles theory of non-local screening in graphene. *Physical Review B*, 83(8):081409, February 2011.

[54] Lin-Lin Wang and Duane D. Johnson. Ternary tetradymite compounds as topological insulators. *Physical Review B*, 83(241309), June 2011.

[55] Frederick Wooten. *Optical Properties of Solids*. Academic Press, 1972.

[56] Yugui Yao, Fei Ye, Xiao-Liang Qi, Shou-Cheng Zhang, and Zhong Fang. Spin-orbit gap of graphene: First-principles calculations. *Physical Review B*, 75(4):041401, January 2007.

[57] E. Zaremba and W. Kohn. Van der Waals interaction between an atom and a solid surface. *Physical Review B*, 13(6):2270–2285, 1976.

[58] Haijun Zhang, Chao-Xing Liu, Xiao-Liang Qi, Xi Dai, Zhong Fang, and Shou-Cheng Zhang. Topological insulators in Bi2Se3, Bi2Te3 and Sb2Te3 with a single Dirac cone on the surface. *Nature Physics*, 5(6):438–442, May 2009.

[59] L. Zhang, N. Schwertfager, T. Cheiwchanchamnangij, X. Lin, P.-a. Glans-Suzuki, L. F. J. Piper, S. Limpijumnong, Y. Luo, J. F. Zhu, W. R. L. Lambrecht, and J.-H. Guo. Electronic band structure of graphene from resonant soft x-ray spectroscopy: The role of core-hole effects. *Physical Review B*, 86(24):245430, December 2012.

[60] Zhiyong Zhu, Yingchun Cheng, and Udo Schwingenschlögl. Band inversion mechanism in topological insulators: A guideline for materials design. *Physical Review B*, 85(23):235401, June 2012.